PRODUCTION AND CHARACTERIZATION OF CUZR-RE BASED BULK AMORPHOUS/NANOCRYSTAL COMPOSITE

A THESIS SUBMITTED TO
THE GRADUATE SCHOOL OF NATURAL AND APPLIED SCIENCES
OF
MIDDLE EAST TECHNICAL UNIVERSITY

BY

FATİH SIKAN

IN PARTIAL FULFILLMENT OF THE REQUIREMENTS
FOR
THE DEGREE OF MASTER OF SCIENCE
IN
METALLURGICAL AND MATERIALS ENGINEERING

AUGUST 2017

Approval of the thesis:

PRODUCTION AND CHARACTERIZATION OF CUZR-RE BASED BULK AMORPHOUS/NANOCRYSTAL COMPOSITE

submitted by **Fatih SIKAN** in partial fulfillment of the requirements for the degree of **Master of Science in Metallurgical and Materials Engineering Department, Middle East Technical University** by,

Prof. Dr. Gülbin Dural Ünver _____
Dean, Graduate School of **Natural and Applied Science**

Prof. Dr. C. Hakan Gür _____
Head of Department, **Metallurgical and Materials Engineering**

Assoc. Prof. Dr. Yunus Eren Kalay _____
Supervisor, **Metallurgical and Materials Eng. Dept., METU**

Assist. Prof. Dr. İlkay Kalay _____
Co-supervisor, **Materials Science and Eng. Dept., Çankaya University**

Examining Committee Members:

Prof. Dr. Tayfur Öztürk _____
Metallurgical and Materials Engineering Dept., METU

Assoc. Prof. Dr. Yunus Eren Kalay _____
Metallurgical and Materials Engineering Dept., METU

Assist. Prof. Dr. Caner Şimşir _____
Dept. of Manufacturing Engineering, Atılım University

Assist. Prof. Dr. Simge Çınar _____
Metallurgical and Materials Engineering Dept., METU

Assist. Prof. Dr. Sezer Özerinç _____
Mechanical Engineering Dept., METU

Date: 01.08.2017

I hereby declare that all information in this document has been obtained and presented in accordance with academic rules and ethical conduct. I also declare that, as required by these rules and conduct, I have fully cited and referenced all material and results that are not original to this work.

Name, Last name: Fatih Sıkan

Signature :

ABSTRACT

PRODUCTION AND CHARACTERIZATION OF CUZR-RE BASED BULK AMORPHOUS/NANOCRYSTAL COMPOSITE

Sıkan, Fatih

M.S., Department of Metallurgical and Materials Engineering

Supervisor: Assoc. Prof. Dr. Yunus Eren KALAY

Co-supervisor: Assist. Prof. Dr. İlkay KALAY

August 2017, 128 pages

Bulk metallic glasses have recently attracted much attention due to their high mechanical strength both in amorphous and in the amorphous/nanocrystal composite form along with their high glass forming ability. However, factors such as having a low plastic strain limit their potential application as structural materials. In this present work, ternary $(Zr_{50}Cu_{40}Al_{10})_{100-x}Sm_x$ (x:0-4 at. %) amorphous alloys were produced by melt-spinning in ribbon form and suction casting in bulk form within the diameter range of 1 to 3 millimeters. The amorphous and the devitrified states of these alloys were investigated with scanning electron microscopy (SEM), transmission electron microscopy (TEM), X-ray diffraction (XRD) and scanning differential calorimetry (DSC), Atom Probe Tomography (APT) techniques. Mechanical behavior of these alloys were investigated using compression and hardness testing. Failure modes and structures were analyzed using SEM as well. Furthermore, micro-mechanical testing experiments were conducted in order to get insights on the mechanical behavior of amorphous and partially crystalline specimens in nano and micro scale. Sm addition up to 4 at. % lead to nanocrystallization of approximately 5-10 nm spherical Cu_2Sm phase for $(Zr_{50}Cu_{40}Al_{10})_{96}Sm_4$ alloy. Further growth of Cu_2Sm phase was thought to

be hindered due to solute pile-up of Zr atoms at phase boundary and insufficiency of Sm atoms in amorphous phase. Since the amount of Sm atoms in amorphous matrix can be controlled by adjusting Sm content during alloying, nanocrystal size can be adjustable for such systems. Precipitation of Cu_2Sm nanocrystals were found to increase strength and hardness of $(Zr_{50}Cu_{40}Al_{10})_{96}Sm_4$ alloy; however, caused a significant embrittlement problem. Adjusting size and distributions of these nanocrystals may prove useful in eliminating this embrittlement problem. This study demonstrates how complex microstructures can be formed in a metallic glass to make a composite structure during devitrification and how these structures can be tuned for better properties.

Keywords: Bulk metallic glass, micro alloying, nanocrystallization, phase transformation, mechanical and structural characterization, micropillars.

ÖZ

CUZR-NTE BAZLI HACİMLİ AMORF/NANOKRİSTAL KOMPOZİT YAPILARIN ÜRETİMİ VE KARAKTERİZASYONU

Sıkan, Fatih

Yüksel Lisans, Metalurji ve Malzeme Mühendisliği Bölümü

Tez Yöneticisi: Doç. Dr. Yunus Eren KALAY

Yardımcı Tez Yöneticisi: Doç. Dr. İlkay KALAY

Ağustos 2017, 128 sayfa

Hacimli metalik camlar aynı zamanda hem amorf halleri hem de amorf/nanokristal kompozit hallerinin yüksek mukavemet değerleri ile dikkat çekmektedir. Ayrıca hacimli metalik camlar yüksek cam yapabilme kabiliyetleri sayesinde makro ölçeklerde üretilebilinmektedir. Fakat metalik camların düşük süneklikleri bu malzemelerin kullanımını kısıtlamaktadır. Bu çalışmada ise $(Zr_{50}Cu_{40}Al_{10})_{100-x}Sm_x$ (x:0-4 at. %) sisteminin amorf örnekleri eriyik savurma ile ince şerit halinde ve emme döküm yöntemi ile 1-3 milimetre çapında silindir çubuk olarak üretilmiştir. Numunelerin amorf ve devitrifiye halleri taramalı ve geçirimli elektron mikroskobu, X-ışını kırınımı ve diferansiyel kalorimetri teknikleri ile incelenmiştir. Mekanik özellikleri basma ve sertlik testleri ile analiz edilmiştir. Kırılma yüzeyleri ve kırılma mekanizmaları çalışılmıştır. Ayrıca micro-mekanik test deneyleri ile mekanik davranışları nano ve mikro boyutlarda incelenmiştir. Sonuç olarak, atomca % 4'e kadar Sm eklenmesi yaklaşık 5-10 nm boyutlarında küresel Cu_2Sm fazının nanokristallenmesine yol açmıştır. Nanokristal boyutlarının Zr atomlarının faz arayüzeylerinde birikmesi ve amorf matriks içerisinde bulunan Sm atomlarının yetersizliği nedeniyle daha fazla büyüyemediği gözlemlenmiştir. Bu gözlem,

mikroyapının kontrol edilebilmesine olanak sağlamaktadır; Sm miktarının alaşımlama sırasında kontrol edilmesi ile nanokristal büyüklüğü kontrol edilmesi ön görülmektedir. Cu_2Sm fazının oluşumu $(Zr_{50}Cu_{40}Al_{10})_{96}Sm_4$ alaşımının hem sertlik hem de mukavemetini arttırırken, malzemeye kırılganlık da kazandırmıştır. Bu kırılganlığın giderilmesi için nanokristal boyutlarının ve dağılımının kontrol edilerek incelenmesi yardımcı olabilir. Bu çalışma metalik camların tavlanması sırasında oluşabilecek kompleks yapıları ve bu yapıların daha iyi malzeme özellikleri için kontrol edilmesini sergilemektedir.

Anahtar Kelimeler: Hacimli metalik cam, mikro alaşımlama, nanokristallenme, faz dönüşümü, mekanik ve yapısal karakterizasyon, mikro kolonlar.

To My Precious Family…

ACKNOWLEDGEMENTS

I would like to thank to my supervisor Assoc. Prof. Dr. Y. Eren Kalay for his support and encouragement throughout my undergraduate and graduate study. I also owe a deepest gratitude to my co-supervisor Assist. Prof. Dr. İlkay Kalay for her insightful guidance.

I am also very grateful to Prof. Dr. Matthew Kramer for his support in sample production and to Assoc. Prof. Dr. Yaqiao Wu for his aid in APT experiments. I am indebted to Dr. Meltem Sezen for her contributions in FIB milling and to Assist. Prof. Dr. Sezer Özerinç and Dr. Amir Motallebzadeh, for their immense support during micro-mechanical testing experiments.

I also need to thank my previous and current laboratory mates Mertcan Başkan, Mert Övün, Eyüp Can Demir, Ayşe Merve Genç Ünalan, Özgün Acar, Mustafacan Kutsal, Ziya Anıl Erdal and Gökhan Polat for their patience and huge support. Especially Serkan Yılmaz and Bengisu Yaşar for their extra assistance during TEM studies.

I owe my heartiest thanks to my dear friends and colleagues Özgün Köse, Güney Mert Bilgin, Simge Tülbez and Doğa Atabay for their constant support in daily struggles and especially my deepest thanks to Doğancan Sarı for being there whenever I need.

Above all I thank Sıla Ece Atabay who helped me immensely throughout this work. I have no words to express my gratitude for her comfort, tender loving care and encouraging words that certainly lifted my morale whenever I required most. I thank her with all my heart for this thesis could not been accomplished without her support.

Finally, I would like to thank to my parents for their continuous support, encouragement, appreciation and love throughout my entire life. Especially, I would like to express my warm thanks to my brother, Tuncay Sıkan for his support.

TABLE OF CONTENTS

LIST OF TABLES

LIST OF FIGURES

NOMENCLATURE

APT: Atom Probe Tomography

BF: Bright-field

BMG: Bulk Metallic Glass

CVD: Chemical Vapor Deposition

DSC: Differential Scanning Calorimetry

FFT: Fast Fourier Transform

FIB: Focused Ion Beam

FWO: Flynn-Wall-Ozawa

GFA: Glass Forming Ability

HEXRD: High Energy X-ray Diffraction

HRTEM: High Resolution Transmission Electron Microscopy

HVOF: High Velocity Oxygen Fuel

ISE: Indentation Size Effect

KAS: Kissinger-Akahira-Sunose

LEAP: Local Electrode Atom Probe

LRO: Long Range Order

MG: Metallic Glass

PSD: Position Sensitive Detector

PVD: Physical Vapor Deposition

RE: Rare-earth Elements

ROI: Region of Interest

SAED: Selected Area Electron Diffraction

SEM: Scanning Electron Microscopy

STEM: Scanning Transmission Electron Microscopy

STZ: Shear Transformation Zone

TEM: Transmission Electron Microscopy

TM: Transition Metal

TTT: Time Temperature Transformation

VRC: Vacuum Reservoir Connection

XRD: X-ray Diffraction

CHAPTER 1

INTRODUCTION

1.1. Metallic Glasses

Metallic glasses can be seen as a junction between crystalline metals and amorphous glasses. Both of these material types were known to man for a quite long time. Silica based glass, namely obsidian tools were used even in Stone Age [1-2]. Later on with the discovery of smelting, Stone Age gave way to Bronze Age. Introducing metals into mankind via bronze, a copper based metal alloy [3]. Since then, metals and glasses have been recognized as completely different material groups and thus studied separately. This difference, in fact originated due to their structural differences and unique properties.

There are a couple of structural differences between metals and glasses. Metallic elements construct a lattice with a long range translational order, known as crystalline lattice via metallic bonding in metals, on the contrary, glasses contain mostly covalent and ionic or van der Waals bonds and completely lack long range translational order. The structure of the glasses is called *amorphous* (originates in Greek as *ámorphos*), meaning without form or shapeless implying the chaotic and non-repetitive structure of atoms within the material. Distinctly different atomic and electronic structures attribute to their unique material properties. In 1960 the first metallic glasses were synthesized by Duwez *et. al.* in Au-Si alloy system with a technique called splat quenching [4]. Discovery of metallic glasses merge the structural varieties of metals and glasses together, creating a non-crystalline structure with metallic bonding. Consequently, combining properties of metals and glasses lead to promising and unique properties.

1.2. History of Metallic Glasses

Discovery of metallic glasses by the work of Duwez *et. al.* in Au-Si alloy system created a scientific curiosity for amorphous metals and undercooled liquids. Pioneer studies of metallic glasses were centered on thin foils or ribbon samples, where the sample size is limited to micron size. Such samples were produced by splat quenching or melt spinning techniques, where melt is directly come in contact with the cold metal surface instead of quenching in liquid to prevent gaseous layers during rapid cooling of the material. Small sample thickness of ribbons and cold metal-melt interactions established an opportunity for extremely high cooling rates reaching up to 10^6 K/s. Later on better mechanical and magnetic properties of metallic glasses become clear to researchers. Thus, effort has been focused on finding more robust production routes and larger scale samples. Inoue proposed several empirical rules in order to stabilize supercooled liquid and increase chance of glass formation, thus decrease the necessary cooling rate in order to increase sample thickness [5]. In this respect, research led to development of bulk metallic glasses (BMGs). According to Inoue's empirical rules, a multicomponent alloy composition with at least 3 elements along with a deep eutectic temperature, elements with large atomic radii difference (approximate threshold value of 12% difference), negative heat of mixing in order to stabilize homogenous structure are some rules to obtain a glass former alloy. Satisfaction of these empirical rules results in a decrease in critical cooling rate and enabling production of millimeter scale glass samples in bulk form. Figure 1.1 shows the change in critical casting thickness in centimeters with years. In 1969, Chen and Turnbull produced the second metallic glass in Pd-Si-M (M=Ag, Cu, Au) system at a cooling rate ranging between 10^2 to 10^3 K/s [6].

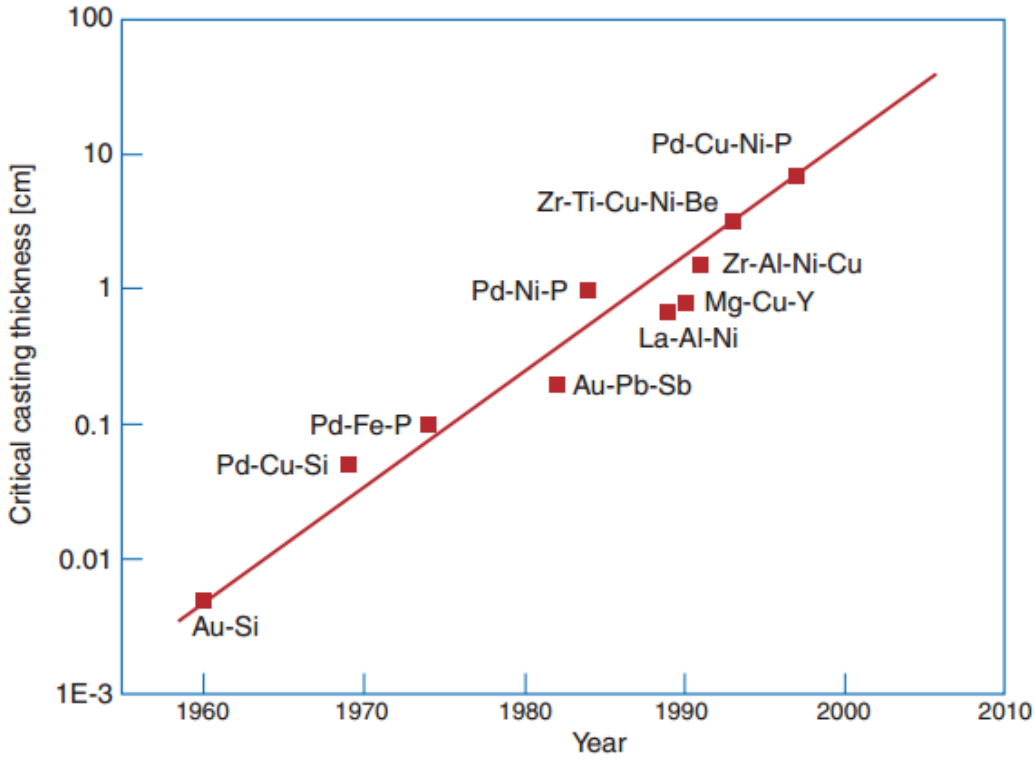

Figure 1. 1 Metallic glass sample size with respect to years. Adopted from [7].

Later on in 1990s, commercial metallic glasses are born with the production of Zr-Cu-Ti-Ni-Be alloy systems commonly known as Vitreloy by Johnson and Peker [8]. Development of commercial metallic glasses lead to new applications which were initially limited to sporting goods.

1.3. Application Areas of Metallic Glasses

Metallic glasses attract the interest of many researchers and remarkable effort spent on literature in order to produce metallic glasses out of various systems and with multiple production routes. The major reasons of such interest in these systems is the promising properties of the metallic glasses such as high strength and hardness combined with superior elasticity, good thermal stability, exceptional wear and corrosion resistance [9]. Thus, metallic glasses are possible candidates for many application areas in

industry. Although metallic glasses inherit their superior properties from their non-crystalline nature, their weakness also comes with it. Since there is no translational symmetry of atoms arranged in long range order, in other words, crystalline lattice, there is no dislocation movement. The absence of dislocations causes very limited plasticity for metallic glasses. Generally metallic glasses tend to deform elastically and fail in a brittle manner where the fracture occurs catastrophically [10].

Sudden fracture characteristic of metallic glasses limits their application areas drastically. Today only critical application of metallic glasses can be considered as anti-corrosive coatings or magnets for nuclear reactors. Due to their non-crystalline nature and chemical homogeneity, metallic glasses have exceptional corrosion and irradiation resistance. Metallic glass coatings that are prepared by High Velocity Oxygen Fuel (HVOF) are used in industry to prevent oxidation and corrosion of critical surfaces [11]. In addition, magnetic properties of metallic glasses are resistant to radiation damage making them good nuclear reactor magnets for longer service life [12].

The first company to produce metallic glass products in bulk form was Liquidmetal Technologies. The company developed and produced their trade mark product as Vitreloy and focused on application areas such as sporting goods, biomedical, electronics and defense. The very first application of metallic glasses was golf club heads. Metallic glass golf club heads rapidly replaced Ti golf club heads due to their superior mechanical properties. Ti golf club heads transferred 70% of the impact energy to ball, while for metallic glass the value is 99% [13]. Such a high value is reached due to the fact that metallic glasses do not have any microstructural features which act as impact energy absorbers. Since there are no grains and grain boundaries in amorphous structure, the impact energy absorption is very limited.

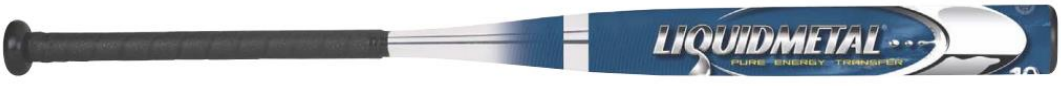

Figure 1. 2 Vitreloy baseball bat with “pure energy transfer” label. Adopted from [13].

Figure 1.2 shows a Liquidmetal Vitreloy baseball bat with “pure energy transfer” label underlying the high impact energy transfer efficiency. Another applications of metallic glasses are strong and light casings for electronic products such as cell phones and watches. However, production cost and manufacturing limitations have a negative impact on popularity of such casings.

1.4. Concept of Glass Forming Ability

Determination of glass forming abilities (GFA) of metallic glass candidates is at utmost importance for the development of new glass former alloys. From the discovery of metallic glasses, the question at what compositions metallic glasses form is extensively considered. Any answers to this question has the potential to reduce the required effort to find new glass former compositions. Concept of glass forming ability, defines how easily the alloy system solidifies into amorphous structure in room temperature. This basic explanation, in fact determines the two major criterions of metallic glass production; critical cooling rate requirement and maximum practical casting thickness.

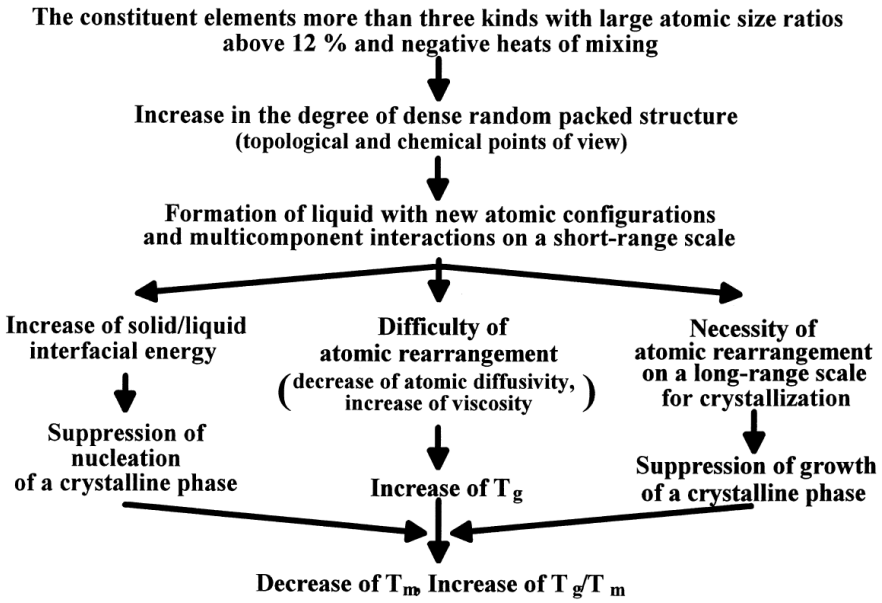

Figure 1. 3 Inoue’s mechanism for high glass forming ability on a multicomponent alloy system. Adopted from [5].

First studies to understand glass forming ability centered on heat of mixing and the atomic size difference. As mentioned earlier, Inoue stated several empirical rules on glass former alloys. Figure 1.3 shows the mechanisms for stable undercooled liquid and high glass forming ability for a multicomponent alloy system. According to his mechanism, suppression of nucleation and growth of a crystalline phase and difficulty of atomic rearrangement has a strong effect on stabilization of undercooled liquid, this approach led to "confusion principle", first coined by H.H. Liebermann while he was a graduate student at the University of Pennsylvania [9]. "Confusion principle" simply underline the idea of complicating and confusing the crystal, so that it will not form with ease. In addition to complex crystal structure, multi-elemental nature of the alloy increase entropy to stabilize the homogenous glass structure.

Glass forming ability is represented by the ratio of glass transition temperature, T_g over liquidus temperature, T_l and known as reduced glass transition temperature, T_{rg} [6]. Higher reduced glass transition temperature indicates that the glass forming ability of the alloy is also high. Another GFA indicator, γ is proposed by Lu *et. al.* [14]. Gamma indicator also takes crystallization temperature into consideration [15]. Equation 1.1 and 1.2 shows the relationship between important characteristic temperatures and glass forming ability indicators.

$$T_{rg} = \frac{T_g}{T_l} \qquad \text{Equation 1.1}$$

$$\gamma = \frac{T_x}{T_g + T_l} \qquad \text{Equation 1.2}$$

In their work Lu correlate glass forming ability to required critical cooling rate and practical maximum sample thickness and obtained two formulas by experimental results. By using equation 1.3 and 1.4, it is possible to determine experimental limits via DSC/DTA measurements.

$$R_c = 5.1 \times 10^{21} exp(-117.19\gamma) \qquad \text{Equation 1.3}$$

$$Z_c = 2.80 \times 10^{-7} exp(41.70\gamma) \qquad \text{Equation 1.4}$$

Figure 1.4 shows the change in critical cooling rate, R_c or critical section thickness, Z_c with respect to γ indicator. As seen in the figure R_c shows a decreasing trend while Z_c shows an increasing trend with increasing γ. Another important aspect that should be pointed out is γ=0.35 is defined as an approximate threshold value for the type metallic glass.

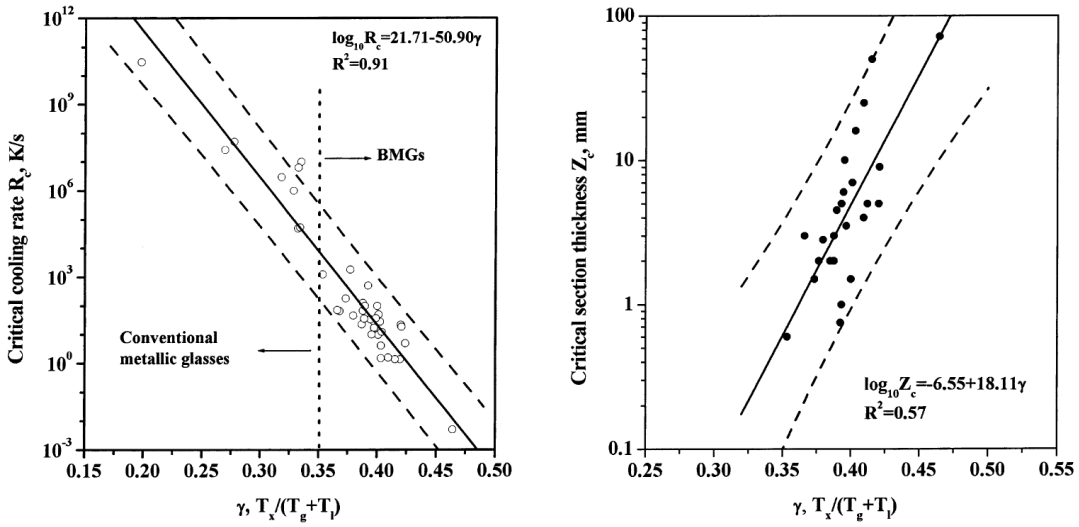

Figure 1. 4 Change in critical cooling rate and critical section thickness with respect to γ, $T_x/(T_g+T_l)$. Adopted from [14].

1.5. Kinetics and Thermodynamic Approach of Metallic Glasses

Glass forming ability of a metallic glass is directly related to the thermodynamics and kinetics of the supercooled melt.

1.5.1. Thermodynamic Approach

At constant temperature and pressure the spontaneity criterion is the Gibbs free energy change of a system. Under conditions where $\Delta G < 0$, the chemical reactions or phase transformations take place spontaneously, in other words, systems tend to minimize their Gibbs free energy by phase transformations. In the case of supercooled melts, as the temperature of the melt is reduced below T_l, Gibbs free energy of the crystalline

solid phase is lower compared to the supercooled melt. The Gibbs free energy difference, ΔG, between solid and liquid phases are establishing the driving force for crystallization. As the melt is more and more undercooled due to the temperature decrease, driving force for crystallization increases. Thus, supercooled liquid becomes more unstable and glass formation gets harder.

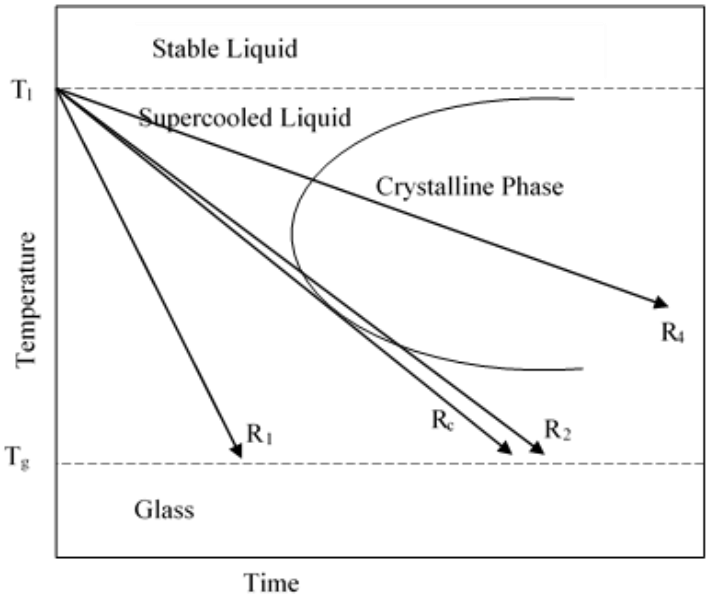

Figure 1. 5 Time-temperature-transformations diagram for glass formation.

Figure 1.5 shows the TTT diagram for glass formation. Diagram also shows several hypothetical cooling rates along with the critical cooling rate for glass formation. As seen in the diagram, the liquid phase is stable above the liquidus temperature, T_l. As temperature decrease below T_l, liquid becomes unstable and if enough time is given it will reduce its Gibbs free energy by crystallization. Melt tends to perform this transformation more, as temperature decreases down to nose of crystalline phase curve due to increasing ΔG.

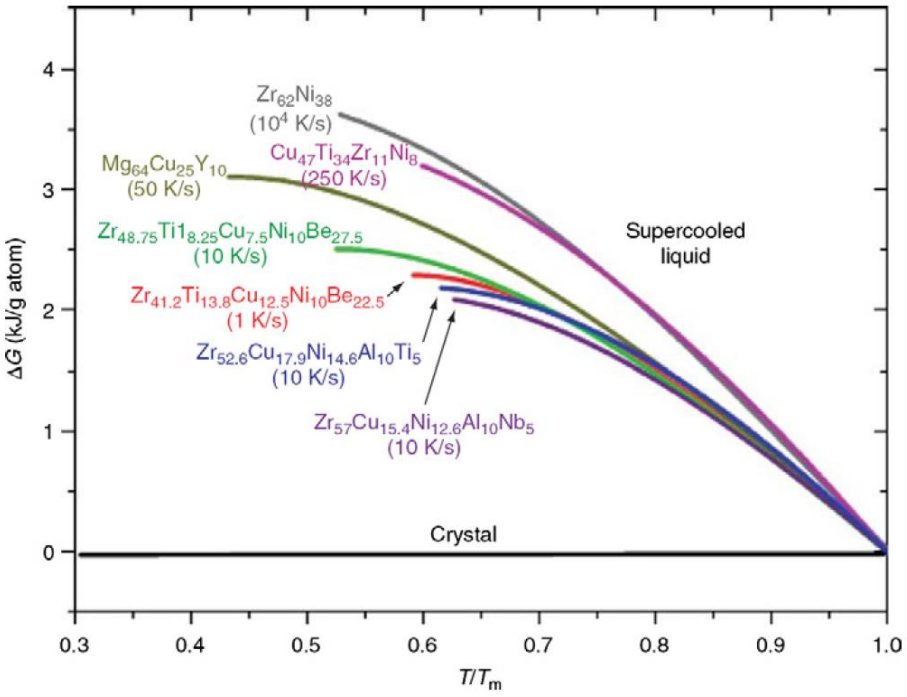

Figure 1. 6 ΔG change with respect to undercooling for various alloys. Adopted from [16].

In Figure 1.6, driving force change with respect to undercooling is shown. As seen in the figure for all alloy systems ΔG shows an increasing trend with undercooling. Increase is higher for some of the alloy systems, this phenomenon is also one of the factors defining glass formability of the alloy. Another important temperature in the TTT diagram is the glass transition temperature. Generally, when supercooled melt exceeds T_g, glass formation occurs. For the cases where cooling rate is lower than R_c, the crystallization occurs. While complete crystallization occurs for R_4, partial crystallization will take place for R_2. In the case of R_1 no crystallization will occur. Although thermodynamics determines the glass formability of the melt, it is kinetic factors that dictates the final structure.

1.5.2. Kinetic Approach

Understanding of the kinetic properties of the supercooled melt requires the comprehension of specific volume and more importantly corresponding viscosity

term. Firstly, while the temperature of the melt is decreased, its specific volume decreases mainly due to the thermal expansion coefficient.

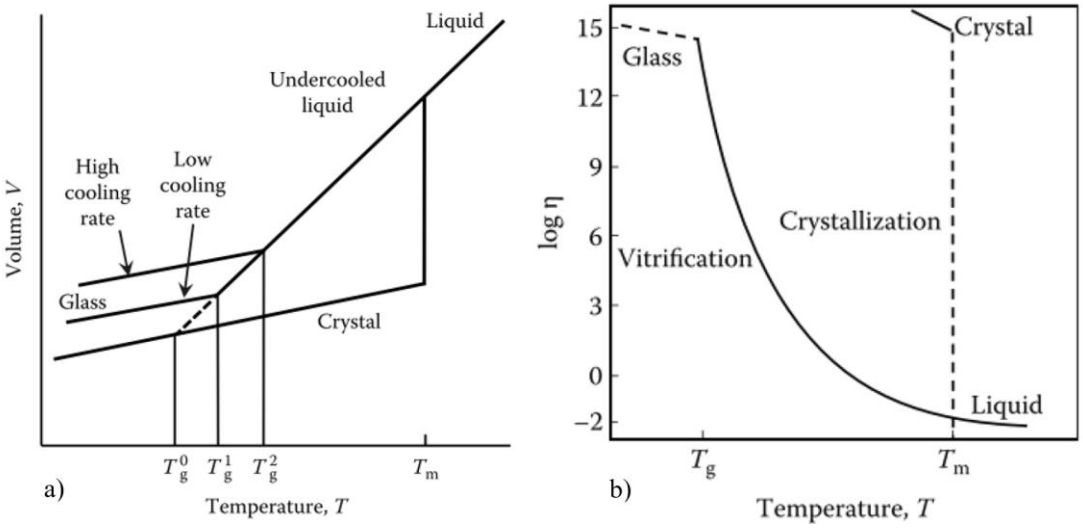

Figure 1. 7 Variation of (a) specific volume and (b) viscosity with temperature for both crystals and glasses. Adopted from [17].

Figure 1.7 (a) shows specific volume change with temperature. In case of crystallization, specific volume decrease is discontinuous and rapid. If crystallization is somehow retarded; as temperature decrease, specific volume continues to decrease and when temperature eventually reach glass transition temperature, supercooled liquid turns into a solid with amorphous nature due to increased viscosity. It is also clear that at different cooling rates, glass transition temperature and specific volume of the glass is different, so glass formation and its structure should depend on cooling rate as well as viscosity of the liquid. Figure 1.7 (b) depicts the change of viscosity with temperature below T_m. Similar to specific volume crystallization causes a strong discontinuous increase in viscosity via solidification of melt. On contrary, vitrification causes a continuous viscosity increase up to T_g. As both temperature decrease and viscosity increase further, mobility that is required for rearrangement of atoms is decreased. Since mobility and diffusion is very limited at relatively low temperatures, the time that is necessary for system to reach in equilibrium (in this case crystallization of the supercooled melt) increases exponentially and rather becomes non-practical.

1.6. Mechanical Behavior of Metallic Glasses

As mentioned earlier in the thesis, metallic glasses tend to deform elastically at room temperature due to the fact that they lack the crystalline structure which attribute to the plasticity. Although at macroscopic scale their deformation is elastic, there is remarkable plasticity within localized zones, called shear bands. There are several theories concerning the localized plasticity zones in literature. Among them shear transformation zone (STZ) theory is studied in detail [18]. Since structural defects such as dislocations, stacking faults or twins are not present in monolithic metallic glasses, the stress relaxation proceeds by shear movement of atom groups within transformation zones.

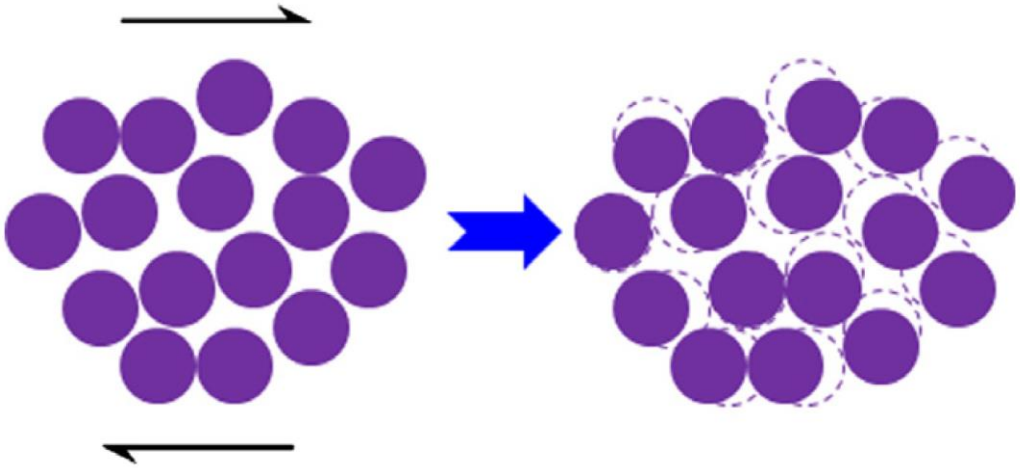

Figure 1. 8 Illustration of STZ mechanism in MG under stress. Adopted from [19].

Figure 1.8 depicts the STZ theory mechanism for metallic glasses under stress. The main challenge in order to understand the stress relaxation within metallic glasses is that STZ cannot be observed via TEM unlike dislocations. Another difference between dislocation motion and STZ is that the energy barriers for activation. Activation energy for dislocation movement is characteristic depending on the crystal structure while activation energy for SZT varies. More unstable regions within the amorphous structure will activate easier compared to less unstable ones. Consequently,

investigation of deformation mechanisms or mechanical behaviors for metallic glasses becomes a challenging topic.

1.6.1. Shear Bands and Serrated Flow

In macroscopic scale, deformation under tensile loading consist of elastic deformation with approximate fracture strain of 2% [20]. In compressive loading, however, elastic deformation is accompanied by yielding and limited plastic deformation without work hardening. Most metallic glasses show serrated flow before yielding occurs [21]. Serrated flow or zig-zag pattern on stress-strain curve is caused by the stick and slip mechanisms of shear bands [22–24]. As increasing load is applied on the glassy samples, material tries to relieve the stress by nucleation and propagation of shear bands. Shear banding in metallic glasses occurs in a catastrophic manner, in fact, shear band propagating rate is about 10^{-5} s [25]. Such high propagation speed reveals that the rate controlling step for fracture is the nucleation of the shear bands. In certain cases, shear band propagation is retarded or even arrested until higher amount of load is applied. Thus, metallic glasses sequentially have bursts of strains and arrests at shear bands. This phenomenon is defined as shear band stability. Strain amounts, frequency or time ranges of these bursts depend on the structure and composition of the alloy, as well as loading rate. If the shear band nucleation rate is slower than loading rate, deformation seems rather homogeneous. In such cases strain is distributed and continuous stress-strain diagram is obtained. For lower loading rates, there is enough time for shear band nucleation. Nucleated shear bands rapidly propagate and cause strain bursts. Generally, metallic glasses with constant shear band arresting are called more “ductile” compared low shear band stability metallic glasses. Figure 1.9 (a) illustrates the effect of loading on serration flow mechanism via load to nano-indentation depth diagram. Serrated flow is disappeared as the loading rate is increased.

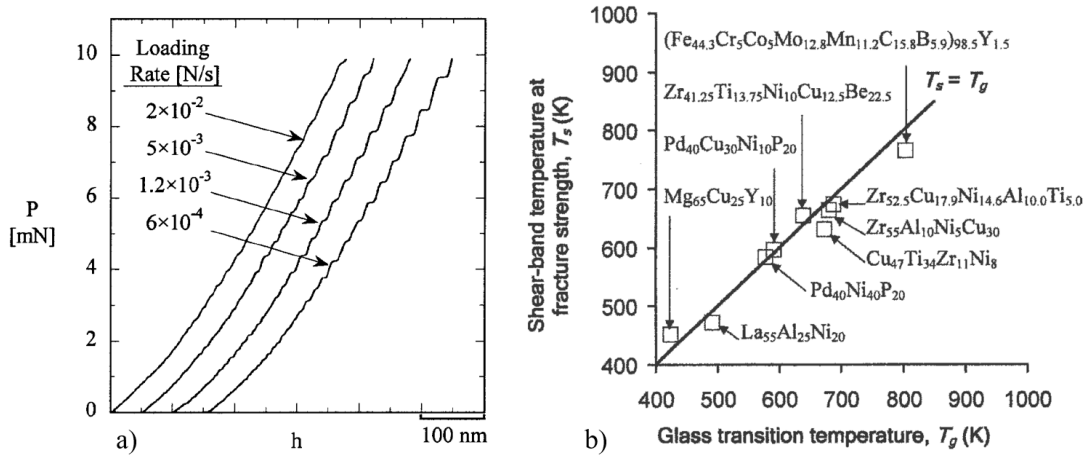

Figure 1. 9 (a) Effect of loading rate on flow mechanism and (b) correlation of shear band temperature at fracture strength with T_g. Adopted from [21] and [26] respectively.

Formation of the shear bands also cause some shear softening. Temperature of the shear band area increases due to the localized deformation during loading of a metallic glass. In some cases, this local temperature rise can result in local melting in shear band vicinity. Temperature rise varies from less than 1 to 1000 K in some of the systems [26-27]. Fracture surface of shear band zones contain evidence of local melting.

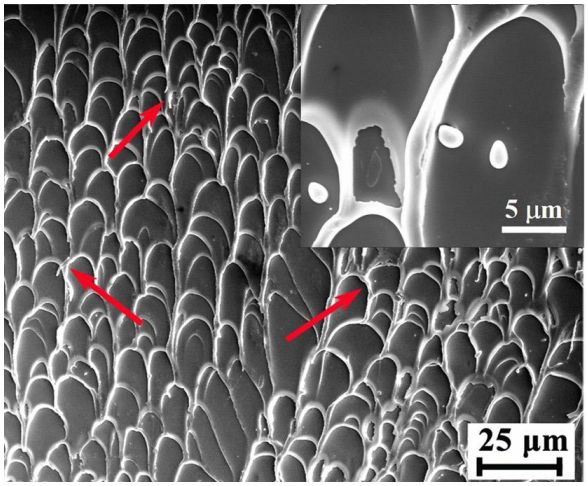

Figure 1. 10 Vein patterns covering the fracture surface of shear band. Adopted from [28].

Figure 1.10 shows the micrograph of fracture surface of a shear band area. The surface is covered in vein patterns. Inset depicts evident liquid-like features and droplets. Temperature rise during loading is strongly depends on the glass transition temperature of the metallic glass. For effective softening to occur, temperature should be near the glass transition temperature. Figure 1.9 (b) illustrates that for various alloy compositions, shear band temperature at fracture strength is very close to the glass transition temperature of the alloys [26-27]. The softening of the glassy alloy attributed by the sudden viscosity drop due to local heating, thought to be one of the reasons of catastrophic failure in metallic glasses.

1.6.2. Fracture Modes

Shapes of the fracture surfaces reveal much information about the fracture mode and mechanical properties of the metallic glasses. Unique fracture modes can be classified in three major group, while in some cases fracture surface contains more than a single mode.

Shear Fracture Mode

Shear fracture mode is the most well-known among the three fracture modes. It is usually observed in tension or compression of relatively "ductile" metallic glasses in which final fracture occurs via shearing of an inclined plane to the loading axis. This type of fracture is similar to one seen in critical resolved shear stress plane at an angle of 45^{o} angle, but the shearing angle for metallic glasses deviates from 45^{o} angle. Deviation is positive in case of tension and negative in case of compression [29–31].

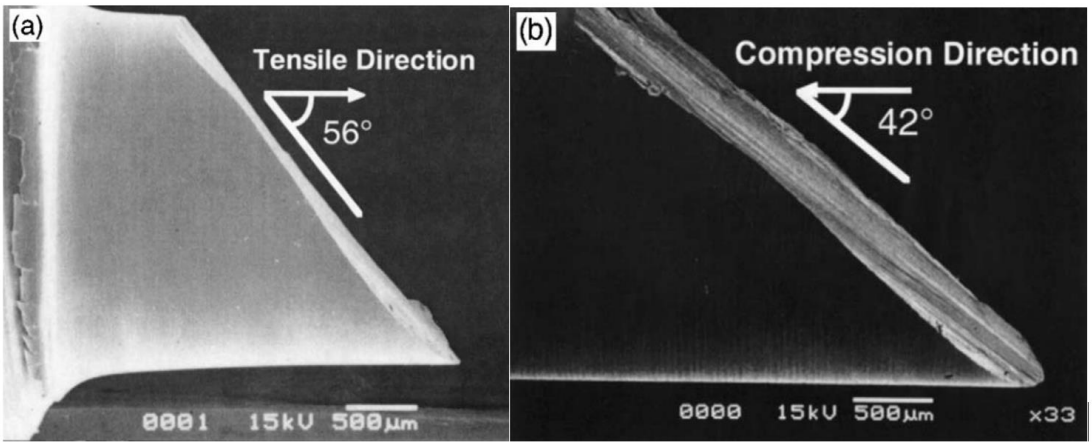

Figure 1. 11 Example of shear fracture under (a) tension and (b) compression for Pd-Ni-P metallic glass. Adopted from [31].

Figure 1.11 shows two examples of shear fracture mode in tensile and compressive loading conditions. Deviation from 45^{o} angle reveals that the failure is not only controlled by deviatoric stresses. Shear fracture mode mostly appears in Zr, Cu, Ti and noble metal based metallic glass compositions. Shear fracture is caused by shear instability on a dominant shear band. As mentioned before, shear band surface is covered by vein patterns and liquid-like features revealing there is evidence of local heating accompanied by softening and plasticity. Due to these features, shear fracture mode is characterized as a "ductile" behavior for metallic glasses.

Cleavage Mode

In cleavage fracture mode, metallic glass sample splits into two along the axis perpendicular to the loading axis. Cleavage in metallic glasses is utterly different compared to the cleavage in crystalline materials. Crystal planes play an important role in cleavage of crystalline materials, since cleavage occurs along the planes of atoms that are weakly bound. In amorphous structure crystal planes are absence, so cleavage follows a wavy pattern of unstable regions. In cleavage surface of metallic glasses mirror, hackle and mist regions are observed [32]. In Figure, 1.12 these regions are illustrated. Cleavage fracture mode is mainly observed under tensile loading of Mg,

Fe and rare-earth element based metallic glasses [33]. This fracture type is characterized as having a brittle manner.

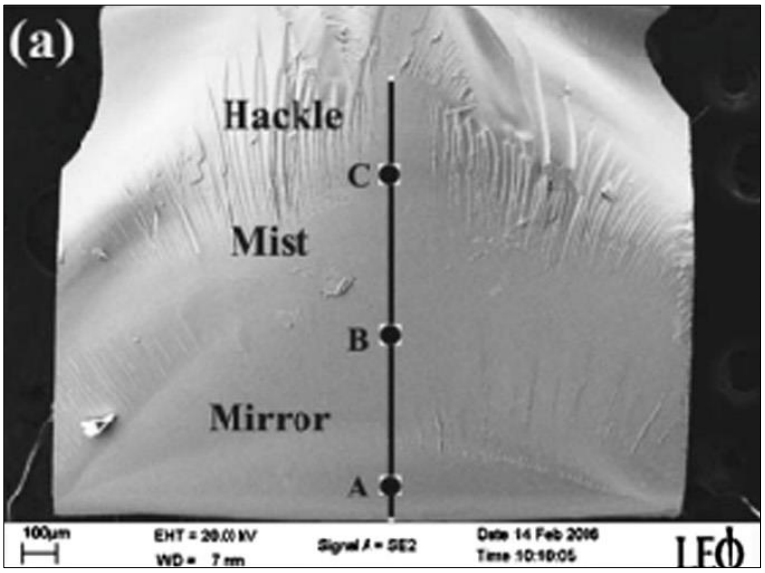

Figure 1. 12 Micrograph of cleavage fracture surface. Adopted from [32].

Fragmentation Mode

Fragmentation mode is observed in extremely brittle metallic glasses. In this fracture mode, glassy alloy splits into many small pieces and fragments in a blast upon loading. Fragments of the fracture are generally uniform and about 50 microns in size. In fragmentation fracture mode fracture surface does not have any sort of vein patterns or liquid-like features. Fragments generally contain a fracture core and radiating marks out of the core. Illustration of fragmentation fracture mode is shown in Figure 1.13 (a). Zhang *et. al.* studied the mechanism of the fragmentation fracture mode in Co-based metallic glasses [34–36].

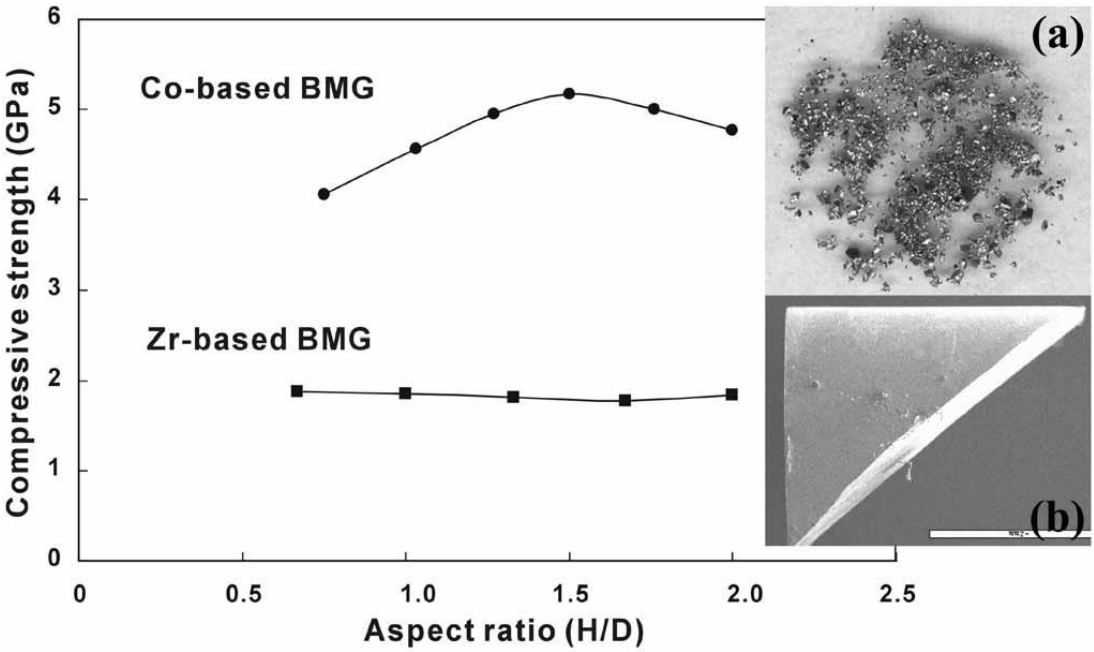

Figure 1. 13 Change in compressive strength with respect to aspect ratio for (a) Co-based fragmented and (b) Zr-based sheared metallic glasses. Adopted from [36].

Zhang revealed that the fragmentation occurs via the nucleation of small fracture sites within the volume before the final fracture. These fracture sites rapidly propagate leading to a fracture blast of small fragments. In Figure 1.14, fracture mechanism of pure shear and fragmentation modes are shown.

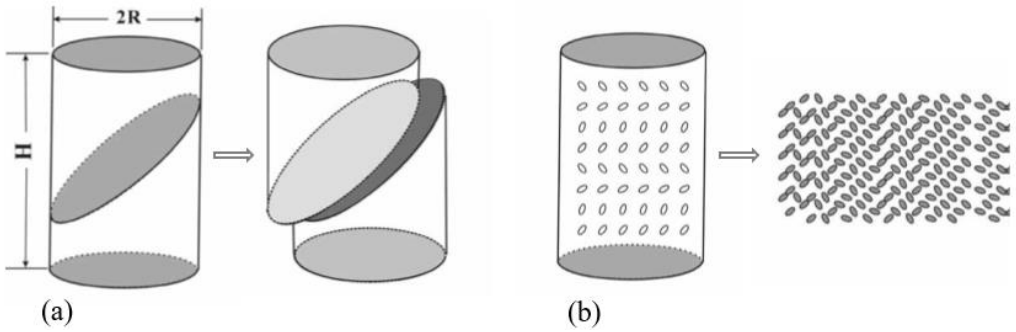

Figure 1. 14 Fracture mode mechanism schematic for (a) shear and (b) fragmentation fracture mode. Adopted from [36].

1.7. Production of Metallic Glasses

Since the discovery of the metallic glasses, their production became a tedious work. Production parameters of metallic glasses mainly depend on the type that is produced. There are two main classes of metallic glasses; bulk metallic glasses and marginal glass formers. The classification practically based on the critical cooling rate requirement during production. Vitrification of bulk metallic glasses, BMGs, are easier compared to marginal glass formers due to their low critical cooling rates. Critical cooling rate requirement for BMGs range between 1 to 100 K/s which makes their production less tedious. However, in practice, this still limit their production techniques to several methods and their maximum diameters to 10-20 mm. Marginal glass formers are harder to produce with required critical cooling rate of 10^6 K/s, which is only achieved by a few production methods. Unlike BMGs, marginal glass formers can only be produced in the forms of thin films or ribbons. In this thesis the emphasis will be given on bulk metallic glass compositions.

Metallic glass production classification mainly depends on the pre-cursor or the parent phase. In most cases, their production is explained via vitrification techniques and critical cooling rates; however, not all metallic glass production methods must involve a cooling. In fact, one sub-group of metallic glass production is focused on distorting the lattice in order to obtain amorphous structure. Any method of disturbing perfect lattice and crystal structure to claim disordered amorphous structure in a solid form can be accepted as metallic glass production.

1.7.1. Vitrification from Liquid State

Requirements and necessities of this production type is already mentioned earlier in this thesis. The major point of vitrification from liquid state is that parent physical state is already in amorphous structure. For this group of production techniques, main aim is to suppress crystallization in order to maintain amorphous structure up to the points where crystallization can no longer practically take place. This is achieved by reaching higher cooling rates than critical cooling rate. So, the solidification process should be

rapid in all these techniques. Since the discovery of metallic glasses, high cooling rates are achieved by melt to cold metal interactions. The quenching provided from the water cooled cold metal depends on the production technique, but in general provides the best cooling performance. The first metallic glass was produced by splat-quenching technique where melt is quenched between two copper plates. Later invention of melt-spinning technique enabled faster metallic glass production. In melt-spinning technique, melt is quenched by a rotating copper wheel and collected in the form of micron thick ribbons. Next widely used method was suction, chill or injection casting methods. These methods provided a lower cooling rate; however, improved sample thickness greatly. By casting methods, metallic glasses production in millimeter scale become possible. Figure 1.15 (a) shows critical parts of a melt-spinner. Set up consist of rotating copper wheel, induction coil, liquid metal holder and nozzle, cooling units and inert gas valves. Figure 1.15 (b) shows suction casting platform integrated into an Edmund Bühler arc-melter.

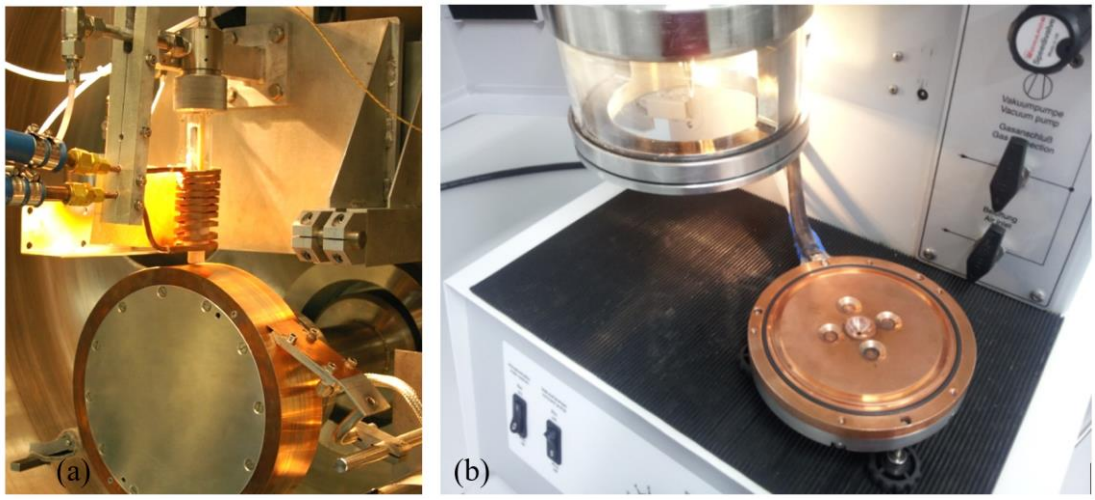

Figure 1. 15 (a) An example of melt-spinning set up and (b) the suction casting set up used in this thesis study. Adopted from [37].

1.7.2. Deposition from Gaseous State

Production of metallic glasses from gaseous state is an another non-equilibrium cooling technique which is focused on various deposition methods. In these production routes final samples are in forms of micron thick thin films (5-10 micrometers). Major examples of these gaseous metallic glass production techniques are chemical vapor deposition (CVD) and physical vapor deposition (PVD) methods. Among various techniques, magnetron sputtering is widely used in order to produce thin film metallic glasses. In magnetron sputtering extremely high cooling rates (reaching up to 10^9 K/s) can be achieved via liquid nitrogen cooling of substrate. Although cooling rate is optimal for metallic glass production, managing the composition of alloys is compelling for magnetron sputtering. Since the system elements are randomly deposited through ion bombardment of the target material, there occurs some compositional fluctuations over sample [38–40].

Another production technique is thermal spray coating method, namely plasma spraying and high velocity oxygen fuel. Although the pre-cursor physical state is liquid for HVOF, samples obtained are in form of thin films via spray deposition. Although coating thicknesses are relatively thick (~500 micrometers), they are not in bulk form [11]. The main use of metallic glass production via HVOF is for anti-corrosive or anti-wear coatings of strategic parts.

1.7.3. Amorphization from Solid State

Amorphization methods from the solid state is inheritably different than other methods, since the initial phase is already in crystalline form. Instead of suppressing crystallization, main effort is focused on distortion of crystalline lattice. Distortion of crystal structure is mainly achieved via severe deformation of the material. Extreme deformation cause generation of lattice defects such as dislocations, stacking faults and vacancies in high density. Due to high density of lattice defects atomic arrangement is distorted leading to high energy, unstable amorphous structure. Amorphization via mechanical alloying is another type of deformation induced

amorphization technique. Mechanical alloying is done via ball milling techniques using high purity alloying elements of the system. Depending on the composition, in general 20-100 hours of milling time results in powders with amorphous alloy structure [41-42].

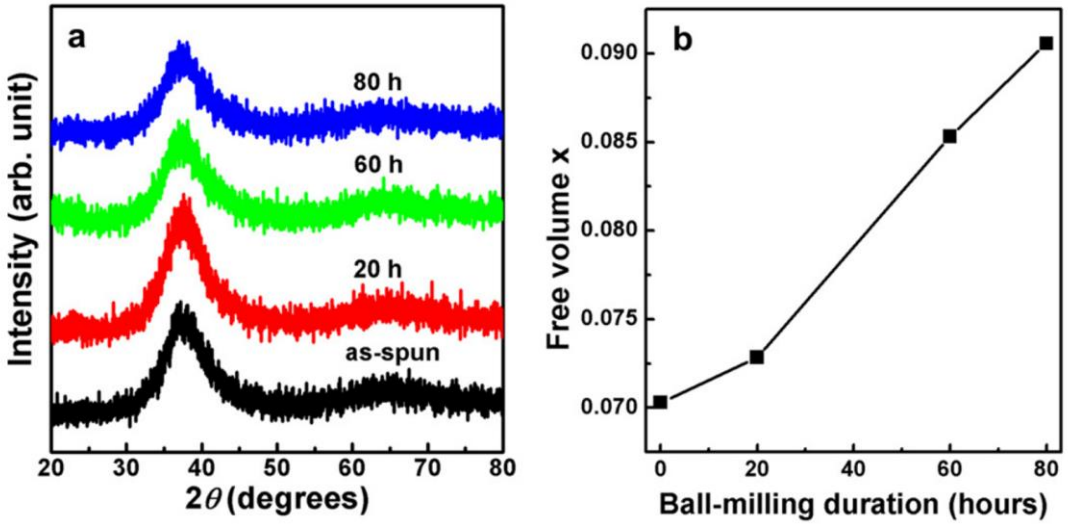

Figure 1. 16 (a) XRD patterns of ball milled Zr-based MG samples and (b) free volume change with milling duration. Adopted from [41].

Figure 1.16 (a) shows the XRD patterns of ball milled Zr-based metallic glass samples. For all milling durations and as-spun samples, amorphous main hump is evident. Even 20 hours of milling time results in amorphous structure for this alloy composition. Figure 1.16 (b) shows free volume change of amorphous structure with respect to milling duration. Increased free volume by milling reveals the effect of severe deformation on the structure.

1.8. Thermal, Structural and Mechanical Characterization of Metallic Glasses

Characterization of metallic glasses is at utmost importance since their properties and promising future application areas are directly correlated with their structure. Understanding their thermal, structural and mechanical properties reveals valuable

information in developing more metallic glass compositions and improving their properties. In literature metallic glasses are studied by various characterization techniques such as differential scanning calorimetry (DSC), X-ray diffraction techniques such as conventional (XRD) or high energy X-ray diffraction via synchrotron radiation (HEXRD), transmission electron microscope (TEM), 3D Atom Probe Tomography (3DAPT).

Mechanical performance of metallic glasses is studied by various in-situ and ex-situ mechanical tests such as hardness and nano-indentation tests, tension or compression tests in macro scale; however, the recent developments and focused ion beam technique enabled researchers to perform micro scale (0.5 to 3 μm diameter samples) mechanical tests via micropillar compression tests.

1.8.1. Differential Scanning Calorimetry

Differential scanning calorimetry (DSC) is a very powerful technique to track physical changes during heating or cooling of materials [43]. Thermal properties of materials can also be evaluated in isothermal conditions using this technique. It is possible to determine temperatures for melting, boiling, freezing, any other first and second order phase transformations, oxidation, deoxidation, and decomposition reactions. In addition, heat change (ΔH) of phase transformations, heat capacity of materials and activation energy for reactions can be calculated from the data provided by DSC. In the field of physical metallurgy and especially metallic glasses, DSC has an important role for determination of glass transition temperature (T_g), crystallization temperature (T_x) and thermal stability of a metallic glass. Other important information such as devitrification path of the alloy can also be revealed when DSC data is correlated with other characterization techniques such as XRD and TEM.

1.8.2. Conventional X-ray Diffraction and Synchrotron Light Source

X-ray diffraction (XRD) is one of the most important structural characterization in the field of material science. Scientists can obtain valuable information from X-ray

diffraction patterns such as crystalline structure, phase analysis, crystallite size, lattice parameter etc. XRD patterns can be studied by using Bragg's Law, which is;

$$n\lambda = 2d \sin\theta \qquad \text{Equation 1.5}$$

where n is the order of diffraction, λ is the wavelength of the incident x-ray beam, d is the interplanar spacing and θ is the incident angle within the XRD pattern.

Although Bragg's Law and XRD analysis combined creates an opportunity to investigate crystalline structure, metallic glasses do not inherit any sort of long range order (LRO) to begin with. Due to their non-crystalline, shapeless nature XRD patterns of amorphous samples do not exhibit any diffraction peaks, but a diffuse and broad main peak-like hump followed by wavy pattern. Figure 1.16 (a) shows a typical XRD pattern for an amorphous sample where there is a main hump. Synchrotron Light Source characterization is similar to conventional XRD; however, much more powerful. Synchrotron radiation enabled researchers to work with higher brilliance and coherency meaning higher number of photons per area and time. Major use of synchrotron radiation in characterization of metallic glasses is ex-situ/ in-situ high energy X-ray diffraction (HEXRD) experiments. Through high brilliance and adjustable energy of photons in synchrotrons, it is possible to observe any structural change within the material. HEXRD data can be used to conduct structural simulations such as Reverse Monte Carlo or Molecular Dynamics. HEXRD patterns can be obtained in a shorter time compared to conventional XRD, giving an opportunity to perform in-situ XRD experiments. Main drawback of synchrotron radiation is their accessibility. Since these facilities are few in number around the world, researchers have to propose their research to gain access for limited times called beam time. Still synchrotron facilities prove useful not only for material science but also for other branches such as biology, medicine and geology.

1.8.3. Transmission Electron Microscope

Transmission electron microscope (TEM) characterization is at utmost importance for structural characterization. TEM provides atomic scale resolution which makes it the

appropriate tool for many structural investigations. In the field of metallic glass studies, scientists use TEM in order to investigate both as-cast state to reveal vitrification efficiency and devitrified state to reveal crystallization kinetics and sequences. TEM not only provides imaging at high resolution, but also can be used to perform electron diffraction in a relatively small selected area. TEM characterization can be used to investigate structure in both real space and reciprocal space through fast Fourier transformation (FFT) analysis. Combining imaging and diffraction, TEM can be used to investigate shapes, sizes and crystallographic structures of crystals that are formed in metallic glasses. In addition, by sophisticated attachments such as a hot stage or a nanoindenter it is possible to perform in-situ heating or mechanical testing experiments within TEM while investigating the structural changes. Fig. 1.17 shows TEM micrographs of $Cu_{10}Zr_7$ crystals embedded within amorphous matrix in a $Cu_{56}Zr_{44}$ melt-spun alloy. Insets in images depicts selected area electron diffraction (SAED) patterns of shown regions [44].

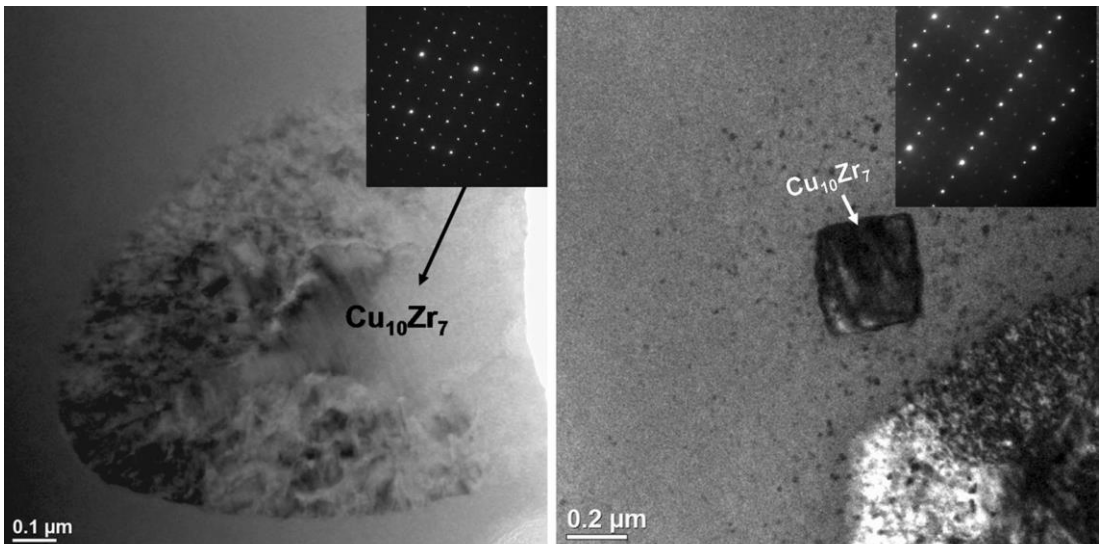

Figure 1. 17 (a) TEM micrographs of annealed $Cu_{56}Zr_{44}$ metallic glass alloy showing the crystallized phases. Adopted from [44].

1.8.4. 3D Atom Probe Tomography

Atom Probe Tomography (APT) is a novice method that can be used to investigate atomic scale material characterization. Although APT seems weak on structural characterization, it is extremely powerful on chemical characterization due to its atomic scale spatial and chemical resolution (around 0.1-0.3nm resolution in depth and 0.3-0.5nm laterally) [45]. Fig. 1.18 illustrate the working mechanism of APT.

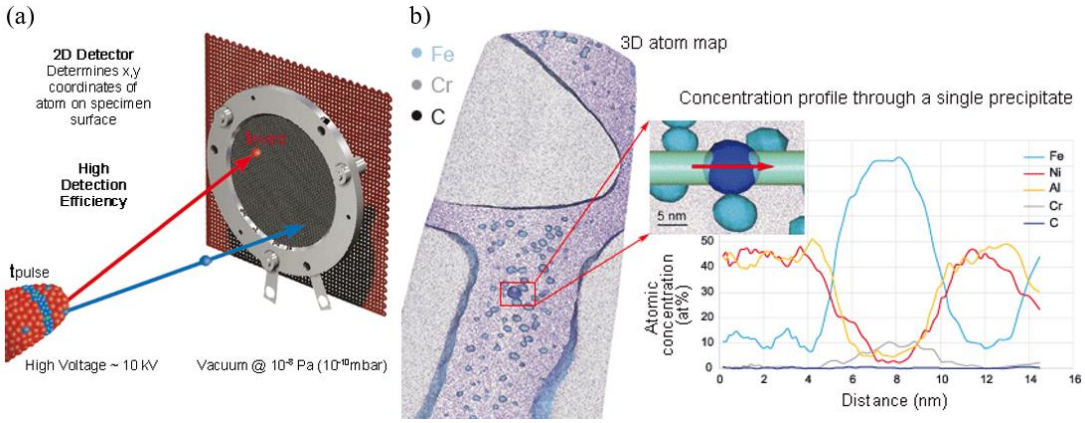

Figure 1. 18 (a) Illustration of APT design and working principles and (b) representative tomography of a Fe-Cr-C sample with its concentration profile. Adopted from [45].

APT samples are prepared in a form of very sharp tip generally by techniques such as electro-polishing or focused ion beam milling. Within the APT instrument sample is cooled down to temperatures such as 20-50 K and. Voltage of 3-15 kV is applied to the sample in order to induce an electrostatic field at the tip which must be not high enough to evaporate atoms. Later on, depending on the type of instrument either laser or voltage pulsing is applied in order to evaporate few atoms from the surface. Evaporated atoms then travel to Position Sensitive Detector (PSD). Repeating the whole procedure again and again, 3D tomography image of collected atoms is generated in computer. Thus, any kind of chemical heterogeneities such as phase separations, precipitations and crystallization can be imaged by APT in atomic scale.

1.8.5. Macro and Micropillar Compression Tests

Behaviors of metallic glasses under tensile, compressive, bending or impact loading gives valuable information about their structures and possible application areas in future. Metallic glasses can show inhomogeneous or homogenous deformation characteristics depending on the composition of the alloy or temperature and strain rate of the experiment. By conducting in-situ high temperature mechanical testing researchers can reveal deformation behavior of metallic glasses. Stress-strain curves obtained from these experiments give valuable information related to their shear band stability. Most metallic glasses show discrete strain burst events during loading, revealing a serrated stress-strain curve. Each serration represents a shear banding event that is either nucleation or propagation. These events can be evaluated in order to understand ductility of metallic glasses.

Micro-pillar compression tests are a recently developed mechanical characterization technique which enables researchers to perform mechanical testing where sample geometry is not suitable for macro mechanical testing. Researchers can also investigate size effect in a wide range where sample diameter varies from values as low as 0.3-0.5 μm to 3-5 μm through micropillars compression tests [46]. Fig. 1.19 depicts deformed micropillars after micropillar compression tests at various temperatures. The shift in deformation behaviour is apparent in scanning electron microscope (SEM) images.

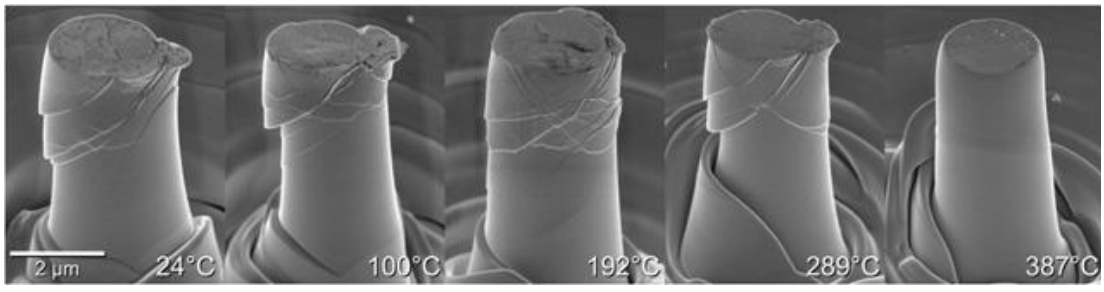

Figure 1. 19 (a) Deformed pillars at various temperatures, ilustrating the shift from inhomogenous to homogenous deformation as temperature increases. Adopted from [46].

One drawback of micro-pillar compression tests are samples may exhibit a tapper angle due to poor focused ion beam (FIB) milling. Where tapper angle is 5^{o} or higher, there occurs a significant error in observed stiffness. But lower tapper angles such as 2^{o} are generally considered as accaptable [47-48].

1.9. Thesis Organization

The scope of this thesis is to investigate the effect of Sm micro alloying on structural and mechanical properties of Zr-Cu-Al bulk metallic glass. In this respect, thesis consists of five chapters. The first chapter includes the brief introduction and literature review on major aspects of metallic glasses. In the second chapter, effect of Sm micro alloying on glass forming ability of $(Zr_{50}Cu_{40}Al_{10})_{100-x}Sm_x$ (x=0, 1, 3, 4 at. %) partially crystalline suction cast rods were investigated using differential scanning calorimetry (DSC), X-ray diffraction (XRD), scanning electron microscopy (SEM) and mechanical testing. The highest GFA was achieved in partially amorphous $(Zr_{50}Cu_{40}Al_{10})_{96}Sm_4$ suction-cast rod. In the third part, thermal stability and crystallization kinetics of cast rods and melt-spun ribbons of $(Zr_{50}Cu_{40}Al_{10})_{96}Sm_4$ alloys were investigated using DSC, XRD, transmission electron microscopy (TEM) and atom probe tomography (APT). Sm micro alloying was found to trigger Cu_2Sm nanocrystallization. In the fourth chapter, mechanical characterization is performed using compression tests, hardness tests and micropillar compression tests. Sm micro alloying deteriorate the mechanical properties by decreasing hardness and fracture strength in as-cast state; however, annealing induced Cu_2Sm nanocrystals improved both hardness and fracture strength of the nanocrystalline/amorphous composite sample of $(Zr_{50}Cu_{40}Al_{10})_{96}Sm_4$ alloy. Shear band propagation speed of composite sample found to be extremely unstable which causes brittle fracture. In the fifth chapter, thesis is concluded by major remarks and future recommendations.

CHAPTER 2

EFFECT OF RARE-EARTH MICROALLOYING ON GLASS FORMING ABILITY AND MECHANICAL PROPERTIES OF Cu-Zr-Al BULK METALLIC GLASSES

2.1. Introduction

Regarding their unique and noteworthy combinations of properties, glass formation has been investigated in numerous systems, leading to the development of several so-called bulk metallic glasses (BMGs). Motivated by the potential technological benefits of designing new advanced engineering and structural materials; efforts have been given to develop alloy systems with high glass forming ability (GFA) to attain new properties or enhance their properties and functionality.

In this chapter, effect of Sm addition on properties such as GFA, thermal stability and mechanical properties of $(Zr_{50}Cu_{40}Al_{10})_{100-x}Sm_x$ (x=0, 1, 3, 4 at. %) suction cast rods were investigated via combined study of XRD, DSC, SEM and mechanical tests.

2.2. Literature Review

2.2.1. Cu-Zr Metallic Glasses

Among many other glass former systems, Cu-Zr binary alloys are particularly interesting for mechanical and structural applications because of their wide composition range of GFA; starting from 35 to 70 at. % Cu in alloys and appreciable compressive plasticity which prevents any catastrophic failures. Fig.2.1 shows Cu-Zr phase diagram illustrating approximate glass forming range along with structures of commonly observed intermetallic phases. There are several studies concerning the glass formation, kinetics and phase transformation mechanisms during devitrification

in Cu-Zr binary systems [44-49]. These studies revealed several details concerning crystallization transformations involving the phases, the kinetics of the crystallization of individual phases under isothermal and constant-heating conditions, structural dynamics associated with devitrification in Cu-Zr binary systems.

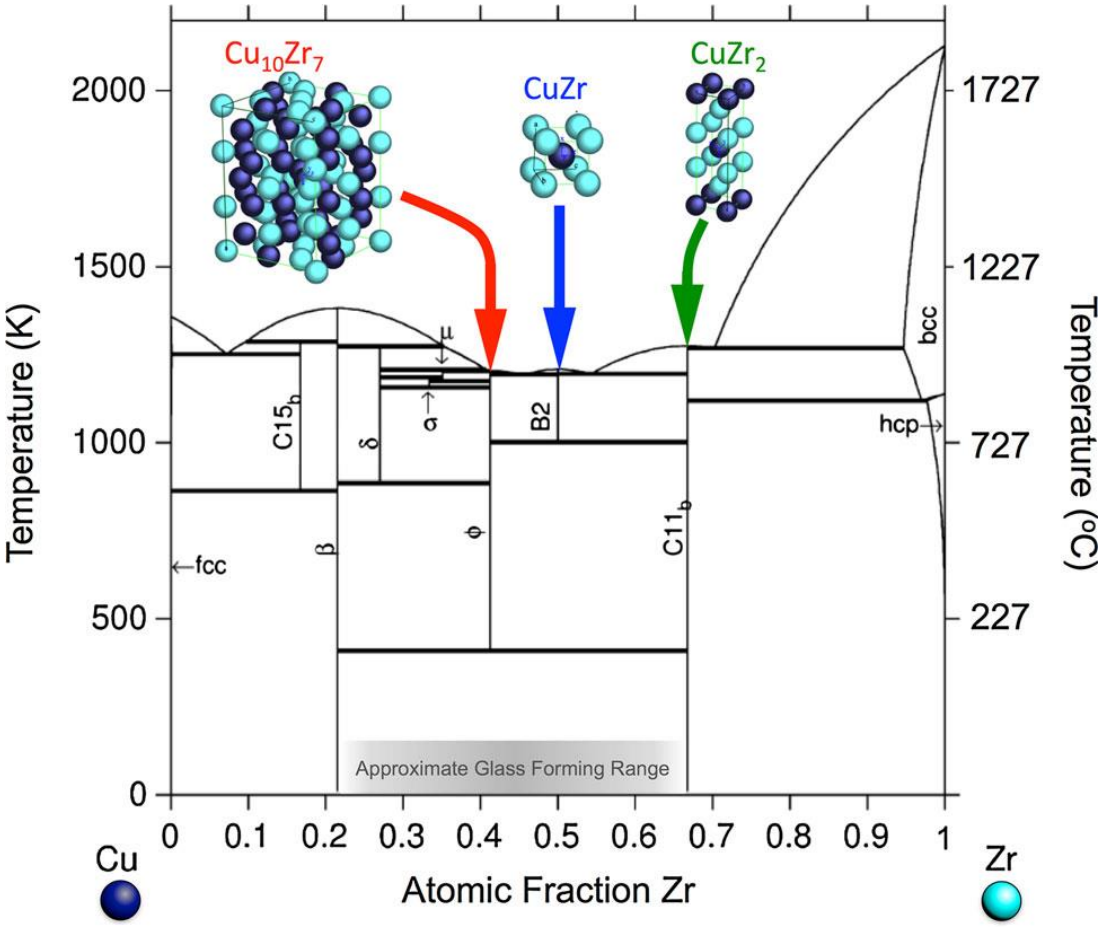

Figure 2. 1 Cu-Zr phase diagram showing approximate glass forming range. Adopted from [50].

According to the literature, GFA is a nonlinear function of Cu composition in case of Cu_xZr_{100-x} binary alloys. Highest GFA has been achieved for 50 at. % Cu, then 65.5 at. % comes next, and then 46 at. % Cu. Although GFA for Cu-Zr binary alloys are quite high, bulk production of Cu-Zr metallic glasses are limited to 2 mm [51].

2.2.2. Cu-Zr-TM Metallic Glasses

In Cu-Zr binary system, recent studies have reported that the GFA of Cu-Zr system increases significantly with an addition of third element, especially one of the transition metals (TM), such as Al**,** Ti, Ni or Ag [52]. Among ternary Cu-Zr-TM systems, Cu-Zr-Al alloys have attracted much attention due to their high GFA and superior mechanical properties. However, since the maximum critical diameter sizes of Cu-Zr-Al BMGs are quite low compared to Be or Pd containing BMGs, the efforts are given to increase the GFA of Cu-Zr-Al BMG [53].

Wang *et. al.* showed best glass forming regions within Cu-Zr-Al ternary system. According to their studies $Zr_{48}Cu_{45}Al_7$, $Zr_{45}Cu_{49}Al_6$, $Zr_{54}Cu_{38}Al_8$ and $Zr_{56}Cu_{36}Al_8$ compositions were determined to be the best glass formers and their GFA significantly changed with even 1 at. % shift in composition. These best glass formers were surrounded by amorphous/crystalline composite former compositions. Table 2.1 shows the results of DSC and DTA analysis of 5 mm cast ingots of Zr-Cu-Al alloys [52].

Table 2. 1 Thermal parameters of various alloys in Zr-Cu-Al ternary system [52].

Results of DSC and DTA analysis of 5 mm cast ingots of Zr–Cu–Al alloys in the τ_3-τ_5-ZrCu eutectic system

Alloy label	Composition	Morphology	T_m (K)	T_l (K)	T_g (K)	T_x (K)	T_{rg}	ΔT_x (K)	γ	ΔH_x (J/g)
8	$Zr_{50}Cu_{34}Al_{16}$	Fully crystalline in the center	1123	1209	–	–	–	–	–	0
2	$Zr_{50}Cu_{36}Al_{14}$		1121	1188	724	771	0.609	47	0.403	28
1	$Zr_{50}Cu_{38}Al_{12}$	Composite:	1122	1170	722	774	0.617	52	0.409	44
7	$Zr_{50}Cu_{40}Al_{10}$	(amorphous + τ_3)	1122	1176	714	770	0.607	56	0.407	46
55	$Zr_{50}Cu_{43}Al_7$		1122	1181	703	763	0.595	60	0.405	52
11	$Zr_{46}Cu_{42}Al_{12}$	Fully crystalline in the center	1123	1262	–	–	–	–	–	–
39	$Zr_{46}Cu_{44}Al_{10}$	Composite:	1125	1223	726	782	0.594	56	0.401	47
40	$Zr_{47}Cu_{45}Al_8$	(amorphous + τ_5)	1125	1218	714	772	0.586	58	0.400	54
64	$Zr_{49}Cu_{44}Al_7$		1126	1184	704	764	0.595	60	0.405	59
67	$Zr_{48}Cu_{45}Al_7$		1125	1186	708	766	0.597	58	0.404	59
56	$Zr_{49}Cu_{45}Al_6$	Fully amorphous	1126	1187	704	758	0.593	54	0.401	58
45	$Zr_{48}Cu_{46}Al_6$		1125	1192	706	762	0.592	56	0.401	58
57	$Zr_{49}Cu_{46}Al_5$	Composite:	1126	1195	701	750	0.587	49	0.396	29
62	$Zr_{49}Cu_{47}Al_4$	(amorphous + ZrCu)	1126	1208	697	745	0.577	48	0.391	21

In a recent study, Yokoyama *et. al.* showed the ternary eutectic point as $Zr_{50}Cu_{40}Al_{10}$ within Zr-Cu-Al systems. Fig.2.2 (a) shows the thermal volume change with respect to Zr concentration (at. %) for Zr-Cu-Al metallic glasses. Fig.2.2 (b) shows Zr-Cu-Al phase diagram indicating eutectic point and corresponding volume change.

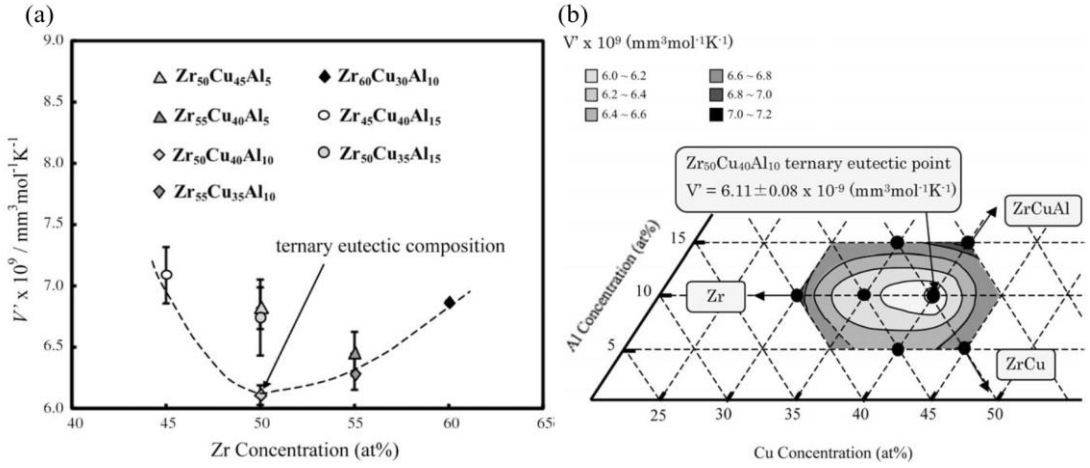

Figure 2. 2 Thermal volume change with respect to Zr concentration (at. %) for Zr-Cu-Al liquids and (b) Zr-Cu-Al ternary phase diagram. Adopted from [54].

It is clear that $Zr_{50}Cu_{40}Al_{10}$ composition has the lowest thermal volume expansion in order to stabilize the excess free volume during vitrification. Thus in their work, Yokoyama *et. al.* concluded eutectic point, $Zr_{50}Cu_{40}Al_{10}$ as the best glass former [54].

2.2.3. Cu-Zr-Al-RE Metallic Glasses

Recent studies indicated an increase in GFA of quaternary Cu-Zr-Al-X [X= Ag, Ce, Pr, Tb, Gd] alloys prepared by the addition of fourth element [55-56]. Besides the addition of transition metals to Cu-Zr-Al alloys, it has been reported that addition of rare-earth elements (RE) results in remarkable enhancement in GFA and mechanical properties of Cu-Zr-Al alloys by increasing the stability of supercooled liquid and reduced glass transition temperature (T_{rg}). For instance, it has been shown that Lu, Y and Dy rare-earths increase GFA in $Cu_{47}Zr_{45}Al_8$ alloy. Fig.2.3 (a) shows macro images of 20 and 25 mm diameter suction cast rods and Fig.2.3 (b) shows XRD patterns of $(Cu_{47}Zr_{45}Al_8)_{100-x}Y_x$ alloy system. Minor Y addition increases critical casting diameter from 15 mm to 25 mm [57].

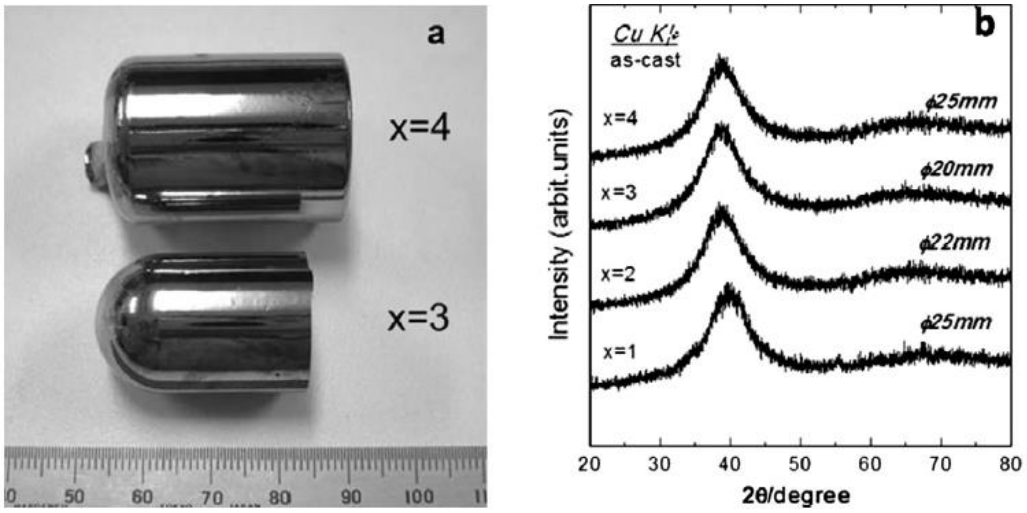

Figure 2. 3 Macro images of $(Cu_{47}Zr_{45}Al_8)_{100-x}Y_x$ suction cast rods and corresponding XRD patterns. Adopted from [57].

Deng *et. al.* also reported that the amorphous samples of $(Cu_{47}Zr_{45}Al_8)_{97}Lu_3$ with a plastic strain of 4.65 % can be obtained. Fig 2.4 shows compressive stress-strain diagrams for $(Cu_{47}Zr_{45}Al_8)_{100-x}Lu_x$ (x = 0–4 at. %). Plasticity increases with addition of Lu up to 3 at. %. Further Lu addition is found to deteriorate the ductility [57]. Such effects on mechanical properties are not only limited to Lu.

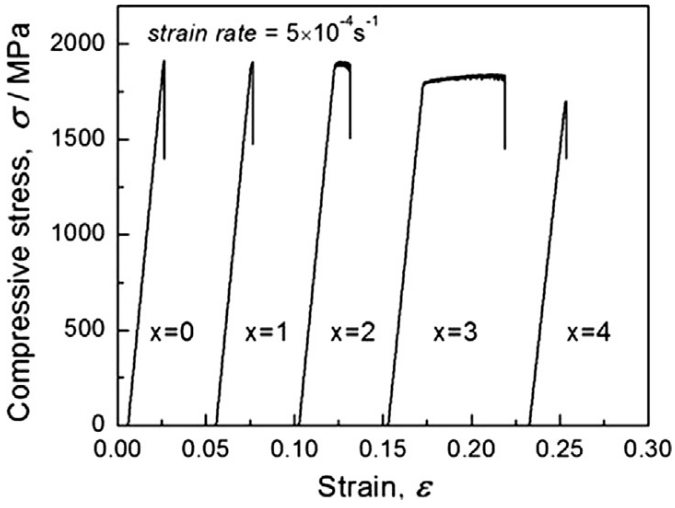

Figure 2. 4 Compressive stress–strain curves of as-cast $(Cu_{47}Zr_{45}Al_8)_{100-x}Lu_x$ (x = 0–4 at. %) glassy rods with a diameter of 2 mm. Adopted from [57].

In Fig.2.5 (a) and (b), effect of Gd and Y addition on Zr-Cu-Al metallic glasses are shown. Plasticity is increased by addition of rare-earth elements at first; however, plasticity significantly decreased with further addition. Maximum ductility is achieved at different values of rare-earth element content as seen in Fig.2.5. For instance in case of further addition of Gd after 3 at. %, plasticity decreases; however, for Y micro alloyed samples maximum ductility is achieved at 2 at. % and samples remain relatively ductile even at 5 at. %.

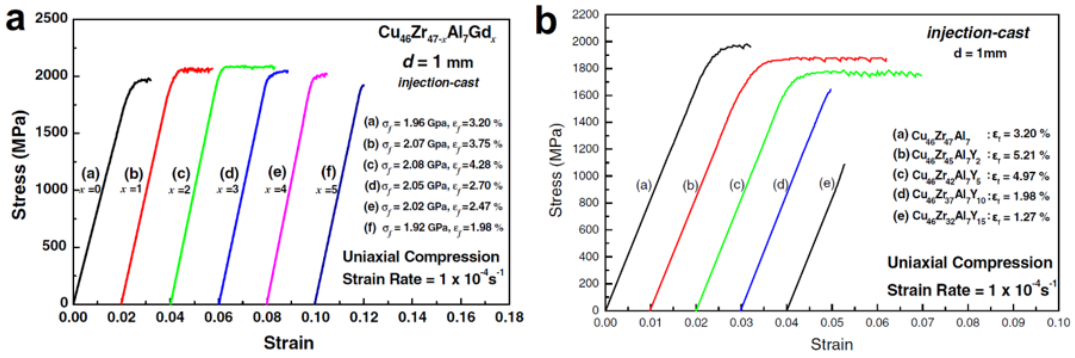

Figure 2. 5 Compressive stress–strain curves of injection-cast (a) $Cu_{46}Zr_{47-x}Al_7Gd_x$ (x = 0–5 at. %) and (b) $Cu_{46}Zr_{47-x}Al_7Y_x$ (x = 0–15 at. %) glassy rods with a diameter of 1 mm. Adopted from [58] and [59] respectively.

Decrease in plasticity with further rare-earth element addition is also observed in SEM images of fracture surfaces due to the shifting in the fracture modes. Fig.2.6 shows fracture surfaces of compression test samples after fracture. Fracture surface of Y free $Cu_{46}Zr_{47}Al_7$ metallic glass is seen in Fig.2.6 (a) illustrating that sample fails in a shear fracture mode where fracture surface is covered with vein patterns. In Fig.2.6 (c), shift in fracture mode can be seen as the effect of 10 at. % Y addition. Ductile fracture features, namely vein patterns or branched shear bands disappear and fracture surface becomes very smooth [58-59].

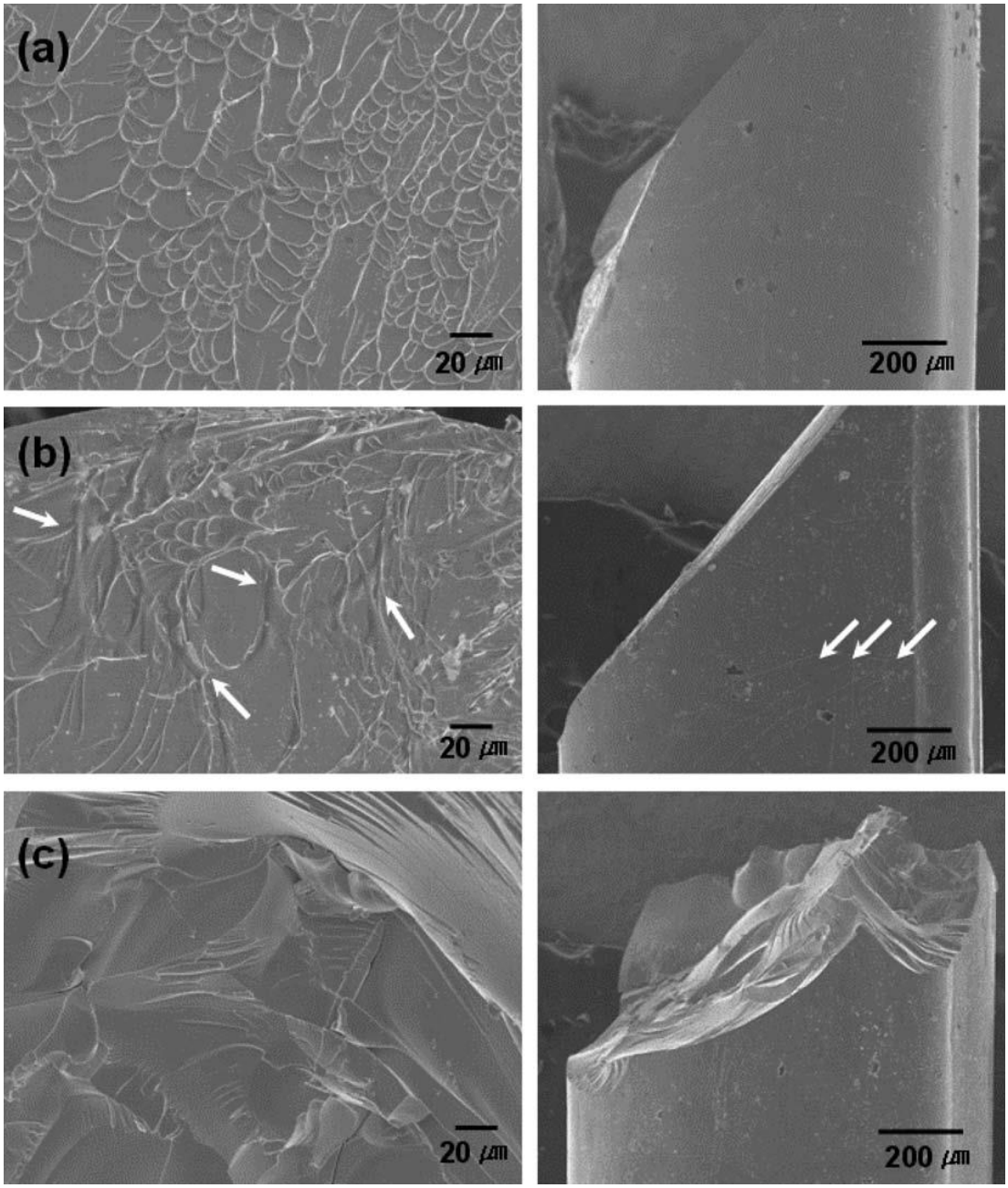

Figure 2. 6 SEM images of fracture surfaces of suction-cast $Cu_{46}Zr_{47-x}Al_7Y_x$ glassy rods with a diameter of 1 mm: (a) x=0, (b) x=5, (c) x=10. Adopted from [59].

2.3. Experimental Procedure

2.3.1. Production of Alloys

The alloy ingots with nominal compositions of $(Zr_{50}Cu_{40}Al_{10})_{100-x}Sm_x$ (x= 0, 1, 3, 4 at. %) were prepared by arc-melting from high purity elements (0.995 Zr, 0.999 Cu and 0.999 Al, by weight) under a Ti-gathered argon atmosphere at 5-8 mbar pressure at Çankaya University. Ti-gathering is done in order to eliminate remaining O_2 within chamber after vacuum sealing to $10^{-3} – 10^{-4}$ mbar. The ingots were remelted three times for a better chemical homogeneity. Before each melting process samples were flipped upside down to enhance homogeneity.

Ingots are then cast into 1, 2 and 3 mm diameter copper molds via suction casting. Fig.2.7 shows Edmund Bühler MAM-1 device that is used in this study. In order to perform casting, vacuum reservoir shown in Fig.2.7 (a) is vacuumed and vacuum reservoir connection (VRC) pipe connected to copper hearth stage while stage is vacuum tight. After air pressure is lowered down to $10^{-3} – 10^{-4}$ mbar, chamber is purged with Ar gas. A pressure gradient is generated from chamber to vacuum reservoir through VRC pipe as vacuum reservoir is under vacuum and chamber is at positive Ar pressure. Pressure gradient originated gas flow is controlled by valve switch shown in Fig.2.7 (a). Molten metal is pushed into the Cu mold seen in Fig.2.7 (b) by Ar gas flow that is generated by opening of valve switch. Cu molds are embedded into copper hearth stage as seen in Fig.2.7 (c) and cooled by water to produce high cooling rate (1-100 K/s). So, cast melt is rapidly quenched and solidified into cylindrical rod shape.

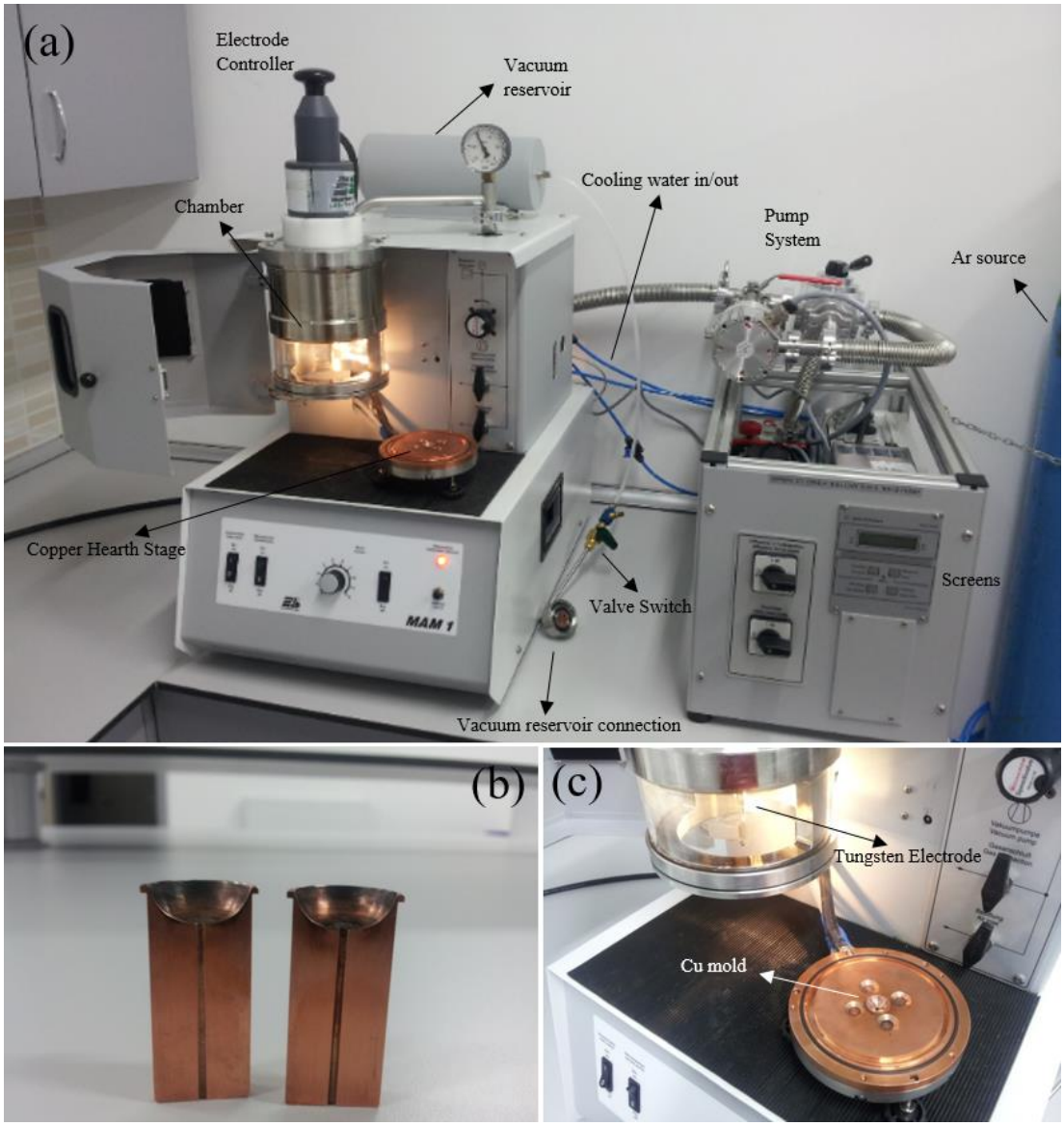

Figure 2. 7 Edmund Bühler MAM-1 device at Çankaya Uni. with important features labeled.

2.3.2. X-ray Diffraction and Differential Scanning Calorimetry Analysis

X-ray Diffraction Analysis

The amorphous nature of suction-cast rods was investigated and confirmed by X-ray diffraction (XRD). XRD measurements were collected using D8 Advance Bruker X-ray Diffractometer shown in Fig.2.8. Surface of the suction cast rod samples are grinded in order to remove any oxide layer. XRD measurements are done from rod samples in bulk form. X-ray tube of the diffractometer is shown in Fig.2.8 (b), which has a Cu K_α (λ = 1.5406 Å) anode with Ni filters. Diffractometer operated at 40 kV voltage and 30 mA current and data collected in a range from 10^o to 90^o at a scan rate of 0.5^o/min.

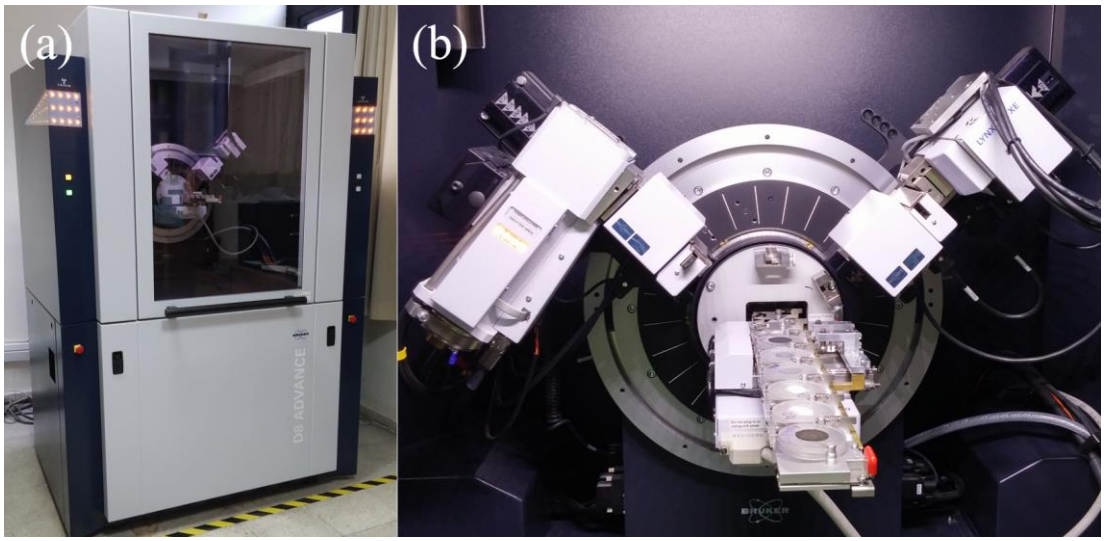

Figure 2. 8 Photographs of D8 Advance Bruker X-ray Diffractometer showing (a) outer view and (b) goniometer, X-ray tube, X-ray detector and sample holders.

Differential Scanning Calorimetry Analysis

Differential scanning calorimetry (DSC) analysis of rods was carried out using Perkin Elmer and Seiko 7000 DSC as seen in Fig.2.9 (a) at a heating rate of 0.17 K/s (10 ^{o}C/min).

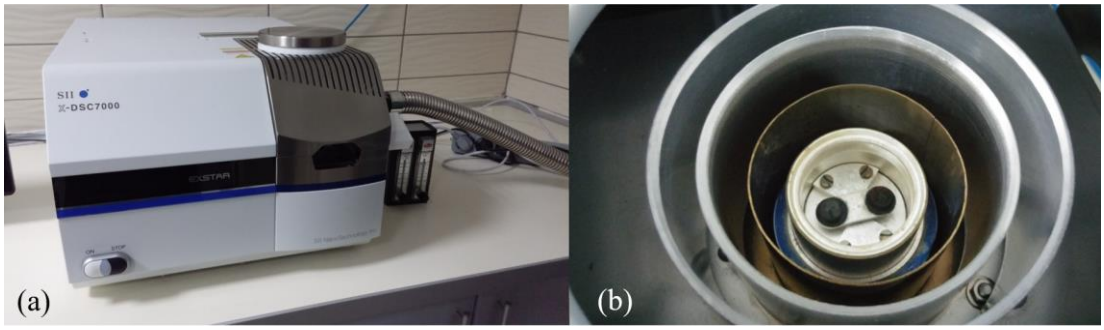

Figure 2. 9 (a) DSC equipment used in this thesis along with (b) photograph of inner chamber where metallic glass sample and reference sample are located.

Before DSC measurements samples are cut from cast rods with a clean side chisel into pellet shapes. Each pellet sample weighed approximately 10-20 miligrams. Samples are then encaplusated into aluminum pans and covers. Enclosed aluminum pans are placed onto black holders seen in Fig.2.9 (b). Sample is placed on top of one holder and reference sample that is the empty aluminum pan and cover is placed on top of other holder. Samples are heated from room temperature to 773 K (500 ^{o}C) under a protective N_2 atmosphere.

2.3.3. Mechanical Tests and Fracture Analysis

The mechanical properties of the rods were investigated under compressive load by using Instron 5582 mechanical testing equipment with max. 100 kN shown in Fig.2.10 (a). Specimens were prepared for compressive test according to the ASTM standards, with the gauge dimensions of 3.0 ± 0.3 mm in diameter and 6.0 ± 0.3 mm in length (with an aspect ratio of 2:1). The surfaces of the rod specimens were polished in order to ensure the surfaces of the samples were parallel and perpendicular to the loading axis. The uniaxial compression tests were conducted with the crosshead speed of 0.03 mm/min and corresponding average strain rate of 10^{-4} s^{-1} at room temperature. The fracture morphologies of the loaded samples were examined using FEI Nova NanoSEM 430 scanning electron microscope (SEM) seen in Fig.2.10 (b).

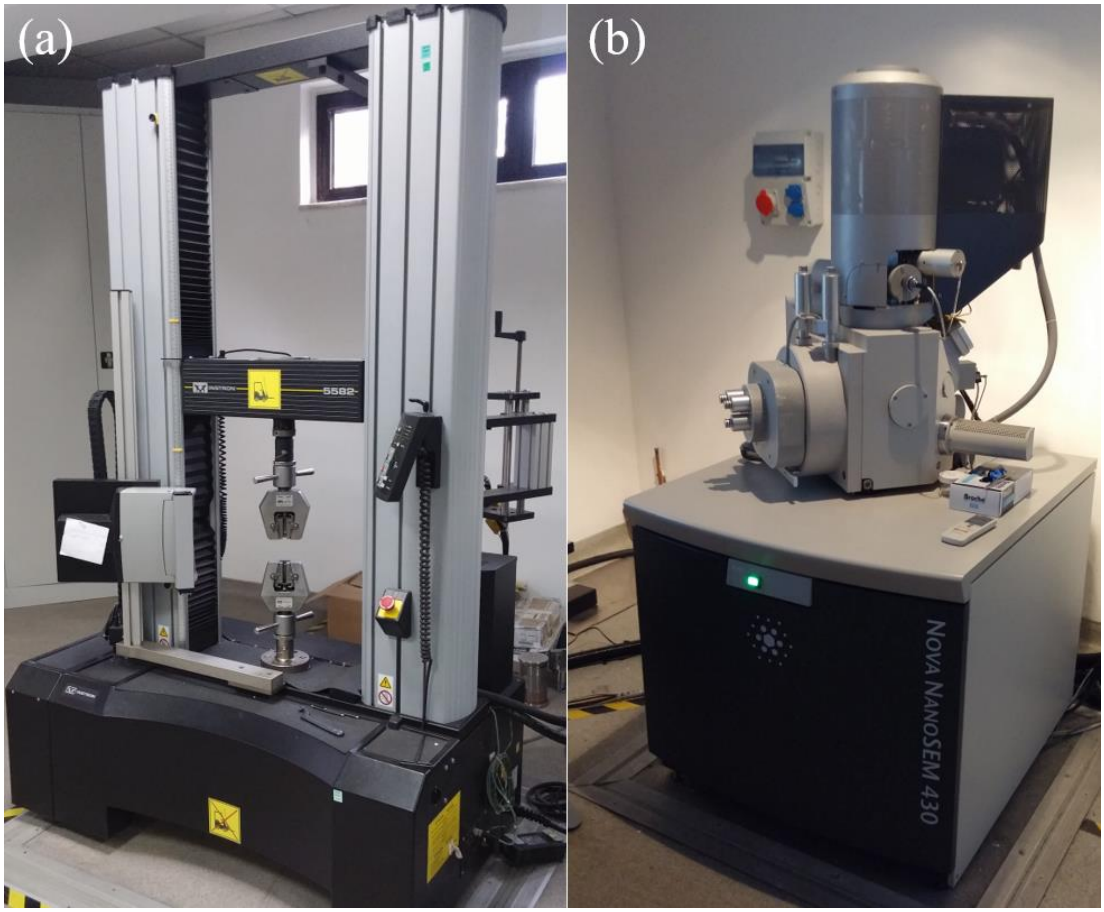

Figure 2. 10 Photographs of (a) Instron 5582 mechanical testing equipment and (b) FEI scanning electron microscope used in this study.

2.4. Results and Discussion

The 1, 2 and 3 mm diameter suction-cast rods of $Zr_{50}Cu_{40}Al_{10}$, $(Zr_{50}Cu_{40}Al_{10})_{99}Sm_1$, $(Zr_{50}Cu_{40}Al_{10})_{97}Sm_3$, $(Zr_{50}Cu_{40}Al_{10})_{96}Sm_4$ alloys, seen in Fig.2.11, were cut according to the aspect ratio and grinded to achieve parallel end surfaces.

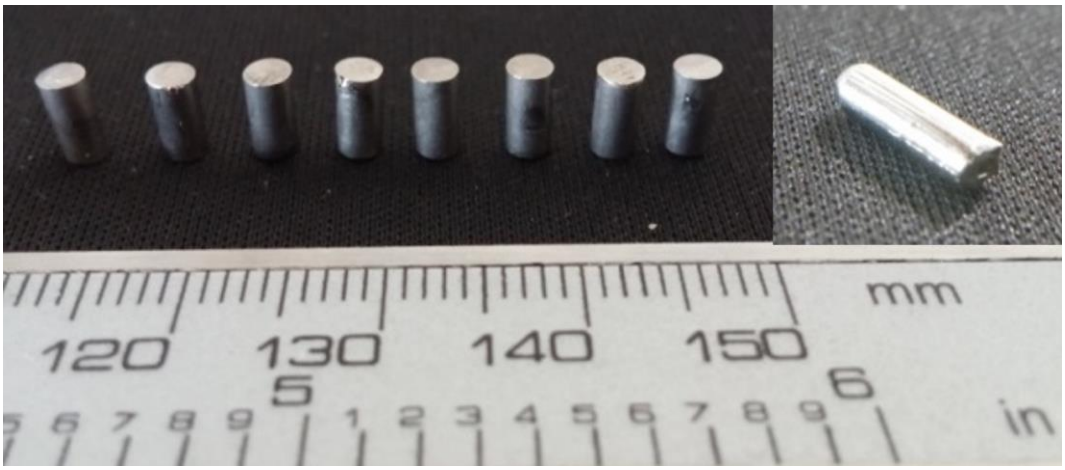

Figure 2. 11 The 3 mm diameter suction-cast rods prepared with an aspect ratio of 2 for the compression test. Inset shows one of the suction cast rods.

2.4.1. X-Ray Diffraction Results

The XRD patterns of 1, 2 and 3 mm diameter suction-cast $Zr_{50}Cu_{40}Al_{10}$ rods, given in Fig.2.12 (a) reveal the crystalline structure where the crystalline phases were labeled as CuZr (B2) and CuZr (B19'). The XRD patterns for $(Zr_{50}Cu_{40}Al_{10})_{99}Sm_1$, in Fig.2.12 (b) show the partially amorphous structure for 1 and 2 mm diameter rods where CuZr (B2) crystals were produced during solidification of alloys and embedded in the amorphous matrix. The XRD pattern of 3 mm diameter $(Zr_{50}Cu_{40}Al_{10})_{99}Sm_1$ rod in Fig.2.12 (b) indicates the solidification products as martensitic CuZr (B19') and CuZr (B2) phases.

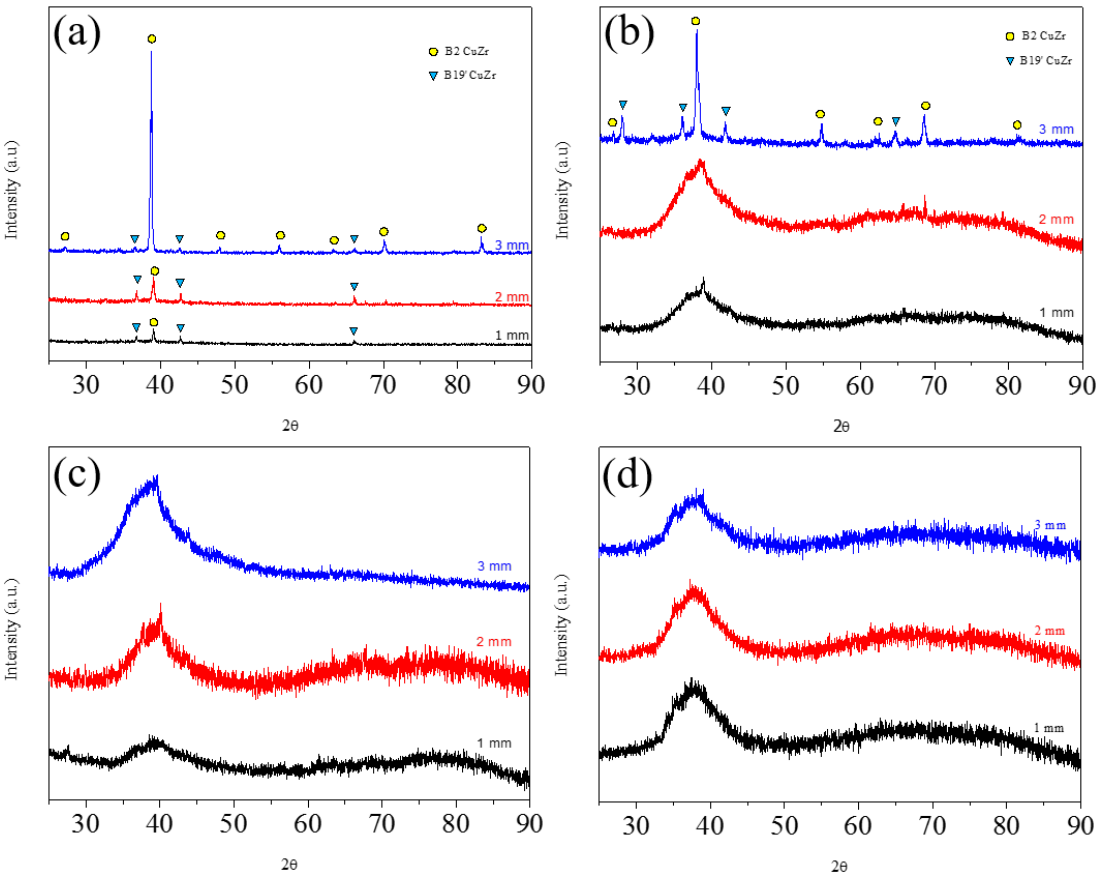

Figure 2. 12 XRD patterns of 1, 2 and 3 mm diameter suction-cast (a) $Zr_{50}Cu_{40}Al_{10}$; (b) $(Zr_{50}Cu_{40}Al_{10})_{99}Sm_1$; (c) $(Zr_{50}Cu_{40}Al_{10})_{97}Sm_3$ and (d) $(Zr_{50}Cu_{40}Al_{10})_{96}Sm_4$ rods.

The XRD patterns in Fig.2.12 (c) indicate partially amorphous structure where CuZr (B2) crystals embedded in amorphous matrix for all 1, 2 and 3 mm diameter $(Zr_{50}Cu_{40}Al_{10})_{97}Sm_3$ suction-cast rods. Fig.2.12 (d) represents only the diffuse scattering peaks related to the amorphous structure of 1, 2 and 3 mm diameter $(Zr_{50}Cu_{40}Al_{10})_{96}Sm_4$ suction-cast rods. The XRD analysis illustrated the crystalline structure of 1, 2 and 3 mm diameter suction-cast rods of $Zr_{50}Cu_{40}Al_{10}$ which solidifies into CuZr (B2) and CuZr (B19') phases. The XRD data collected from $(Zr_{50}Cu_{40}Al_{10})_{99}Sm_1$ revealed the partially amorphous structure reinforced with CuZr (B2) crystals for 1 and 2 mm diameter rods while 3 mm diameter $(Zr_{50}Cu_{40}Al_{10})_{99}Sm_1$ rod was found to solidify into martensitic CuZr (B19') and CuZr (B2) phases. CuZr

(B2) phase is a high temperature phase, but it may be synthesized during the rapid cooling of Cu-Zr based binary and multi component systems. The main difference between the solidification products of these three suction-cast rods of $(Zr_{50}Cu_{40}Al_{10})_{99}Sm_1$ depends on the cooling rate differences; such as the lower cooling rate will be achieved for the larger diameter rods. With an increase in Sm concentration up to 3 at. %, $(Zr_{50}Cu_{40}Al_{10})_{97}Sm_3$ suction-cast rod solidifies into partially amorphous precursor with CuZr (B2) crystals. It is obvious that while increasing the Sm concentration, the formation of martensitic CuZr (B19') phase is hindered and CuZr (B2) crystals embed in the amorphous matrix. Higher portion of amorphous structure was obtained for 1, 2 and 3 mm diameter $(Zr_{50}Cu_{40}Al_{10})_{96}Sm_4$ suction-cast rods. Although it is known to be a good glass former, it was not possible to produce fully amorphous samples of $Zr_{50}Cu_{40}Al_{10}$ composition with our experimental setup in Çankaya University. However, the XRD analysis of four alloys reveals how the minor addition of Sm effects the GFA of Cu-Zr-Al system. Crystalline peaks diminish while their intensity decreases and diffuse main amorphous hump becomes more dominant as Sm content increases. It is important to note that the GFA increases with the Sm addition in the range of 1 to 4 at. % and the highest GFA is achieved for $(Zr_{50}Cu_{40}Al_{10})_{96}Sm_4$.

2.4.2. Scanning Electron Microscope Images

Scanning electron microscope images of cut surfaces of 1 mm diameter suction-cast rod samples of $(Zr_{50}Cu_{40}Al_{10})_{100-x}Sm_x$ (x=0, 1, 3, 4) alloys are shown in Fig.2.13. Fully crystalline nature of $Zr_{50}Cu_{40}Al_{10}$ alloy can be emphasized from the cleavage fracture surfaces in Fig.2.13 (a) and (b). Cut surface appears to be quite homogenous for Sm-free alloy sample.

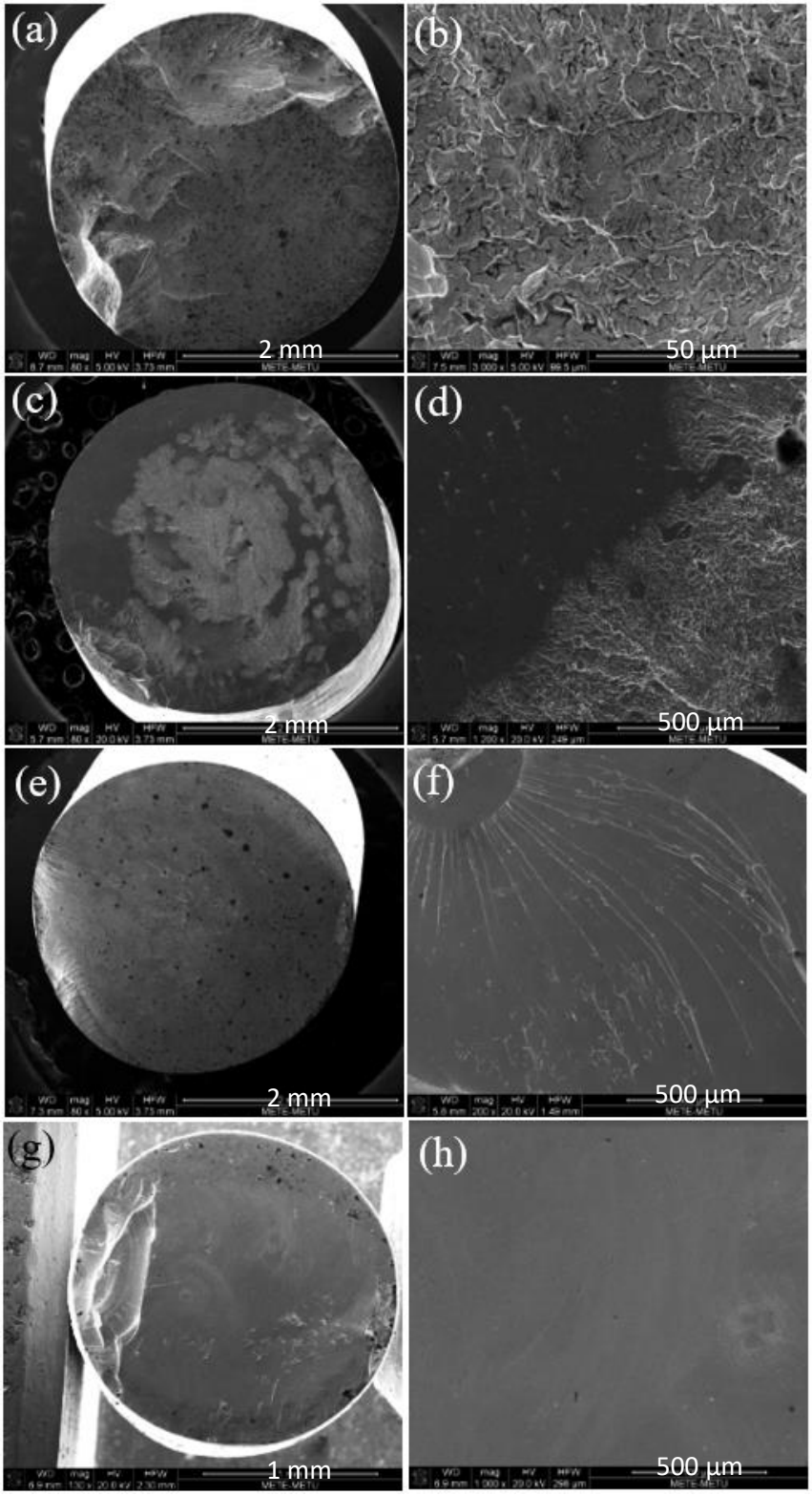

Figure 2. 13 SEM images of 1 mm diameter suction-cast rod samples of $(Zr_{50}Cu_{40}Al_{10})_{100-x}Sm_x$ where x=0 (a, b), x=1 (c, d), x=3 (e, f), x=4 (g, h).

Cut surfaces of the $(Zr_{50}Cu_{40}Al_{10})_{99}Sm_1$ alloy are shown in Fig.2.13 (c) and (d) revealing a heterogeneous surface. It is evident that surface contains 2 distinct fracture characteristics, where sample core exhibit brittle cleavage fracture surface while outer rim contains smooth mirror-like surface for this sample. Considering fracture surfaces of metallic glasses, smooth mirror-like surface is thought to be due to amorphous nature of outer rim. Such heterogeneity in $(Zr_{50}Cu_{40}Al_{10})_{99}Sm_1$ sample is caused by the cooling rate difference between sample core and rim during solidification. Higher cooling rate achieved at the sample rim was sufficient enough to synthesis amorphous structure, while lesser cooling at the core of the sample could not suppress crystallization. Cut surfaces of $(Zr_{50}Cu_{40}Al_{10})_{97}Sm_3$ and $(Zr_{50}Cu_{40}Al_{10})_{96}Sm_4$ alloys are illustrated in Fig.2.13 (e, f) and Fig.2.13 (g, h) respectively. Both of these samples appear to have a rather smooth surface, where $(Zr_{50}Cu_{40}Al_{10})_{97}Sm_3$ sample surface contains a few shear band river marks and $(Zr_{50}Cu_{40}Al_{10})_{96}Sm_4$ sample surface is completely smooth. Increased amorphous proportion can also be illustrated considering the smooth surface fractions within the cut sample surfaces. As Sm content increases, smooth regions on sample surfaces becomes dominant revealing increased amount of glassy phase and thus increased GFA of the alloy system.

2.4.3. Differential Scanning Calorimetry Results

The amorphous nature of the alloys for 1 mm diameter suction-cast rods was further checked by DSC analysis, given in Fig.2.14, which shows the continuous heating DSC data obtained at a heating rate of 10 K/min. Each DSC trace given in Fig.2.14 indicates a glass transition feature followed by an exothermic peak associated with the crystallization. From these DSC traces, thermal data including the parameters to define GFA of the alloys, such as the glass transition temperature (T_g), the onset temperature of crystallization (T_x), the crystallization peak temperature (T_p), and supercooled liquid region (ΔT_x ($=T_x-T_g$)) were obtained at a heating rate of 10 K/min and listed in Table 2.2.

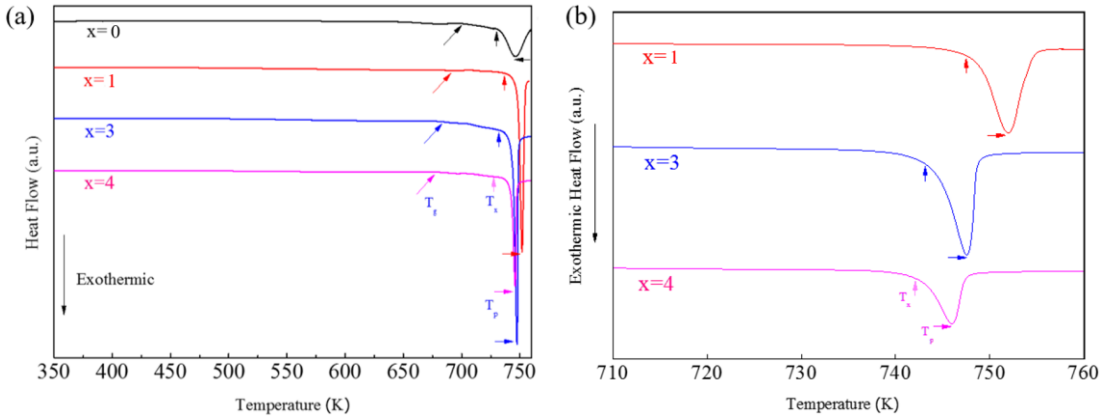

Figure 2. 14 Isochronal DSC traces of 1 mm diameter suction-cast rods of $(Zr_{50}Cu_{40}Al_{10})_{100-x}Sm_x$ (x=0, 1, 3, 4 at. %) alloys at 10 K/min. The characteristic temperatures of T_g, T_x and T_p were also labeled on each trace.

Table 2. 2 Thermal data obtained at 10 K/min from DSC traces for 1 mm diameter partially crystalline rods of $(Zr_{50}Cu_{40}Al_{10})_{100-x}Sm_x$ (x= 0, 1, 3, 4 at. %) alloys.

Composition	T_g	T_x	ΔT
$Zr_{50}Cu_{40}Al_{10}$	700	730	30
$(Zr_{50}Cu_{40}Al_{10})_{99}Sm_1$	686	749	63
$(Zr_{50}Cu_{40}Al_{10})_{97}Sm_3$	683	744	61
$(Zr_{50}Cu_{40}Al_{10})_{96}Sm_4$	681	741	60

The amorphous nature of the alloys was further confirmed by the constant-heating-rate DSC analysis that illustrates a glass transition followed by single step crystallization. Regarding our XRD analysis, three alloys; $(Zr_{50}Cu_{40}Al_{10})_{99}Sm_1$, $(Zr_{50}Cu_{40}Al_{10})_{97}Sm_3$, $(Zr_{50}Cu_{40}Al_{10})_{96}Sm_4$ show higher amount of amorphous portion compared to that of $Zr_{50}Cu_{40}Al_{10}$ (can be accepted as nearly fully crystal). Due to its crystalline nature thermal properties of $Zr_{50}Cu_{40}Al_{10}$ composition was not investigated in detail. As CuZr crystals are in high amount for this sample, it would not be representative to comment on T_g and T_x and as a result ΔT for this composition from rod samples. Supercooled liquid range, ΔT for $Zr_{50}Cu_{40}Al_{10}$ was found as 30 K, which is considerably low

compared to Sm micro-alloyed samples. It is important to notice that this difference in ΔT is not caused by Sm addition but due to crystalline nature of $Zr_{50}Cu_{40}Al_{10}$ rods. Higher ΔT is associated with a thermally stable metallic glass; however, in case of $Zr_{50}Cu_{40}Al_{10}$ rods glassy phase is unstable since crystalline phases already present and tend to grow with increased atomic mobility during heating. In order to discuss the effect of Sm on thermal stability of $Zr_{50}Cu_{40}Al_{10}$ metallic glass, it would be suitable to compare concentration range from 1 at. % to 4 at. % Sm. It is observed that increasing the Sm concentration from 1 to 4 at. % decreases the T_g from 686 K to 681 K and the T_x from 749 K to 741 K and also decreases the ΔT_x slightly (3 K). It seems that even the glass formation in Cu-Zr-Al-Sm alloys increases, which is supported by XRD findings as well, the thermal stability of supercooled liquid region is decreasing with Sm addition. For 1 mm diameter suction-cast rods of the alloys; highest amorphous fraction was obtained for the highest Sm (4 at%) addition while the amorphous portion reinforced with CuZr (B2) crystals was achieved in less amount of Sm addition (1 at. % and 3 at.%). From Inoue proposal, it is assumed that the wider supercooled liquid region, ΔT_x results in the thermally more stable metallic glass and thereby larger GFA. However, many studies have reported that there is no proportional relationship exists between ΔT_x and GFA and furthermore many systems show low GFA for relatively largest ΔT_x [60–63]. This seems similar to our case. Recently, Deng *et. al.* reported that ΔT_x increases with the addition of rare-earth Y element while it decreases with the addition of as Gd and Nd rare-earths to Cu-Zr-Al alloy [58-59].

2.4.4. Compression Tests and Fracture Surface Analysis

Fig.2.15 indicates the effect of Sm addition on compressive strengths. The amorphous $(Zr_{50}Cu_{40}Al_{10})_{96}Sm_4$ has the highest compressive fracture strength (1202 MPa) while $Zr_{50}Cu_{40}Al_{10}$ (634 MPa), $(Zr_{50}Cu_{40}Al_{10})_{99}Sm_1$ (632 MPa) and $(Zr_{50}Cu_{40}Al_{10})_{97}Sm_3$ (687 MPa) have similar compressive fracture strength values. Among four alloy compositions only $Zr_{50}Cu_{40}Al_{10}$ show discrete plastic deformation, which is attributed to crystalline nature of the sample. Other partially crystalline samples $(Zr_{50}Cu_{40}Al_{10})_{99}Sm_1$ and $(Zr_{50}Cu_{40}Al_{10})_{97}Sm_3$ show no sign of plasticity with low

fracture strength, i.e., they combine poor ductility and low strength of both glass and crystalline material. $(Zr_{50}Cu_{40}Al_{10})_{96}Sm_4$ composition has a considerably high fracture strength, but no plasticity due to its higher amorphous structure portion.

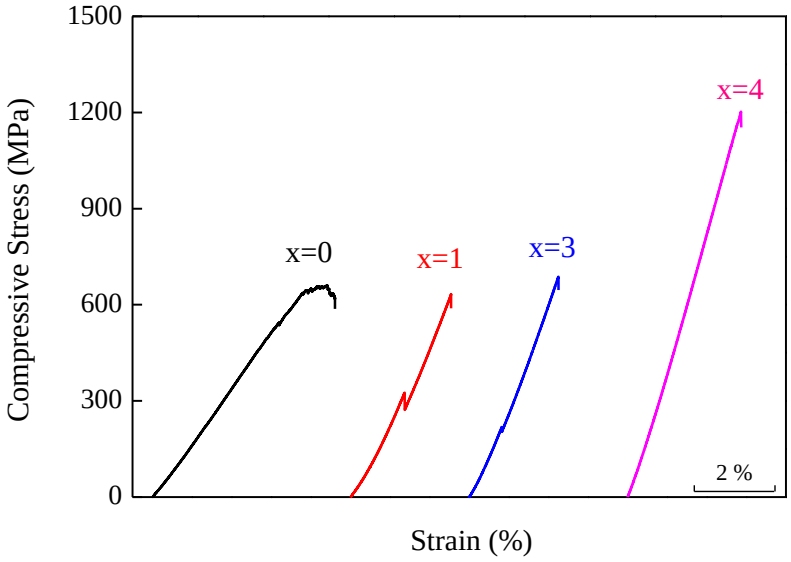

Figure 2. 15 Compressive stress-strain curves for 3 mm diameter $(Zr_{50}Cu_{40}Al_{10})_{100-x}Sm_x$ (x=0, 1, 3, 4 at. % Sm) suction cast rods.

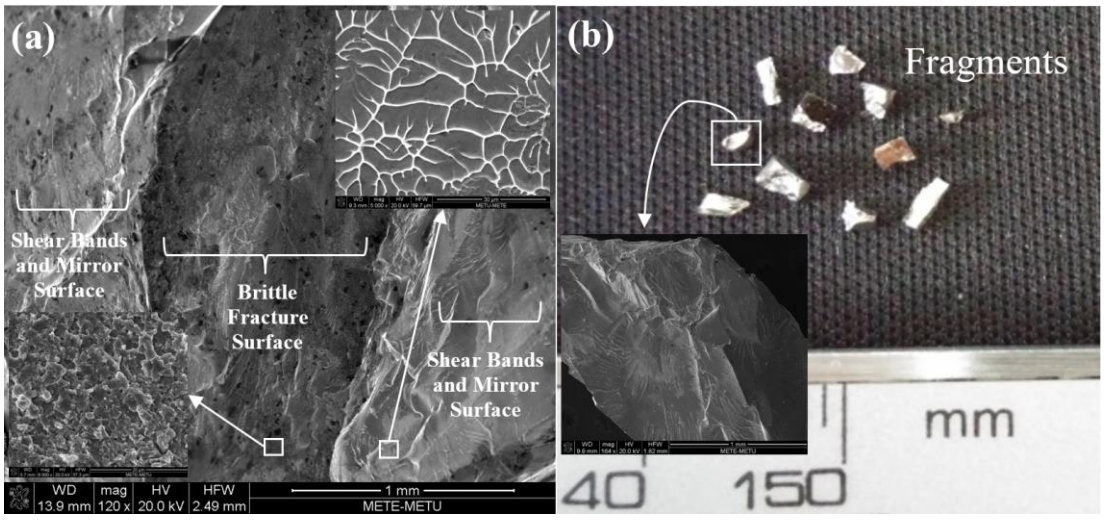

Figure 2. 16 SEM micrographs of fracture surfaces of 3 mm diameter (a) $(Zr_{50}Cu_{40}Al_{10})_{99}Sm_1$ and (b) fragments of $(Zr_{50}Cu_{40}Al_{10})_{96}Sm_4$ suction-cast rod after fracture.

Microstructural analysis was carried out to examine the amorphous nature and fracture characteristics of 3 mm diameter partially amorphous $(Zr_{50}Cu_{40}Al_{10})_{99}Sm_1$, $(Zr_{50}Cu_{40}Al_{10})_{97}Sm_3$, and $(Zr_{50}Cu_{40}Al_{10})_{96}Sm_4$ suction cast rods. It is observed that $(Zr_{50}Cu_{40}Al_{10})_{99}Sm_1$ and $(Zr_{50}Cu_{40}Al_{10})_{97}Sm_3$ compositions fail with shear mode fracture type, but $(Zr_{50}Cu_{40}Al_{10})_{96}Sm_4$ undergoes fragmentation fracture mode. SEM micrograph of the fracture surface of $(Zr_{50}Cu_{40}Al_{10})_{99}Sm_1$, which has two distinct regions; crystalline cleavage in the core part and mirror in the rim is shown in Fig.2.16 (a). The surface analysis of $(Zr_{50}Cu_{40}Al_{10})_{99}Sm_1$ illustrated the structural heterogeneity of this sample. This structural fluctuation is mainly caused by the variation of cooling rate during suction casting. While the regions closed to the mold wall reaches higher cooling rate and thereby results in the formation of amorphous structure, inner core will have lower cooling rate. Although crystalline regions are present, it is important to note that glassy rim region contains branched vein patterns. Vein pattern shear bands are observed in fracture surfaces of metallic glass samples that failed under shear fracture mode.

$(Zr_{50}Cu_{40}Al_{10})_{97}Sm_3$ and $(Zr_{50}Cu_{40}Al_{10})_{96}Sm_4$ show featureless mirror region with shear band marks which is observed in brittle fracture of metallic glasses. Fragmentation of $(Zr_{50}Cu_{40}Al_{10})_{96}Sm_4$ sample after fracture revealing the shift in fracture mode with Sm addition. Shift in fracture mode can be also observed in Fig.2.17 as it illustrates the SEM micrographs of fracture surfaces of each alloy. Fig.2.17 (a) and Fig.2.17 (b) represent distorted shear fracture mode where shearing does not occur on a single shear plane due to presence of crystalline phases. SEM images in Fig.2.17 (b) and Fig.2.17 (c) reveal featureless mirror region with shear band marks for $(Zr_{50}Cu_{40}Al_{10})_{97}Sm_3$ and $(Zr_{50}Cu_{40}Al_{10})_{96}Sm_4$, respectively. The failure mode analysis conducted on the amorphous $(Zr_{50}Cu_{40}Al_{10})_{96}Sm_4$ and Fig.2.17 (c) shows the SEM micrographs of fragment surfaces where no vein pattern or local melting is observed. Radiating marks without branches are observed in the SEM images of fragment surfaces.

The smooth and shiny surface with the shear band marks for $(Zr_{50}Cu_{40}Al_{10})_{97}Sm_3$ and $(Zr_{50}Cu_{40}Al_{10})_{96}Sm_4$ revealed the amorphous nature of these alloys. SEM analysis has

also confirmed the increase in amorphous portion and thereby the glass forming ability with increasing Sm concentration in Cu-Zr-Al alloys. When considering compression properties, for instance $(Zr_{50}Cu_{40}Al_{10})_{99}Sm_1$ has highest fracture strain with only observable plasticity due to its crystalline nature. On the other hand, amorphous $(Zr_{50}Cu_{40}Al_{10})_{96}Sm_4$ has the highest compressive fracture strength which is caused by its brittle amorphous nature.

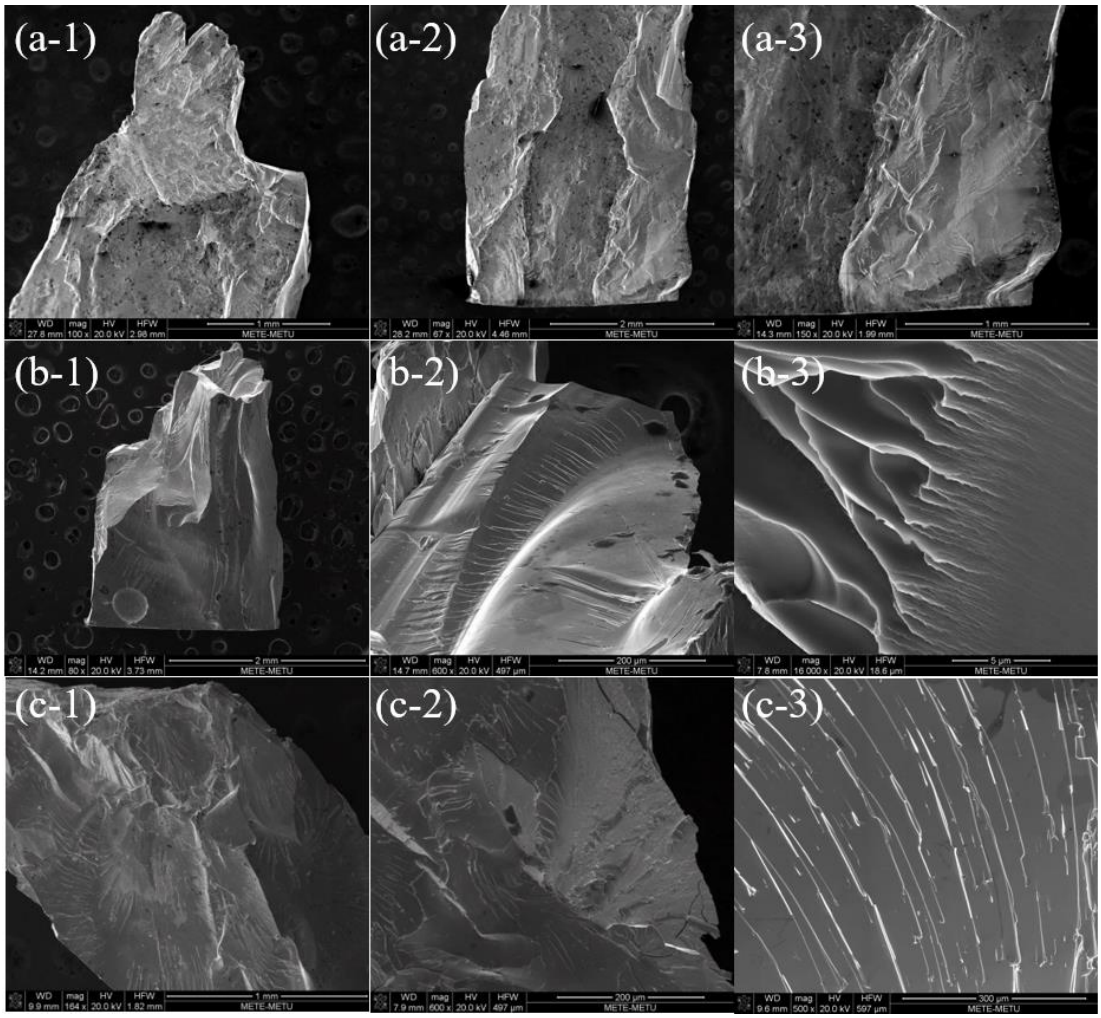

Figure 2. 17 SEM micrographs of fracture surfaces of 3 mm diameter (a) $(Zr_{50}Cu_{40}Al_{10})_{99}Sm_1$, (b) $(Zr_{50}Cu_{40}Al_{10})_{97}Sm_3$, (c) $(Zr_{50}Cu_{40}Al_{10})_{96}Sm_4$ suction-cast rod at different magnifications.

Several studies have reported that fracture surfaces of ductile metallic glasses under compression contain smooth regions and dominant vein patterns. The vein pattern, related to ductile shear failure of the metallic glasses, is formed by superplastic behavior of the liquid-like glass during local temperature increase [64–66]. Here, we did not observe any dominant vein pattern in our alloys, which is consistent with our findings since none of the glassy alloys show any remarkable plasticity during compressive loading. The fragmentation type failure mode was observed in amorphous $(Zr_{50}Cu_{40}Al_{10})_{96}Sm_4$. SEM analysis did not show any vein pattern or local melting. The fragmentation failure mode is generally observed in Mg-, Fe- and Co-based BMGs under compressive loading [67] however it has been reported that in Zr-based BMGs it was observed only under impact loading [68]. As a different from shear failure via one dominant shear band seen in Zr-based BMGs, in this study it is observed that $(Zr_{50}Cu_{40}Al_{10})_{96}Sm_4$ fail in fragmentation mode. It is clear that there is a drastic change in failure mode of the Zr-based BMGs, which is mainly because of the rare-earth element addition.

2.5. Conclusion

The effect of rare-earth (Sm) microalloying on the glass forming ability and mechanical properties of $(Zr_{50}Cu_{40}Al_{10})_{100-x}Sm_x$ (x= 0, 1, 3, 4 at. %) alloys have been investigated in combination of DSC, XRD, SEM and mechanical testing. The alloys were produced using arc-melting and suction-casting techniques. Based on XRD analysis, the glass forming ability of $Zr_{50}Cu_{40}Al_{10}$ alloy was found to increase by the addition of Sm. Furthermore, DSC analysis has revealed that increasing the Sm concentration in the alloys decreases ΔT_x, which is considered to be related to the thermal stability of the amorphous phase. However, there are many systems such as in the addition of Gd and Nd rare-earths show high GFA for relatively low ΔT_x. The mechanical properties were investigated using compressive fracture testing. The results have revealed that the fracture strength of the glassy alloy including 4 at. % Sm increased to 1.2 GPa while the crystalline alloy without Sm and partially crystalline alloys with little Sm addition failed at around 630 MPa. The ductile Zr-based BMGs generally fail with shearing mode under quasi-static loading conditions, however, in this study change of fracture mode from cleavage to fragmentation with increasing Sm concentration and thereby increasing amorphous portion was observed.

CHAPTER 3

CRYSTALLIZATION KINETICS & NANOCRYSTALLIZATION IN Cu-Zr-Al-Sm BULK METALLIC GLASSES

3.1. Introduction

Devitrification of several Zr-based metallic glasses attract much attention due to their peculiar crystallization behavior. Considering the classical nucleation theory at temperature range between crystallization temperature, T_x and glass transition temperature, T_g, nucleation rate for crystallization of an alloy with high GFA should be very limited. Thus, the expected microstructure should be relatively coarse. However, in recent studies nanocrystallization in Cu-Zr-Al metallic glasses are observed. In this chapter, nanocrystallization in $(Zr_{50}Cu_{40}Al_{10})_{96}Sm_4$ alloy composition were investigated on both suction-cast rods and melt-spun ribbons via combined study of XRD, DSC, TEM and APT.

3.2. Literature Review

3.2.1. Crystallization of Cu-Zr Metallic Glasses

Crystallization of Cu-Zr metallic glasses were first investigated on melt-spun ribbons of $Cu_{50}Zr_{50}$ composition in 1982 [69]. The study resulted that crystallization of $Cu_{50}Zr_{50}$ metallic glasses in fully amorphous state occur via one step crystallization and two eutectic products, which are mainly $Cu_{10}Zr_7$ phase along with $CuZr_2$ phase. Similar study done by Kneller also proved presence $Cu_{10}Zr_7$ and $CuZr_2$ phases as final product; however, Kneller *et. al.* showed polymorphic crystallization of cubic CuZr (B2) phase occurs prior to eutectic duo [70]. Later, CuZr phase rapidly decompose into $Cu_{10}Zr_7$ and $CuZr_2$ phases. In case of suction-casting, limited cooling rate resulted in crystallization of cubic CuZr or metastable martensitic CuZr phase in Cu-Zr metallic

glasses. For most Cu-based or Zr-based metallic glasses suppressing the crystallization of CuZr during solidification results in a fully amorphous structure [49,50,71–76].

Such phase selection is not only limited with $Cu_{50}Zr_{50}$ composition, CuZr, $Cu_{10}Zr_7$ and $CuZr_2$ phases are also observed in various compositions under isothermal and continuous heating conditions. For instance, Kalay et.al. investigated the crystallization kinetics and phase transformation mechanisms of $Cu_{56}Zr_{44}$ alloy composition and showed that nucleation of $Cu_{10}Zr_7$ and $CuZr_2$ phases start the crystallization [44]. DSC curve of $Cu_{56}Zr_{44}$ ribbons are shown in Fig.3.1 (a) illustrate the devitrification path with a discrete endothermic signal T_g followed by single step crystallization T_x. Fig.3.1 (b) shows the BF TEM image of same sample isothermally annealed at 705 K. $Cu_{10}Zr_7$ crystal with approximate size of 1 μm with heterogeneous structure; cellular through outside and planar core, can be seen. Crystallization of Cu-Zr metallic glasses occurs in a rather coarse manner where crystal sizes are in micrometers. Coarse crystallization and growth of $Cu_{10}Zr_7$ phase can be explained by the classical nucleation theory.

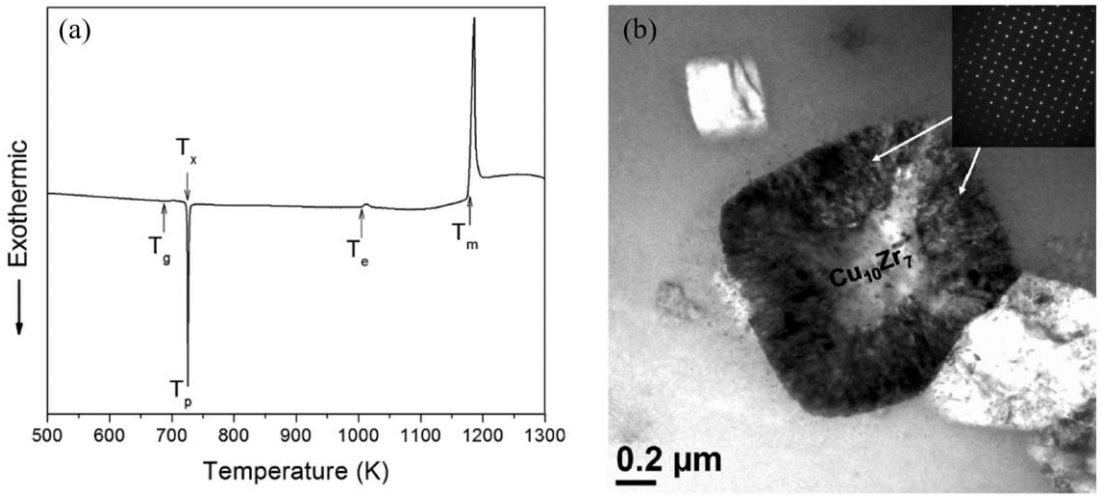

Figure 3. 1 (a) Continuous heating DSC curve of $Cu_{56}Zr_{44}$ melt-spun ribbon with 10 K/min heating rate and (b) BF image of isothermally annealed $Cu_{56}Zr_{44}$ melt-spun ribbon at 705 K. Adopted from [44].

3.2.2. Nanocrystallization in Cu-Zr-TM Metallic Glasses

Effect of Zn on glass forming ability and crystallization kinetics of $Cu_{50}Zr_{50}$ metallic glasses were investigated by Wu et.al. Study showed that Zn addition not only increased GFA but also stabilized the crystallization of CuZr phase at lower temperatures. However, Zn addition up to 14 at. % had no effect on primary crystallization of $Cu_{10}Zr_7$ and $CuZr_2$ phases during annealing. Optical microscope images of $(Cu_{50}Zr_{50})_{100-x}Zn_x$ (x=0, 4.5, 7.5 and 14 at. %) 2 mm diameter suction cast rods are shown in Fig.3.2. It is clear that with increasing Zn content, growth of metastable martensitic CuZr phase is hindered and cubic CuZr (B2) phase is favored. Further Zn addition up to 14 at. % stabilize amorphous phase, revealing enhanced GFA for the system [73].

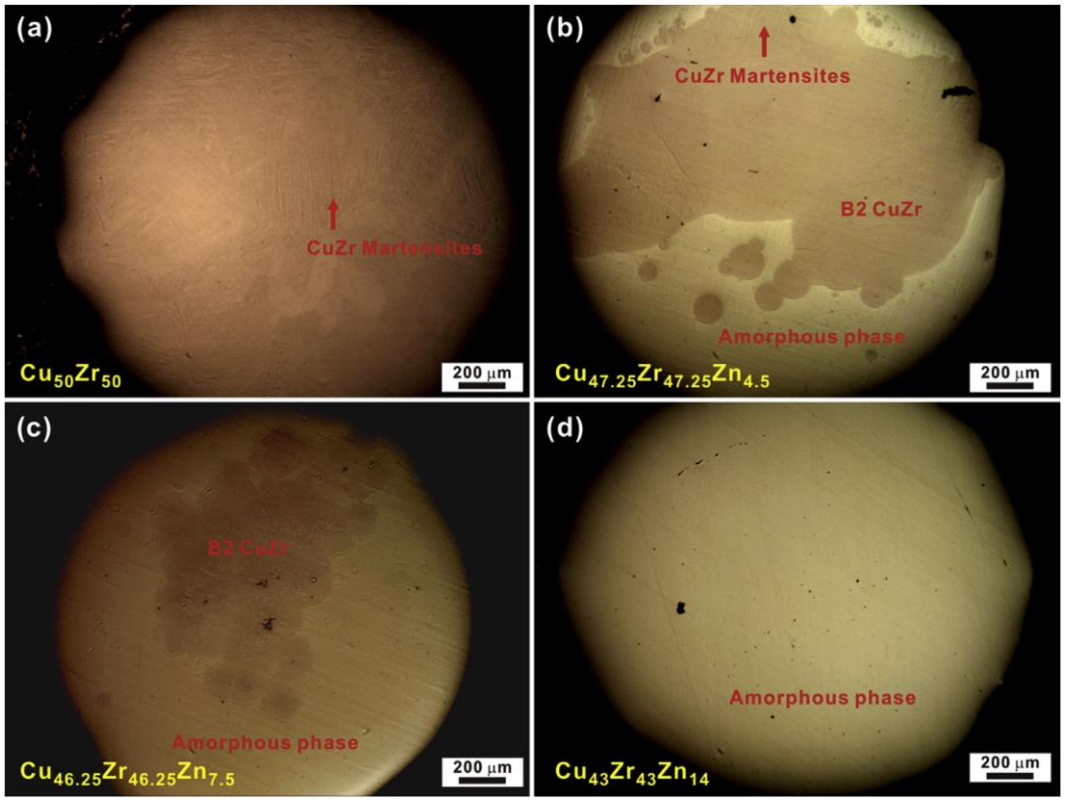

Figure 3. 2 Optical microscopy images of the suction-cast $(Cu_{50}Zr_{50})_{100-x}Zn_x$ (x = 0, 4.5, 7.5, and 14 at. %) rods with a diameter of 2 mm. Adopted from [73].

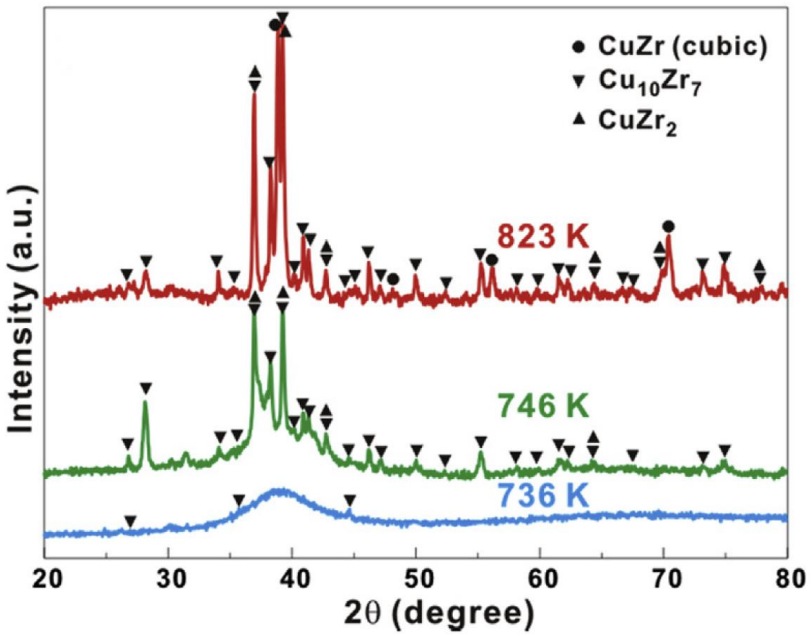

Figure 3. 3 XRD patterns of suction cast $Cu_{43}Zr_{43}Zn_{14}$ rods with 2 mm diameter isothermally annealed at different temperatures as indicated. Adopted from [73].

Fig.3.3 shows XRD patterns of isothermally annealed $Cu_{43}Zr_{43}Zn_{14}$ samples, indicating annealing induced crystallization starts with $Cu_{10}Zr_7$ and $CuZr_2$, followed by CuZr crystallization at higher temperatures. Effect of Al is found to be similar to Zn, in terms of enhancing GFA and stabilizing cubic CuZr phase. Wei et.al. stated that crystallization sequence for $Cu_{48}Zr_{48}Al_4$ composition starts with CuZr phase and followed by $Cu_{10}Zr_7$ and $CuZr_2$ phases as shown in Fig.3.4 [71]. Another important consequence of Al micro-alloying is that low temperature crystallization of B2 CuZr occurs in nanometer scale unlike micrometer scale crystallization of $Cu_{10}Zr_7$ and $CuZr_2$ in Al-free Cu-Zr bulk metallic glasses.

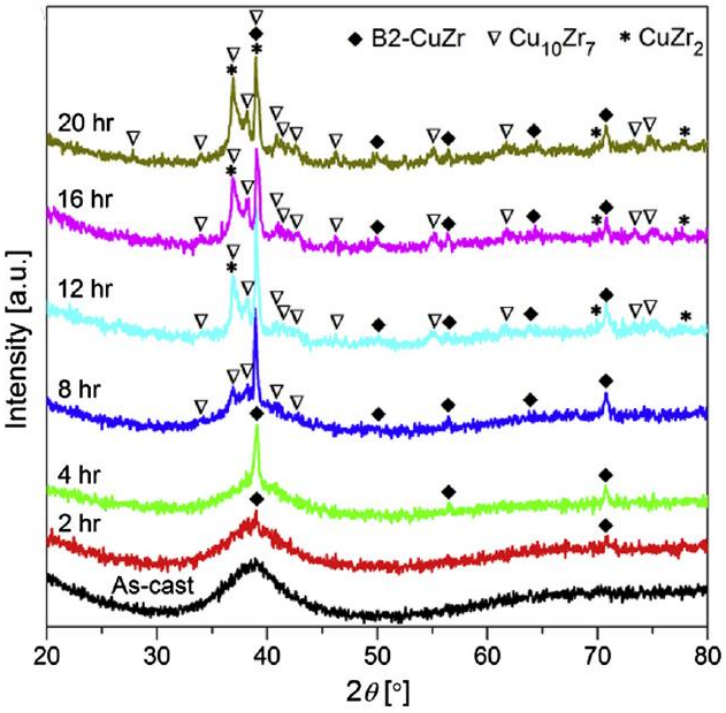

Figure 3. 4 XRD patterns of $Cu_{48}Zr_{48}Al_4$ rods annealed at different times as indicated. Adopted from [71].

In a similar study, Louzguine-Luzgin et.al. showed nanocrystallization in $Zr_{55}Cu_{35}Al_{10}$ with an extremely high nanocrystal density (> 10^{23} m^{-3}) [77]. In recent studies, minor Al addition into Zr-Cu metallic glasses found to trigger high density nanocrystallization. Fig.3.5 shows spherical 15 nm diameter size CuZr (B2) nanocrystals embedded in amorphous matrix for various times. Fig.3.5 (a) shows earlier stages of nanocrystallization and Fig.3.5 (b) shows lateral stage where nanocrystal density is very high.

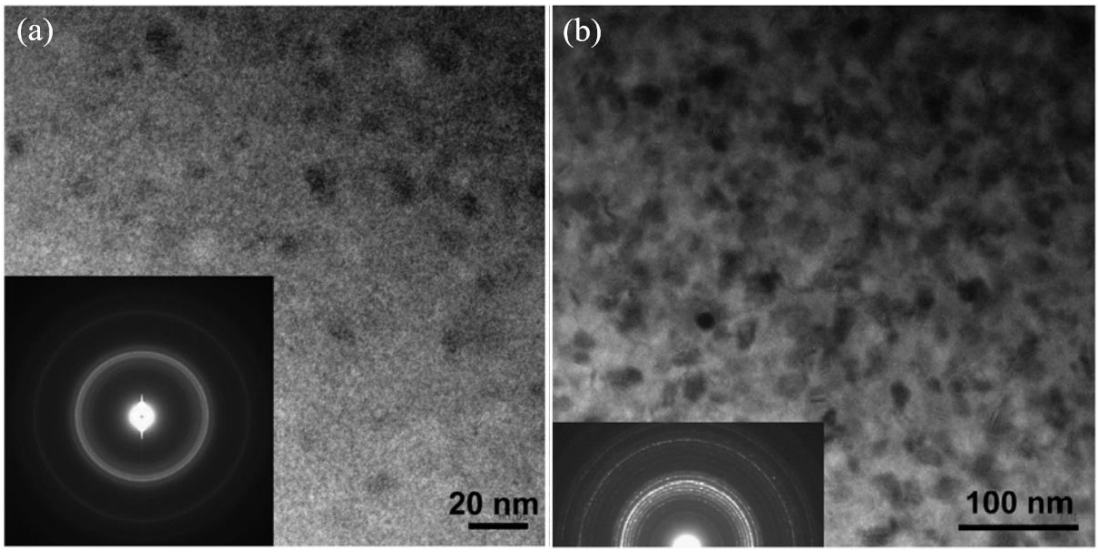

Figure 3. 5 TEM images of $Cu_{55}Zr_{35}Al_{10}$ melt-spun ribbons annealed for (a) 1.25 kS and (b) 3 kS. Inset depicts SAED patterns for each image. Adopted from [77].

In Zr-based metallic glasses, phase separation is considered as the source of nanocrystallization [78–81]. It is stated that nanocrystallization occurs from regions where melt is separated spinodally. Nanoscale chemical heterogeneities induced by phase separation results in easier nucleation sites and cause nanocrystallization in the metallic glass. Due to appearance of such models phase separation phenomenon in metallic glasses attract much attention in order to understand crystallization sequences.

3.2.3. Phase Separation in Cu-Zr-Al-RE Metallic Glasses

Introduction of RE elements not only affect the devitrification paths, but also the as-cast structure for Cu-Zr-Al metallic glasses. Various studies showed that addition of rare-earth elements tend to trigger phase separation of Zr-rich and RE-rich glassy phase in Cu-Zr-Al metallic glasses [7,59,82–84]. Phase separation can occur in metallic glasses, since they are thermodynamically unstable. Such phase separation can either occur in liquid state and can be obtained during cooling or in solid state, where metallic glasses is annealed. Whether it is former or latter type strongly depends on alloy systems, in fact, heat of mixing of constituent elements of the system [82]. Considering most metallic glass system with high GFA having atom pairs with

negative heat of mixing, phase separation during heating is rather unexpected. Although there are studies indicating phase separation in couple metallic glass systems, results are not considered as unambiguously true since it is hard to distinguish phase separation from nucleation and growth of nanocrystals at early stages even with powerful techniques such as TEM. In addition, compositional fluctuations can be too small to detect when the driving force for separation is small. However, when atom pairs with positive heat of mixing are intentionally introduced into a metallic glass system, phase separation of two glassy phase can be achieved. Considering most RE elements such as Sm, Tb, Gd, Y or Lu having a positive enthalpy of mixing with Zr, addition of RE elements tend to favor immiscibility and moves the alloy composition to phase separated state [56–58,80,83,85–87]. Park et.al. showed that Y addition up to 35 at. % as a substitute of Zr into $Cu_{46}Zr_{47}Al_7$ composition resulted in phase separation of CuZr-rich and CuY-rich amorphous phases, also addition of Gd into $Cu_{46}Zr_{47}Al_7$ and $Cu_{50}Hf_{42.5}Al_{7.5}$ compositions showed that Gd also triggers formation of Gd-rich and Zr/Hf-rich glassy phase [58,59]. Fig.3.6 (a) shows DSC curves for $Cu_{46}Zr_{47-x}Al_7Gd_x$ (x=0, 5, 10, 15, 20, 25, 30, 35, 40, 47 at. %) melt-spun ribbons revealing two unique glass transition and crystallization duos; one representing Gd-rich and other representing Zr-rich crystallizing glass. In Fig.3.6 (b), brigth-field TEM image of $Cu_{46}Zr_{22}Al_7Gd_{25}$ composition along with SAED pattern illustrates two distinct amorphous phases within alloy.

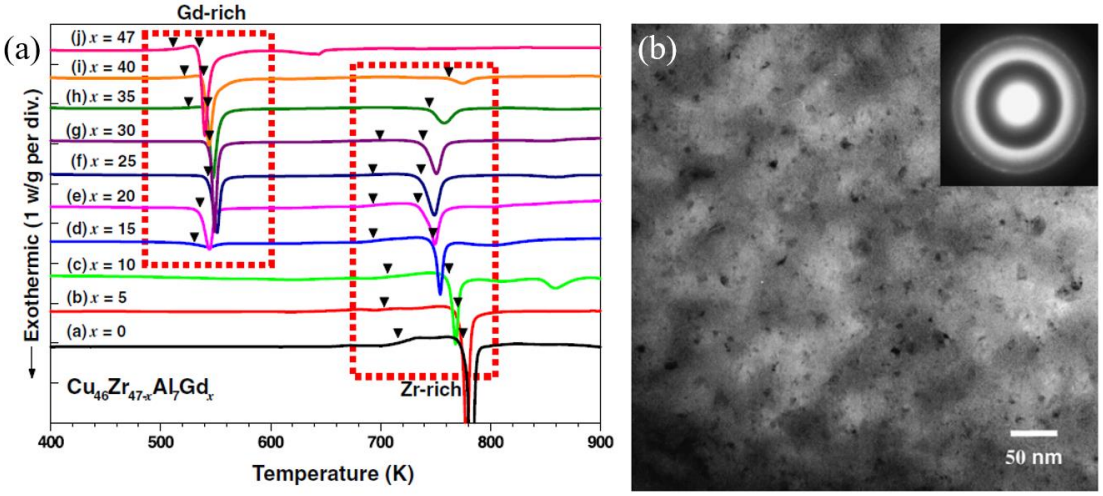

Figure 3. 6 (a) DSC traces of $Cu_{46}Zr_{47-x}Al_7Gd_x$ (x=0, 5, 10, 15, 20, 25, 30, 35, 40, 47 at. %) melt-spun ribbons and (b) TEM BF image of 25 at. % Gd containing melt-spun sample. Inset depicts broad halo in SAED pattern. Adopted from [58].

In a similar study, Han et.al. also showed the effect of 10 at. % Gd addition into $Zr_{56}Co_{28}Al_{16}$ composition resulted in phase separation as shown in Fig.3.7. According to their TEM analysis in Fig.3.7 (a-c) samples with lower Gd concentrations such as 5 at. % showed no discrete sign of phase separation, while phase separation becomes more evident with further alloying up to 20 at. % Gd in as-cast state; however, APT analysis showed finer nanoscale phase separation even for $Zr_{51}Co_{28}Al_{16}Gd_5$ composition as shown in Fig.3.7 (d) [83]. Studies concerned about addition of RE to Zr-based metallic glasses showed that amount of RE before phase separation is initiated within amorphous phase is approximately same for Y and Gd. For instance, according to DSC analysis critical minimum phase separation composition for Y and Gd is about 15 at. %. More powerful characterization techniques such as TEM and APT showed that this critical minimum phase separation composition is much lower and depends slightly on rare-earth element i.e. as low as 5 at. % for Gd and approximately about 10 at. % for Y [58].

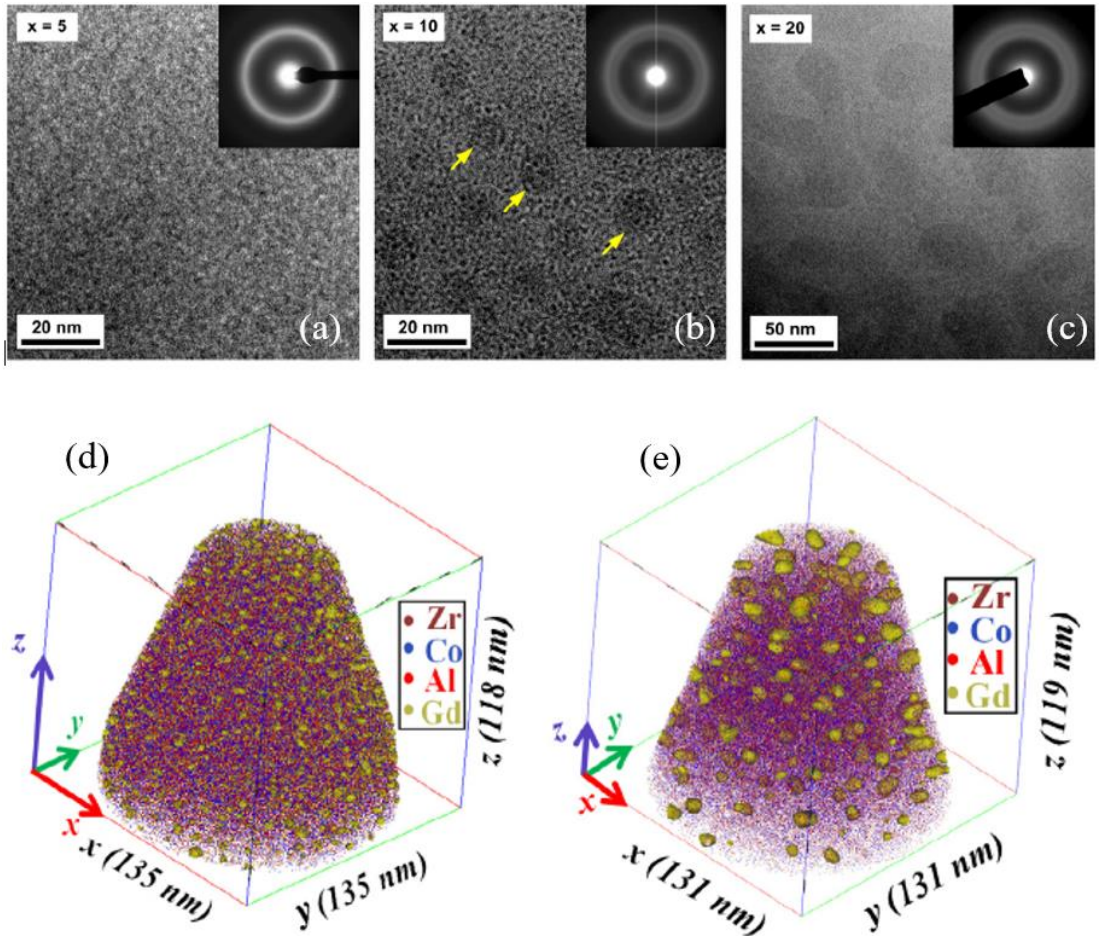

Figure 3. 7 TEM BF images of $Zr_{56-x}Gd_xCo_{28}A_{16}$ melt-spun ribbons for (a) x=5, (b) x=10, (c) x=20 and APT atomic spatial distrubutions of (d) x=5 and (e) x=10. Adopted from [83].

3.3. Experimental Procedure

3.3.1. Production of Alloys

Suction cast 1, 2, and 3 mm diameter rods of $(Zr_{50}Cu_{40}Al_{10})_{100-x}Sm_x$ (x=0, 2, 4 at. %) alloy composition samples are prepared by the same procedure and methods that are explained in Chapter 2. However, the arc-melter that is used in this particular chapter is a different machine (Edmund Bühler MAM-1, which is a more recent model) in Metallurgical and Materials Engineering Department of Middle East Technical University. In parallel, same alloy composition samples were prepared in 40 μm thick melt-spun ribbon form in Ames Laboratory, Iowa, US in courtesy of Prof. Matthew J. Kramer. These samples are then shipped to Turkey in order to conduct devitrification and characterization experiments.

3.3.2. X-ray Diffraction and Differential Scanning Calorimetry Analysis

Details of XRD and DSC samples and experiments can be found in Chapter 2 as well. Continuous heating experiments that are conducted in this chapter are done at a heating rate of 0.5 K/s (30 ^{o}C/min). Isothermal controlled crystallization (annealing) experiments are also conducted within DSC at a heating rate of 0.5 K/s (30 ^{o}C/min) in order to monitor and interrupt crystallization. Isothermal annealing is done at 703 K (which is in supercooled liquid region) under N_2 atmosphere for various times corresponding to the onset, the maxima and the end of isothermal crystallization peak. Samples are interrupt quenched with a cooling rate of 1 K/s (60 ^{o}C/min) inside DSC in order to maintain structure. Annealing times were adjusted due to the shift in crystallization peak position for rod and ribbon samples. The shift in isothermal crystallization peak position to higher annealing times were discussed in discussion part.

Activation Energy Calculations by Kissinger-Akahira-Sunose (KAS) and Flynn-Wall-Ozawa (FWO) Methods

Activation energies for $(Zr_{50}Cu_{40}Al_{10})_{100-x}Sm_x$ (x=0, 2, 4 at. %) composition ribbon samples are calculated using KAS and FWO methods in order to discuss the effect of Sm on crystallization kinetics. To perform activation energy calculations from the data provided from continuous heating experiment, multiple experiments with various heating rates must be conducted. In this particular chapter, 4 different heating rates, namely 0.17-0.33-0.5-0.66 K/s (10-20-30-40 ^{o}C/min) are applied for activation energy calculations. For each continuous heating curve characteristic crystallization peak temperatures are acquired. Thermal data obtained are used in KAS and FWO equations shown in Equation 3.1 and Equation 3.2 respectively.

$$\ln\left(\phi/T_p^2\right) = -\left(\frac{E_c}{RT}\right) + constant \qquad \text{Equation 3.1}$$

$$\ln(\phi) = -1.052\left(\frac{E_c}{RT}\right) + constant \qquad \text{Equation 3.2}$$

Where, ϕ represents heating rate, T_p represents crystallization peak temperature at maxima, E_c represents activation energy for crystallization, R represents gas constant and T represents temperature. Considering the above equations slopes of $\ln\left(\phi/T_p^2\right)$ vs. $1000/T_p$ curve for KAS and $\ln(\phi)$ vs. $1000/T_p$ curve for FWO should give activation energy, E_c.

3.3.3. Transmission Electron Microscopy Analysis

The TEM characterizations were performed using a JEOL JEM2100F field-emission gun scanning/transmission electron microscope operating at 200 keV voltage. All specimens for TEM were prepared through Focus Ion Beam (FIB) microscope in Sabancı University, TR in courtesy of Dr. Meltem Sezen. TEM that is used in this study is shown in Fig.3.8 (a).

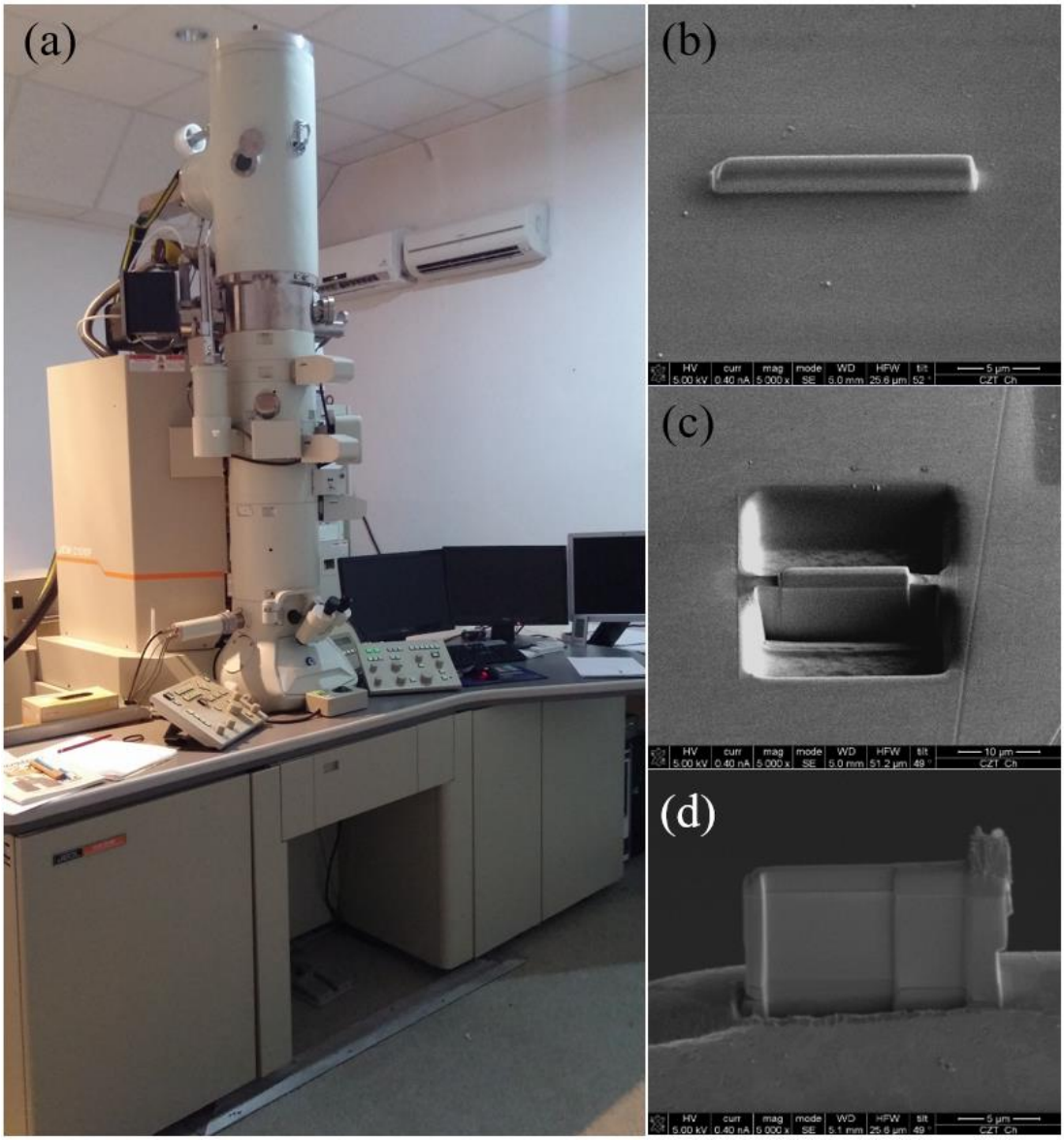

Figure 3. 8 (a) JEOL JEM2100F field-emission gun scanning/transmission electron microscope used in this thesis and important steps of FIB sample preparation steps as (b) Pt deposition, (c) Ga-milling, (d) sample removal.

Focused Ion Beam (FIB) Milling

TEM samples could not prepared by conventional TEM sample preparation methods i.e. electro-polishing or ion milling, due to uneven and thin shape of samples. All TEM samples were prepared in FIB. In order to do so, firstly, region of interest for specimens were coated with Pt as shown in Fig.3.8 (b). The main purpose of Pt deposition on sample surface is to protect the sample area from Ga ion damage during milling. During Pt deposition, electron image is tilted so that deposition can be observed clearly; however, ion deposition is done perpendicular to the surface. After required thickness of Pt coating is achieved, Ga ion milling is initiated as illustrated in Fig.3.8 (c). Ga ions are bombarded on selected areas near the specimen region and thus sample vicinity is mechanically etched. When upper and lower sides of the sample is completely etched, milling is applied to right and left sides. Before milling bottom part, sample is fixated or welded to omniprobe tool by depositing Pt between sample-omniprobe interface so that sample would not simply fell off. Finally, sample is removed by Ga ion milling to bottom and replaced to TEM sample holders as shown in Fig.3.8 (d).

One important drawback of FIB milling is that Ga ion damage can spoil the sample. In some cases, milling can introduce high amount of Ga into the system, changing the composition and structure of the alloy. In particular study, mechanical deformation induced crystallization is the main concern. By operating FIB with lower voltages and beam currents such problems can be minimized. During analyzing results Ga ion milling damage or any structural change caused by Ga ions are considered carefully. FIB milling was found to do little effect according to TEM and APT results shown in results and discussion part of this chapter.

3.3.4. Atom Probe Tomography Analysis

Atom probe tomography (APT) samples are prepared in FIB in Sabancı University. APT sample preparation via FIB is only little different from TEM sample preparation via FIB. Additionally, after fine samples are removed from large sample surface sample is sharpened by further Ga ion milling in order to obtain a sharp tip shaped APT sample. APT experiments are conducted at temperature of 50 K with pulse rate of 200 kHz, 20% pulse fraction and 0.5% detection rate with IMAGO Local Electrode Atom Probe (LEAP) instrument in Idaho National Laboratory, Center of Advanced Energy Studies in Idaho, US in courtesy of Dr. Yaqiao Wu. APT experiments have been only conducted on annealed rod samples due to time limitations. Sadly, no ribbon samples were investigated via APT analysis. Nevertheless, extremely powerful resolution and chemical contrast of APT characterization proved useful and revealed some crucial results. Fig.3.9 illustrates the photograph of Local Electrode Atom Probe instrument that is used in this thesis along with APT samples prepared by in FIB.

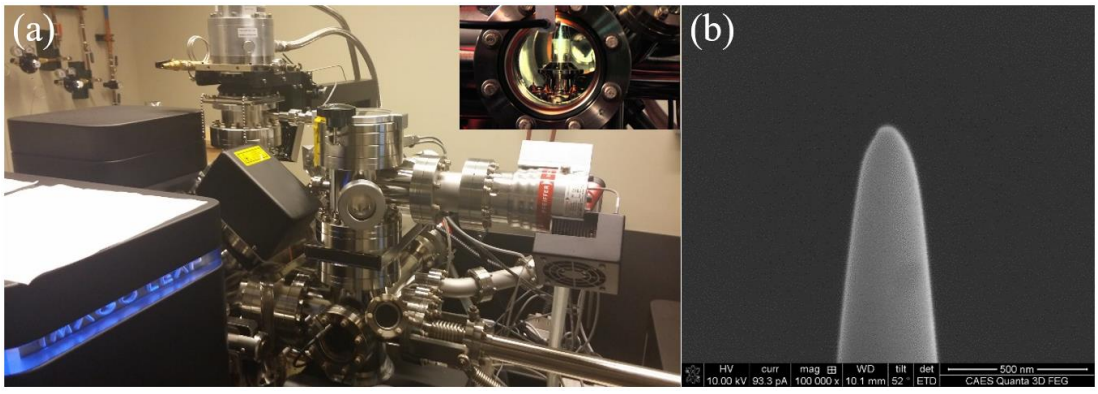

Figure 3. 9 (a) IMAGO Local Electrode Atom Probe (LEAP) instrument used in this thesis, inset depicts inner view of sample chamber and (b) nanometer scale sharp APT sample tip.

3.4. Results and Discussion

3.4.1. Preliminary Results

XRD pattern given in Fig.3.10 illustrates structure of the melt-spun ribbons and suction cast rods for $(Zr_{50}Cu_{40}Al_{10})_{100-x}Sm_x$ (x=0, 2, 4 at. %) alloy compositions. In Fig.3.10 (a), only diffuse scattering peak that is related with amorphous structure is observed in XRD patterns for all compositions. In Fig.3.10 (b), low intensity crystalline peaks are seen along with amorphous hump in XRD patterns revealing that crystal phases are embedded within amorphous phase. According to XRD patterns in Fig.3.10 (b) for $Zr_{50}Cu_{40}Al_{10}$ and $(Zr_{50}Cu_{40}Al_{10})_{98}Sm_2$ compositions crystalline solidification products of 1 mm suction cast rods are shown as CuZr phase; however, for $(Zr_{50}Cu_{40}Al_{10})_{96}Sm_4$ composition solidification product is found as Cu_2Sm phase. Considering XRD results shown in Fig.3.10 (b) amorphous hump becomes more diffuse and intensity of crystalline peaks diminish with further Sm addition revealing increased GFA once more.

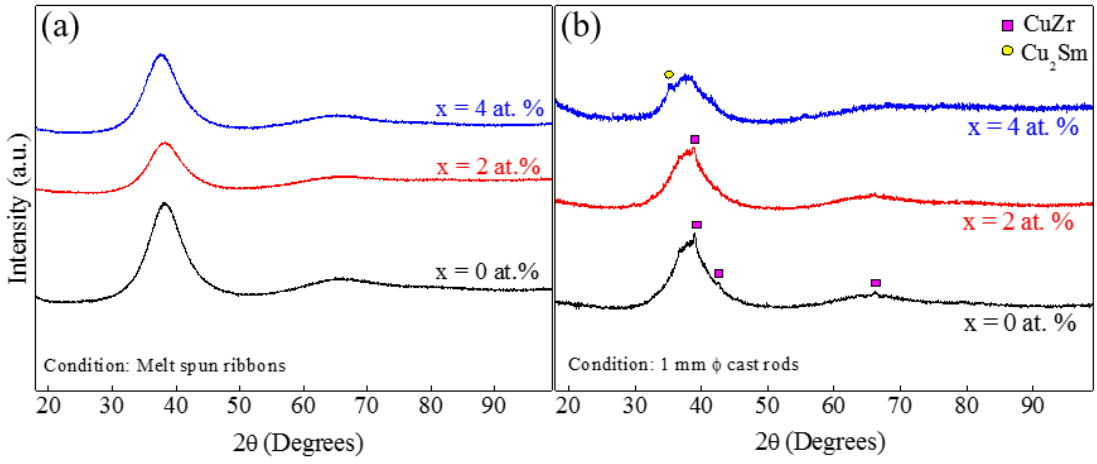

Figure 3. 10 XRD patterns of (a) melt-spun ribbons and (b) 1 mm diameter suction-cast rods of $(Zr_{50}Cu_{40}Al_{10})_{100-x}Sm_x$ (x=0, 2, 4 at. %) alloys.

DSC curves given in Fig.3.11 reveals a discrete endothermic glass transition signal followed by one step exothermic crystallization signal. DSC curves appear mostly identical for melt-spun ribbons and 1 mm diameter suction-cast rods. Characteristic thermal parameters such as T_g, T_x and ΔT are tabulated in Table 3.1 with respect to at. % Sm and sample condition. Thermal results of melt-spun ribbons in the current chapter are in good agreement with thermal data presented in Chapter 2. For both melt-spun ribbon and 1 mm diameter rod samples with increasing Sm content both T_g and T_x shift to lower temperatures. In case of ribbon samples, supercooled liquid region ($\Delta T=T_x-T_g$) decreases from 79 to 63 with 4 at. % increase in Sm within the alloy composition indicating decrease in thermal stability of the amorphous phase. For 1 mm diameter suction cast rod samples, trend is parallel except for $Zr_{50}Cu_{40}Al_{10}$ composition. Absurdly low ΔT value (50 K) of this sample is thought to be due to higher crystalline content within the sample and does not represent a true value. Considering both melt-spun ribbons and rod samples characteristic temperatures such as T_g and T_x depends on both crystalline content and Sm concentration and since any crystallization also causes fluctuations in composition, change in thermal parameters becomes rather impossible to comment on. Under such circumstances thermal results obtained from fully amorphous melt-spun ribbons for all compositions can be considered as most purposeful data.

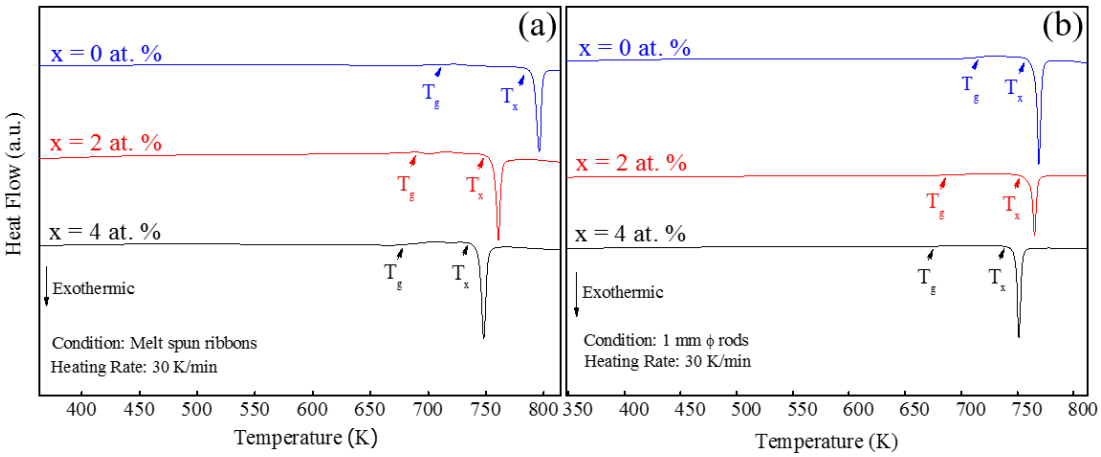

Figure 3. 11 DSC curves of (a) melt-spun ribbons and (b) 1 mm diameter suction-cast rods of $(Zr_{50}Cu_{40}Al_{10})_{100-x}Sm_x$ (x=0, 2, 4 at. %) alloys.

Table 3. 1 Thermal data obtained at 30 K/min from continuous heating DSC curves for $(Zr_{50}Cu_{40}Al_{10})_{100-x}Sm_x$ (x=0, 2, 4 at. %) composition samples.

Sample Condition	*At. % Sm*	T_g *(K)*	T_x *(K)*	ΔT
Melt-spun Ribbon	0	713	792	79
	2	683	756	73
	4	679	742	63
1 mm Ø cast rod	0	716	766	50
	2	688	761	73
	4	678	747	69

3.4.2. Crystallization Kinetics and Activation Energy Calculations

Crystallization kinetics and activation energy for crystallization is investigated on melt-spun ribbon samples of $(Zr_{50}Cu_{40}Al_{10})_{100-x}Sm_x$ (x=0, 2, 4 at. %) alloys. Although calculations and activation energy plots of only $Zr_{50}Cu_{40}Al_{10}$ composition is shown, same procedure is applied for $(Zr_{50}Cu_{40}Al_{10})_{98}Sm_2$ and $(Zr_{50}Cu_{40}Al_{10})_{96}Sm_4$ compositions as well.

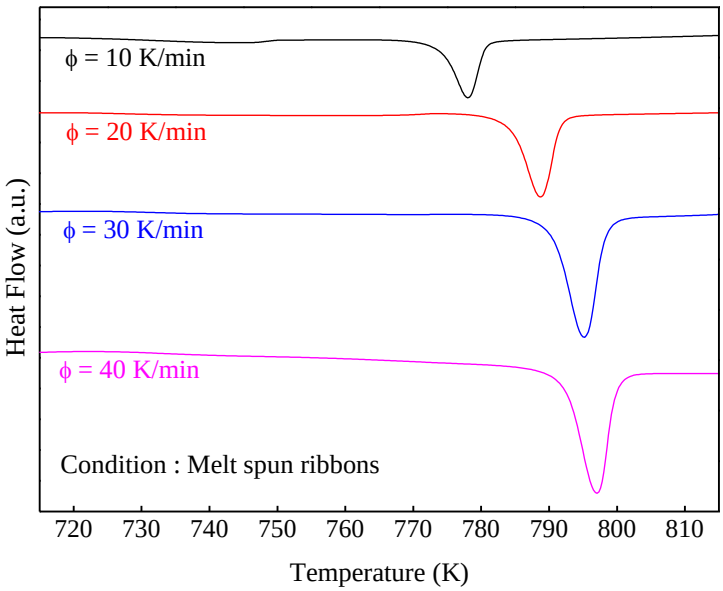

Figure 3. 12 DSC curves of melt-spun ribbons of $(Zr_{50}Cu_{40}Al_{10})$ alloy at various heating rates as indicated.

Continuous heating DSC curves of $Zr_{50}Cu_{40}Al_{10}$ composition melt-spun ribbon samples at different heating rates (10-20-30-40 K/min) are shown in Fig.3.12 illustrating the kinetic shift of crystallization peak to higher temperatures with increasing heating rate. According to the 4 unique peak temperatures in Fig.3.12, Kissinger-Akahira-Sunose method and Flynn-Wall-Ozawa method plots are obtained with 4 data points and shown in Fig.3.13 (a) and (b) respectively. Linearity of KAS and FWO plots are illustrated by r^2 values on the graphs and found as 0.978 and 0.979 respectively. Calculations are made using equation 3.1 and 3.2 using observed slope for each plot. Slope values are also shown on each graph. Calculated activation energies for each composition is shown in Table 3.2.

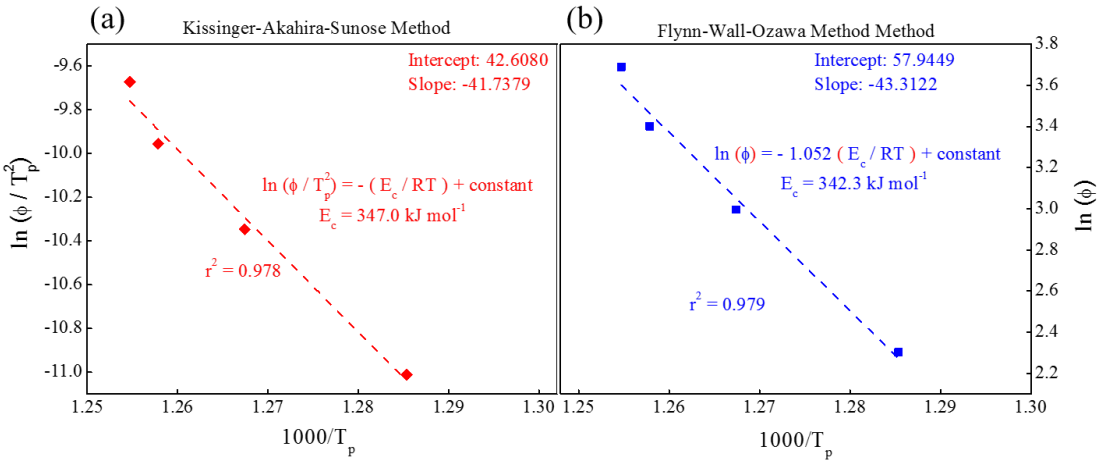

Figure 3. 13 Activation energy plots for (a) KAS and (b) FWO methods for ($Zr_{50}Cu_{40}Al_{10}$) alloy.

Fig.3.14 illustrates the change in crystallization activation energy with respect to Sm content. Both Fig.3.14 and Table 3.2 reveals that calculated activation energy of crystallization increases with Sm addition. Considering XRD results in Fig.3.17 (a), exothermic crystallization signal belongs to crystallization of $Cu_{10}Zr_7$ phase. It is important to notice large negative enthalpy of mixing between Cu and Sm (-22 kJ/mole) along with positive enthalpy of mixing between Zr and Sm (+9 kJ/mole) to make further comments. It was discussed that increase in fraction of Sm atoms within

the structure shifts solidification crystallization from CuZr phase to Cu_2Sm. It is evident that Sm atoms retard the formation of Cu-Zr pairs by repulsing Zr due to positive enthalpy of mixing. Since the crystallization of $Cu_{10}Zr_7$ phase requires diffusion of Cu-Zr pairs similar to CuZr phase, increased activation energy can be explained by increased Sm content and its effect on phase selection. This explanation can gain more validity with following APT and TEM results.

Table 3. 2 Calculated crystallization activation energies for KAS and FWO methods.

Composition	*E_c (KAS) (kJ/mole)*	*E_c (FWO) (kJ/mole)*
$(Zr_{50}Cu_{40}Al_{10})$	347.0	342.3
$(Zr_{50}Cu_{40}Al_{10})_{98}Sm_2$	395.7	388.0
$(Zr_{50}Cu_{40}Al_{10})_{96}Sm_4$	389.7	382.1

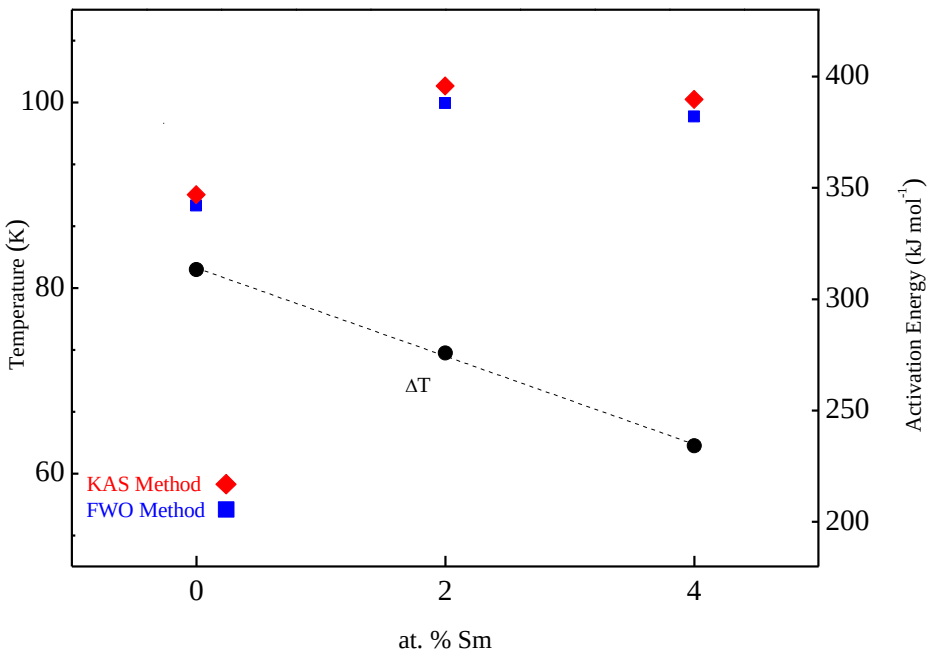

Figure 3. 14 Change in activation energy and supercooled liquid region with respect to at. % Sm composition.

3.4.3. XRD and DSC Results

The XRD patterns of melt-spun ribbons and 1, 2, and 3 mm diameter suction cast rods of $(Zr_{50}Cu_{40}Al_{10})_{96}Sm_4$ alloy composition given in Fig.3.15 reveal the as-cast structure for all samples. XRD pattern for melt-spun sample in Fig.3.15 represents only the diffuse scattering peak related to the amorphous structure, while patterns for all suction cast rods exhibit crystalline peaks for $(Zr_{50}Cu_{40}Al_{10})_{96}Sm_4$ alloy. The crystalline phase was labeled as Cu_2Sm (Imma). The XRD patterns for 1, 2, and 3 mm rods in Fig.3.15 show the partially crystalline structure where Cu_2Sm crystals were produced during solidification of alloys and embedded in the amorphous matrix. The XRD pattern of 3 mm diameter rod sample indicates the solidification products are in higher fraction for this sample since Cu_2Sm phase peaks are more discrete compared to 1 and 2 mm diameter rods which can be attributed to having lower cooling rate as sample size increases. Although Cu_2Sm crystalline peaks are present for all rod samples, Cu_2Sm crystallite size is thought to be relatively low and in small amount due to high broadening and low intensity of the crystalline peaks.

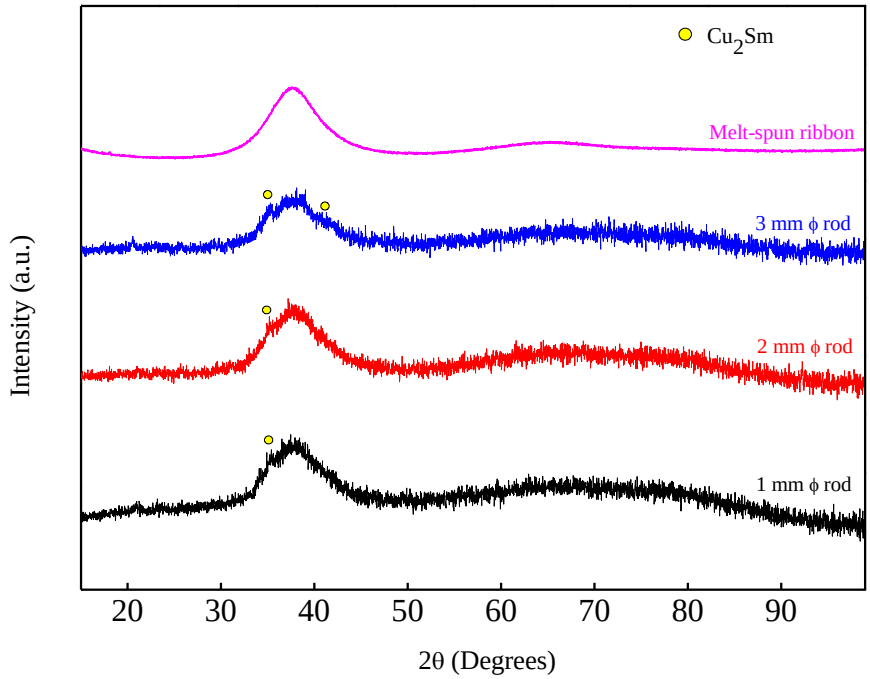

Figure 3. 15 XRD patterns of melt-spun ribbons and 1, 2 and 3 mm diameter suction-cast $(Zr_{50}Cu_{40}Al_{10})_{96}Sm_4$ alloys.

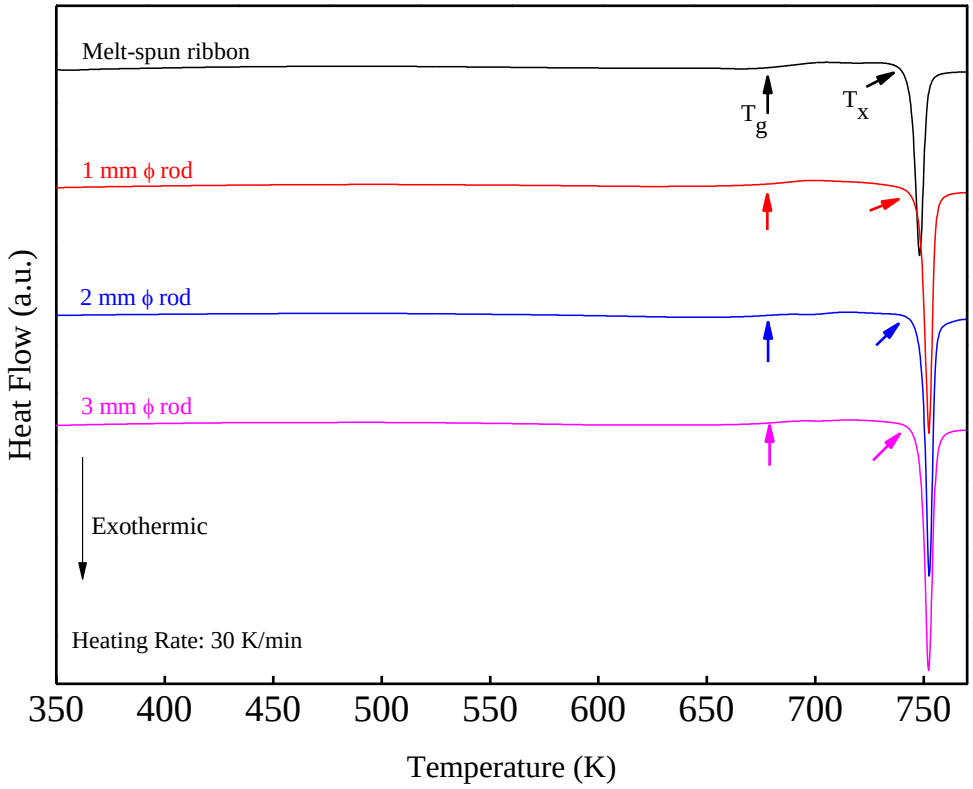

Figure 3. 16 DSC heating curves of melt-spun ribbons, 1, 2 and 3 mm suction-cast rods of $(Zr_{50}Cu_{40}Al_{10})_{96}Sm_4$ alloy. The characteristic temperatures of T_g and T_x are labeled on each trace.

The amorphous nature of the samples for melt-spun and suction cast rods was further checked by DSC analysis, given in Fig.3.16, which shows the continuous heating DSC data obtained at a heating rate of 30 K/min. Each DSC trace given in Fig.3.16 indicates a distinct glass transition feature followed by an exothermic peak associated with the crystallization. From these DSC traces, thermal data including the parameters to define GFA of the alloys, such as the glass transition temperature (T_g), the onset temperature of crystallization (T_x), the crystallization peak temperature (T_p), and supercooled liquid region (ΔT) were obtained at a heating rate of 30 K/min and listed in Table 3.3. It is observed that for all suction cast rod samples the T_g is at 677 K, while the T_x and Tp are at 747 K and 752 K respectively. Supercooled liquid region range, ΔT is found as 70 K. However, for melt-spun ribbon samples T_g, T_x and Tp are 679 K, 742 K, and 748 K respectively. Supercooled liquid region range, ΔT is shorter in case of melt spun

ribbons and found as 63 K. Differences in thermal parameters between suction cast rods and melt-spun ribbons are thought to be originated from structural and compositional differences between amorphous phases. Suction cast rods exhibit Cu_2Sm nanocrystals that are crystallized during solidification. Nucleation and growth of these Cu_2Sm nanocrystals must cause a decrease in concentration of Cu and Sm atoms, which may change composition of the metallic glass. Considering the effect of Sm on crystallization temperature as shown in preliminary results of this chapter. Decrease of Sm concentration within amorphous phase due to crystallization of Cu_2Sm may result with increase in crystallization temperature, thus effecting the ΔT. Decrease in driving force for crystallization may be another reason of higher crystallization temperature for suction cast rod samples. As system contains higher fraction of stable crystalline phases instead of unstable amorphous phase, driving force for crystallization should decrease. Decrease in driving force for crystallization can be compensated by increase in ΔT by the alloy system during heating. Same reasons can be used to explain the shift in isothermal heating DSC curves as well.

Table 3. 3 Thermal data obtained from continuous heating DSC curves for $(Zr_{50}Cu_{40}Al_{10})_{96}Sm_4$.

Sample	T_g *(K)*	T_x *(K)*	T_p *(K)*	ΔT
Ribbon	679	742	748	63
1 mm rod	678	747	752	69
2 mm rod	677	747	752	70
3 mm rod	677	747	752	70

In order to understand the devitrification path of the $(Zr_{50}Cu_{40}Al_{10})_{96}Sm_4$ alloy melt-spun ribbon samples are annealed up to elevated temperatures and then rapidly quenched to capture structure at that temperature. These samples are then investigated with XRD. Continuous annealing temperatures can be seen on the DSC curve in

Fig.3.17 (b). Quenching temperatures are indicated with arrows. These temperatures are 350 ºC (623 K), 400 ºC (673 K), 450 ºC (723 K), and 500 ºC (773 K). Corresponding XRD patterns of continuously annealed and then quenched samples can be seen in Fig.3.17 (a). XRD pattern at 623 K remains unchanged indicating amorphous structure of the ribbons is conserved. Further increase in temperature near T_g at 673 K results in a distortion in XRD pattern of the ribbons revealing very broad peaks of Cu_2Sm phase. Later at 723 K, there are no sign of any extra peaks but present crystalline peaks become more discrete. At 773 K, which corresponds to the end of the main crystallization peak, $Cu_{10}Zr_7$ peaks emerge from the main hump. Combined study of XRD and DSC revealed that main crystallization peak belongs to crystallization of $Cu_{10}Zr_7$ phase which is previously observed in our studies [44,88]. However, in recent study crystallization sequence up to 800 K is as follows:

Amorphous → Amorphous + Cu_2Sm → Cu_2Sm + $Cu_{10}Zr_7$.

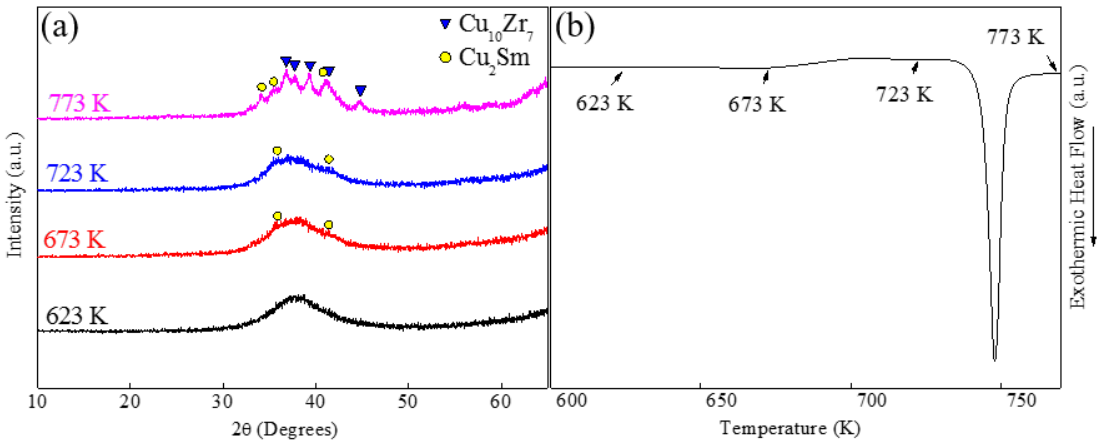

Figure 3. 17 (a) XRD patterns of continuous annealed and subsequently quenched samples, (b) DSC heating curve of melt-spun ribbons with arrows indicating annealing temperatures.

Continuous annealing experiments on ribbon samples revealed the crystallization sequence; however, exothermic crystallization peak of Cu_2Sm is not detected in DSC heating curves. XRD patterns in Fig.3.17 (a) indicates that nanocrystallization of Cu_2Sm phase starts somewhere near step-like endothermic T_g signal. It is possible that endothermic T_g and exothermic Cu_2Sm nanocrystallization signal overlap at around 670-680 K. Furthermore, TEM images shown in Fig.3.21 (a) and Fig.3.21 (b) in following results reveal mostly amorphous structure even at 703 K. Only after sufficient annealing time nanocrystals appear in number. Due to very low amount of Cu_2Sm nanocrystals formed during continuous heating, exothermic crystallization signal may have very low intensity.

3.4.4. TEM and APT Results

TEM images of melt-spun ribbons and 1 mm diameter suction cast rods are shown in Fig.3.18. TEM image of melt-spun ribbon in Fig.3.18 (a) is in good correlation with XRD pattern in Fig.3.15 to prove amorphous nature of the sample. SAED pattern reveal only the diffuse halo ring for melt-spun ribbon indicating there are no sign of crystalline regions present. In contrast, TEM image of 1 mm diameter suction cast rods exhibit spherical crystalline phase with 30 nm size embedded within amorphous matrix. SAED pattern contains crystalline diffraction spots along with the diffuse halo ring, proving amorphous/nanocrystalline composite structure for this sample. Further investigation on 1 mm diameter suction cast rods can be seen in Fig.3.19. HRTEM image combined with SAED pattern in Fig.3.19 (b) reveals the identity of these 30 nm size nanocrystalline solidification products as Cu_2Sm phase as stated before in XRD patterns in Fig.3.15. In addition, STEM and EDS results in Fig.3.19 (a) also shows the composition of the 30 nm size Cu_2Sm nanocrystal as ~76 at. % Cu, ~26 at. % Sm. STEM image shows a certain chemical gradient is present within amorphous matrix as the distance increases further away from crystalline region revealing the sluggish diffusion during growth of Cu_2Sm nanocrystal. TEM image of melt-spun ribbon sample shows fully amorphous nature as cooling rate was sufficient enough to synthesize amorphous phase. Cu_2Sm nanocrystals with 30 nm size were seen for 1 mm

diameter suction cast sample. Relatively lesser cooling rate produced by suction casting method was insufficient to suppress crystallization of Cu_2Sm phase; however, considering STEM image seen in Fig.3.19 (a) further growth thought to be hindered due to sluggish diffusion at lower temperatures and increased Al and Zr pile up at the interface.

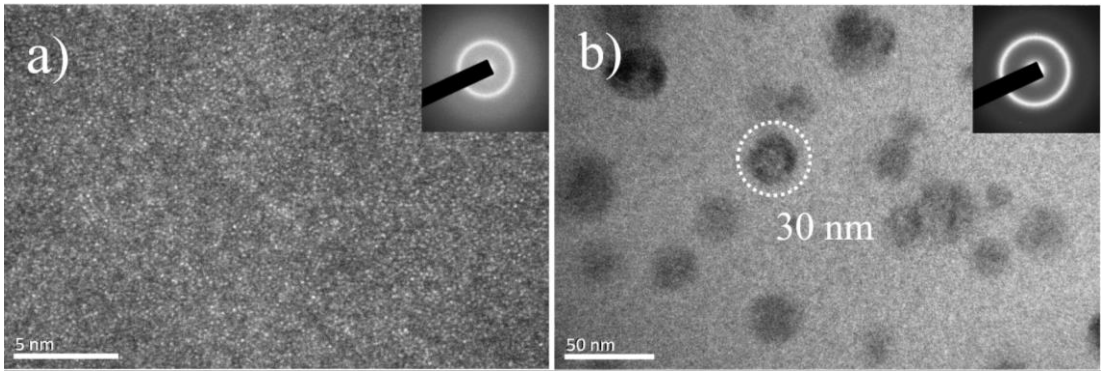

Figure 3. 18 TEM images of as-cast (a) melt-spun ribbons and (b) 1 mm diameter suction cast rods. Insets depicts SAED patterns of each image.

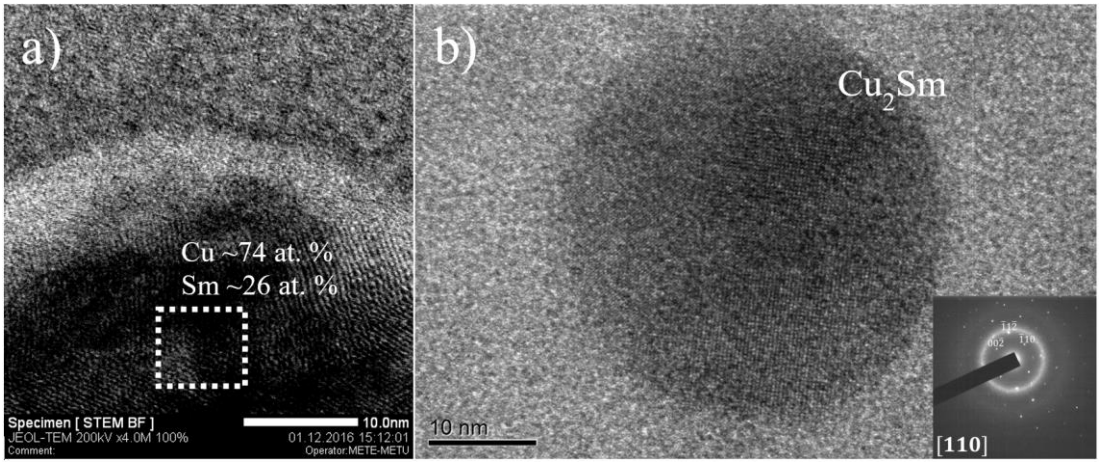

Figure 3. 19 (a) STEM and (b) HRTEM images of as-cast 1 mm diameter suction cast rods showing solidification residue. Insets depicts SAED pattern.

Isothermal controlled crystallization experiments are done to study nanocrystallization of Cu_2Sm phase further. Both melt-spun ribbon samples and 1 mm diameter suction cast rods are isothermally annealed. Isothermal crystallization peaks at 703 K can be seen in isothermal DSC curves in Fig.3.20. Arrows are indicating the annealing time and condition of the samples that are prepared. For ribbon samples, there are 3 sample conditions that are quenched at the onset, A1 (16 min.), at the maxima, A2 (20 min.), and at the end, A3 (26 min.) of the isothermal crystallization peak. Similarly, for 1 mm diameter rod samples conditions are B1 (26 min.), B2 (30 min.), and B3 (34 min.). Annealing times were adjusted due to the shift in peak position. The shift in isothermal crystallization peak position to higher annealing times were discussed earlier.

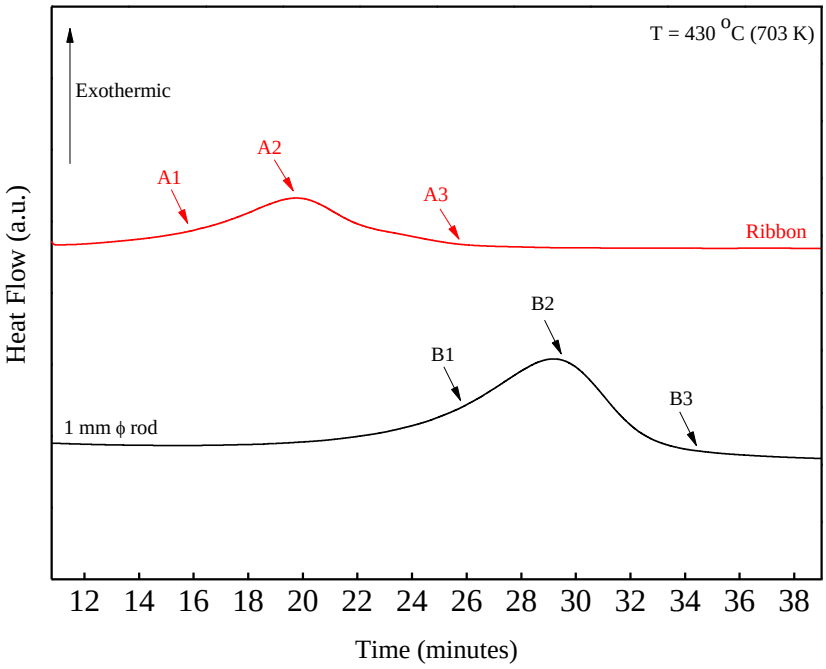

Figure 3. 20 Isothermal DSC curves of melt-spun ribbons and 1 mm diameter suction-cast rods of $(Zr_{50}Cu_{40}Al_{10})_{96}Sm_4$ alloy at 703 K. Interrupt quenched sample conditions are labeled on each trace showing annealing times.

TEM images of isothermally annealed melt-spun ribbon samples are shown in Fig.3.21. TEM image showing A1 (16 min.) condition can be seen in Fig.3.21 (a) and Fig.3.21 (b). At the onset of the crystallization peak, A1 (16 min.) sample remains mainly amorphous as can be seen in SAED pattern at inset of Fig.3.21 (a). However, there are 5 nm size crystalline regions are present where planes can be seen in HRTEM image in Fig.3.21 (b). At the maxima of the crystallization peak, A2 (20 min.), crystalline regions become clearly visible as shown in Fig.3.21 (c) and Fig.3.21 (d). Nanocrystal size grow up to approximately 8-10 nm size. In Fig.3.21 (d) inset shows FFT obtained from nanocrystal which supports Cu_2Sm phase as well. Fig.3.21 (e) and Fig.3.21 (f) depicts the end of the crystallization peak, A3 (26 min.) revealing higher nanocrystal density in comparison to condition A2. Nanocrystal size remain mostly constant at about 8-10 nm size at condition A3 similar to A2. TEM images in Fig.3.21 shows the isothermal evolution of Cu_2Sm nanocrystals through time. The nanocrystal radius is 5 nm at the onset of the crystallization and increases up to 8-10 nm through maxima of the crystallization peak. Up to end of the crystallization peak nanocrystal size remain mostly constant, while new nanocrystals nucleate and none of the observed nanocrystals exceed 10-11 nm size. Considering these observations, it is possible to state that nucleation of new nanocrystals is preferred by the system instead of growth of already present ones. Statement may gain more verification after results of APT analysis when concentration of Sm within amorphous phase is considered.

In parallel, TEM images of isothermally annealed 1 mm diameter suction cast rod samples are shown in Fig.3.22 Similarly, TEM images showing B1 (26 min.) condition can be seen in Fig.3.22 (a) and Fig.3.22 (b). At the very early stages of the crystallization, B1 (26 min.), sample exhibits two distinct microstructural features: 30 nm size spherical Cu_2Sm crystals that are formed during solidification and 5 nm size spherical Cu_2Sm nanocrystals originated from isothermal annealing. Distribution of annealing nanocrystals appear to be quite homogenous in whole structure. At the maxima of the isothermal crystallization peak, B2 (30 min.), structure does not change drastically as seen in Fig.3.22 (c) and Fig.3.22 (d). Size of annealing nanocrystals remain mostly constant at about 5-6 nm, while nanocrystal number appear to be

increasing slightly as seen in Fig.3.22 (c). Compositional difference due to solute rejection is more evident even in bright-field TEM image for this sample revealing sluggish growth of Cu_2Sm phase during solidification. Structure of the sample at the end of the crystallization, B3 (34 min.) is shown in Fig.3.22 (e) and Fig.3.22 (f) illustrating similar results to B2 (30 min) condition. Nanocrystal size remains constant at 5-6 nm at this stage as well.

TEM images in Fig.3.22 reveal that Cu_2Sm crystallization during solidification does not change the phase selection sequence during isothermal annealing. TEM images in Fig.3.22 illustrate that structure consists of 30 nm size solidification originated and 5-6 nm size annealing originated spherical Cu_2Sm nanocrystals. Unlike nanocrystals in annealed ribbon samples, annealing nanocrystals in 1 mm diameter rod samples remain at constant size throughout annealing. In addition, nanocrystals in ribbon samples are larger compared to the annealing nanocrystals in 1 mm diameter rod samples. Main cause of constant and smaller nanocrystal size is attributed to the Sm shortage in the system. In upcoming APT results, amorphous matrix is found to be depleted from Sm atoms from the concentration profiles in Fig.3.23 (e). Since there are no Sm atoms available for growth of the annealing nanocrystals, their size remains constant at 5-6 nm. Moreover, since Sm atoms are also used up for 30 nm size Cu_2Sm solidification crystals, annealing nanocrystals cannot grow further up to 10-11 nm size. Considering TEM results for 1 mm diameter rod samples, Sm amount is definitely a limiting step for size of Cu_2Sm nanocrystals, which can be adjusted by changing composition with further study.

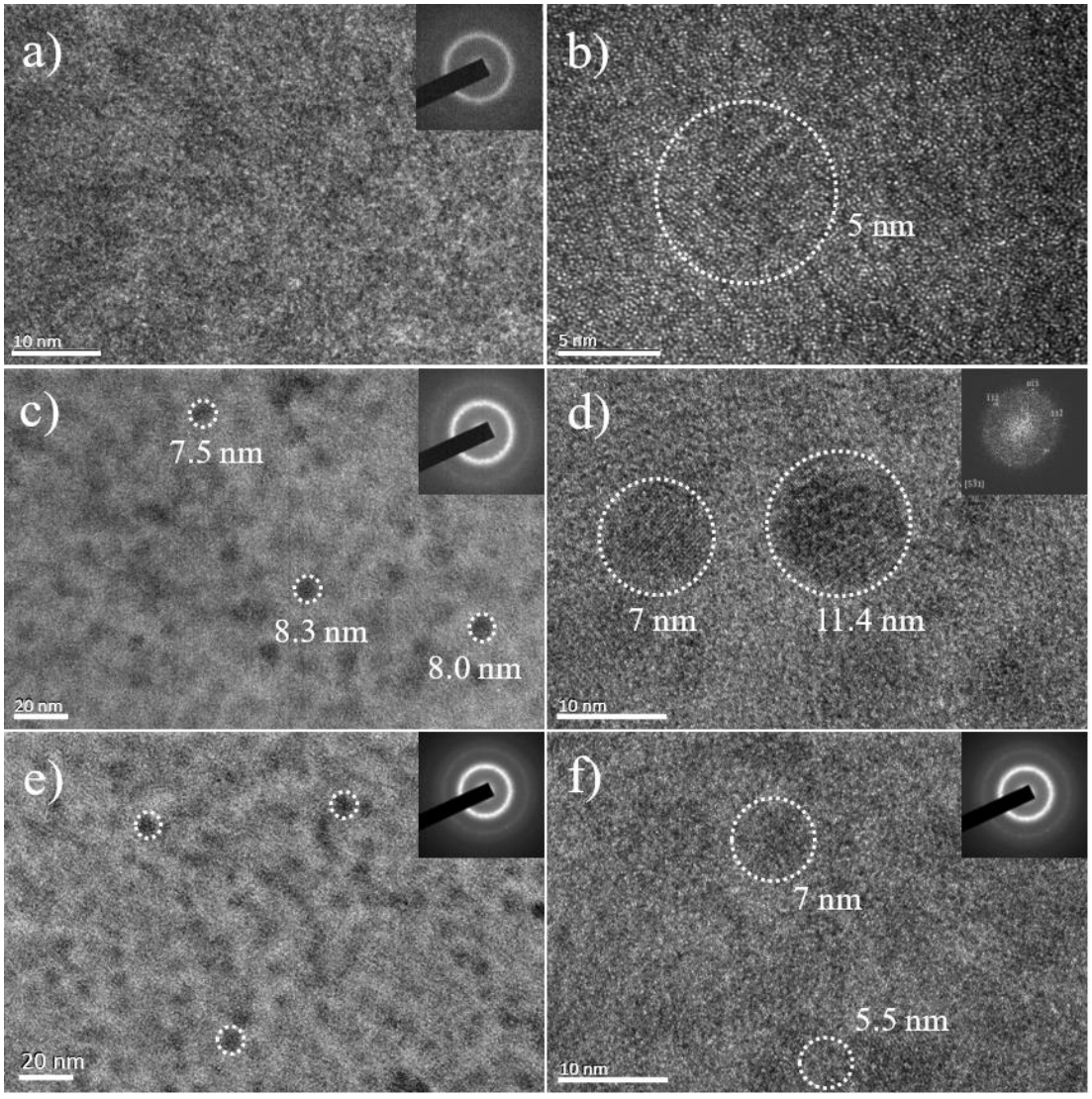

Figure 3. 21 TEM images of isothermally annealed melt-spun ribbons at annealing condition A1 (a, b), A2 (c, d), and A3 (e, f) as shown in Fig. 3. Insets shows SAED patterns and FFT for each image. Circles show examples of nanocrystals.

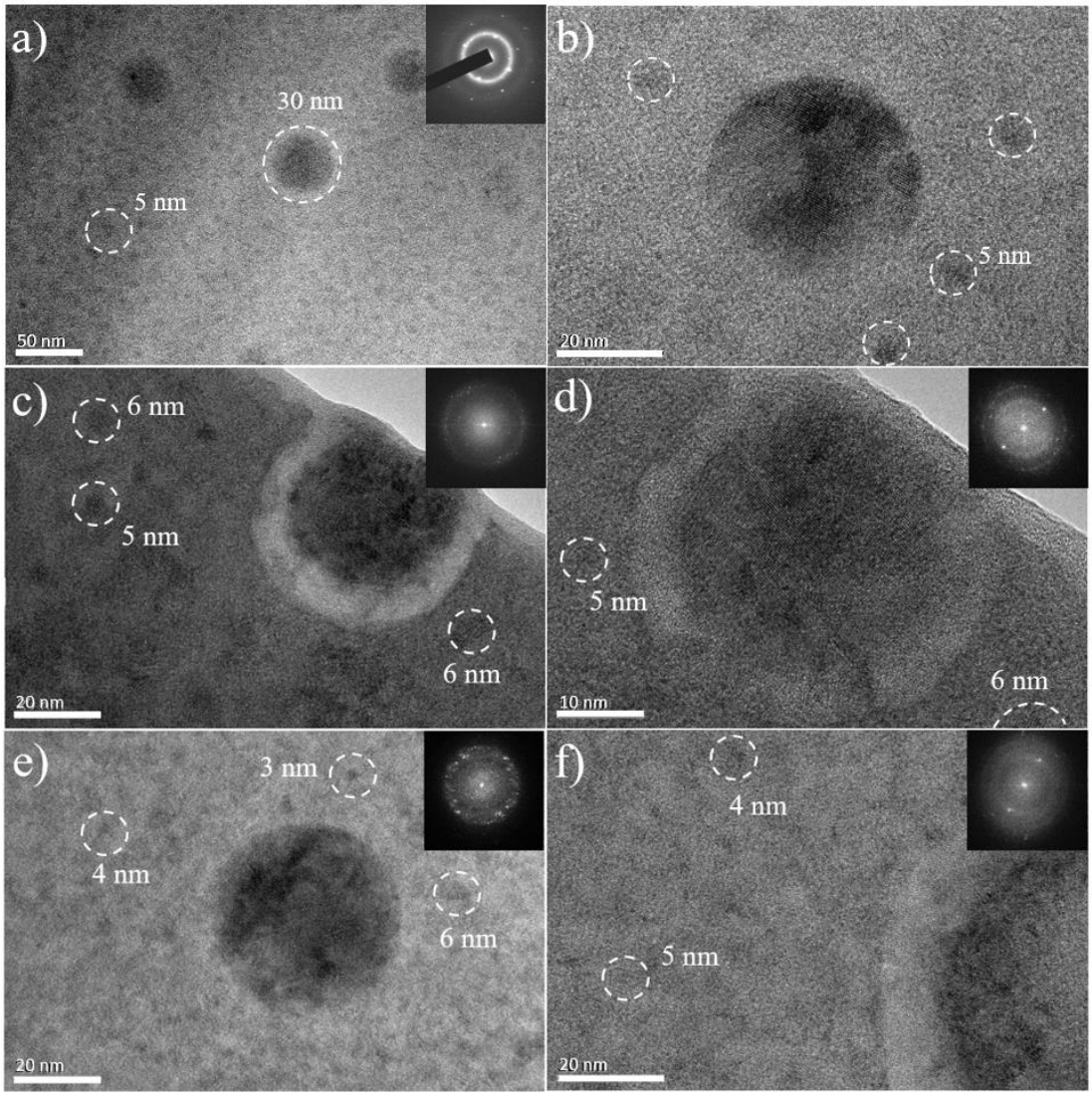

Figure 3. 22 TEM images of isothermally annealed 1 mm diameter suction cast rods at annealing condition B1 (a, b), B2 (c, d), and B3 (e, f) as shown in Fig. 3. Insets shows SAED patterns and FFT for each image. Circles show examples of nanocrystals.

Fig.3.23 (a, b, c, d) indicate APT results showing atomic spatial distribution of constituent elements of the alloy composition, namely Cu, Sm, Zr, Al, in an 80x70 nm^2 tip area for 1 mm diameter suction cast rod at condition B1. Atomic distributions of Al and Zr are quite homogenous as seen in Fig.3.23 (c) and Fig.3.23 (d). In contrast, accumulation of Cu and Sm atoms in certain regions are apparent in Fig.3.23 (a) and Fig.3.23 (b). These segregations are in such a form that; they can be classified into two groups. First one is the thick needle-like Cu and Sm aggregation at the right corner, the other ones are small clusters of Cu and Sm atoms all around the tip area. Considering TEM image of this sample in Fig.3.22, thick needle-like Cu and Sm aggregation represents the edge of 30 nm size Cu_2Sm solidification product and clusters represents the 5 nm size Cu_2Sm annealing nanocrystals. In addition, Fig.3.23 (e), represents concentration profile of the region of interest (ROI) that is extracted from whole APT data. As seen in Fig.3.23 (e) left-hand side of ROI is at the 30 nm size solidification crystal and right-hand side is at 5 nm size annealing crystal. Concentration of Cu and Sm increases up to approximately 60 at. % and 30 at. % respectively at solidification crystal side. As distance increase further away from Cu_2Sm into the amorphous matrix, both Cu and Sm concentration gradually decreases. On the other hand, both Zr and Al concentration increase due to solute pile-up. Concentration profile reveals composition of amorphous matrix is approximately $Zr_{55}Cu_{45}Al_{10}$. At the right-hand side of ROI, again concentration of Cu and Sm increases due to the presence of 5 nm size Cu_2Sm annealing nanocrystal. Cu and Sm concentration reach up to approximately 40 at. % and 10 at. % respectively. APT results give valuable information about the nanocrystallization of Cu_2Sm phase. Full comprehension of APT data can only be obtained by TEM images given in Fig.3.22 (b), which is the corresponding TEM image of same sample. As mentioned before, atomic distribution of Cu and Sm are sharing two major features. The thick needle-like feature at right corner represents edge of the 30 nm size Cu_2Sm solidification crystals from the Fig.3.22 (b). Size and composition of the chunky Cu-Sm agglomeration is quite matching with the TEM image. Cu and Sm spherical clusters are also present all around the tip area. In Fig.3.22 (b), 5 nm size spherical Cu_2Sm

annealing crystals are also present around the solidification crystals. APT results and TEM images in Fig.3.22 are in good correlation. Concentration profile suggests that composition of annealing nanocrystals is not exactly same with Cu_2Sm stoichiometry. However, APT sample is at condition B1, which is the onset of the crystallization peak meaning at a very early stage of nanocrystallization. It may be possible that the nucleation of Cu_2Sm phase is not completed yet. Another reason for such error may be detection efficiency of APT instrument. Low detection limit may not be a problem for larger nanocrystals such as in case of 30 nm size solidification crystal, but cause problems for smaller nanocrystals. FFT in Fig.3.21 (d) indicates annealing crystals are also Cu_2Sm for ribbon samples. Nevertheless, it was impossible to perform diffraction from annealing nanocrystals in rod samples within TEM due to their small size. Their true identity can only be speculated with present data.

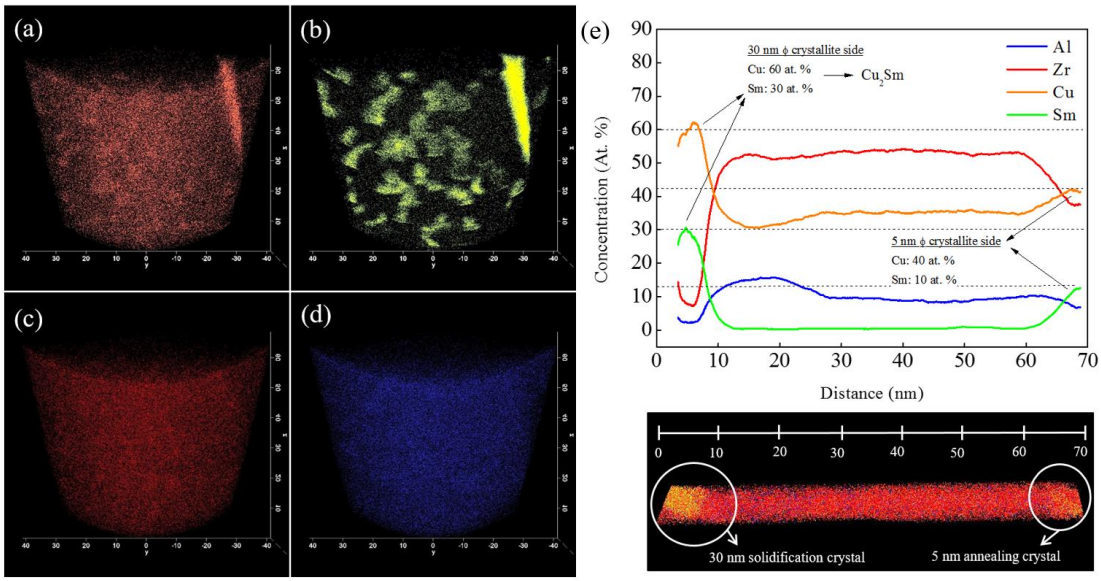

Figure 3. 23 APT results showing atomic spatial distributions of (a) Cu, (b) Sm, (c) Zr, and (d) Al and (e) concentration profile of a nanocrystal/amorphous intersection region extracted from APT data for 1 mm diameter suction cast rod at B1 condition.

Fig.3.24 illustrates the cross sectional 2D elemental contour maps of isothermally annealed 1 mm diameter suction cast rod at B1 along with a STEM image of the sample. Elemental contour maps in Fig.3.24 (b) reveal that 5 nm large nanocrystals are rich in Cu and Sm atoms. Results showed that Zr is rejected to amorphous matrix at crystalline/amorphous interface during nanocrystallization. Solute pile-up of rejected elements during growth are even observable for fine scale nanocrystals in APT anaylsis. It is tougth that combined effect of Zr pile up at interface and insufficiency of Sm resulted in a hindered growth and nanocrystallization for this alloy system.

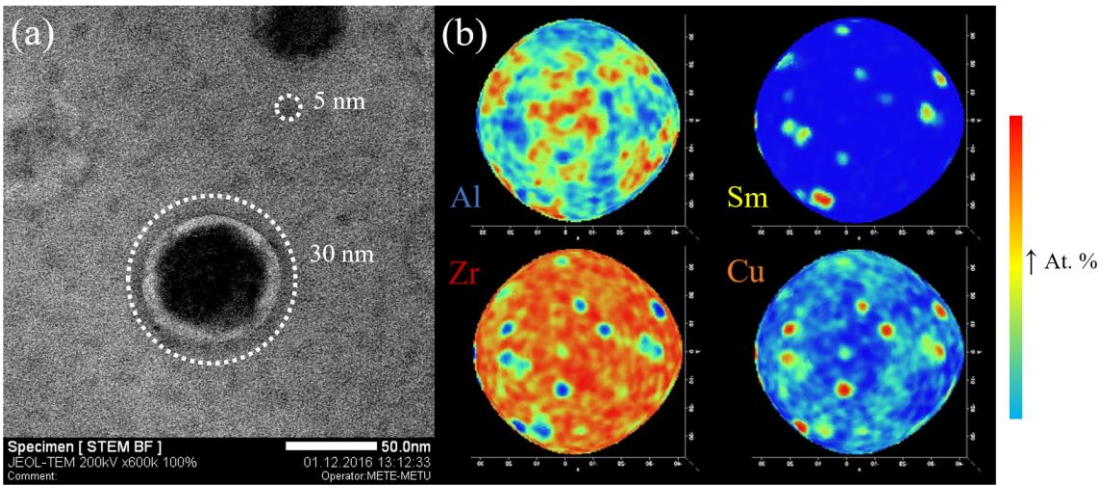

Figure 3. 24 (a) STEM image and (b) cross sectional 2D elemental contour maps of isothermally annealed 1 mm diameter suction cast rod at B1 condition.

Earlier it was stated that growth cannot continue for Cu_2Sm nanocrystals. Considering the composition of the amorphous phase in concentration profile in Fig.3.23 (e), amorphous matrix is almost completely depleted from Sm atoms. Since in order to satisfy growth of Cu_2Sm nanocrystals, Sm diffusion is required for stoichiometry. When matrix is insufficient of Sm in order to feed Cu_2Sm nanocrystals, growth cannot continue any further. This may also bring up some designing aspect to this microstructure. It may be possible to control size of these nanocrystals, by controlling the Sm content during microalloying.

3.5. Conclusion

Glass forming ability and thermal properties of $(Zr_{50}Cu_{40}Al_{10})_{100-x}Sm_x$ (x=0, 2, 4 at. %) alloys have been investigated in a combined study of DSC and XRD and shown in preliminary results. All composition samples are produced in both 1 mm diameter suction cast rods and melt-spun ribbon forms after preparing ingots in arc-melter from high purity elements of the systems. XRD analysis showed melt spun ribbons were fully amorphous, while suction cast rods were partially crystalline. According to XRD results of 1 mm suction cast rod samples, GFA is found to increase with Sm addition. Furthermore, DSC analysis has revealed that micro alloying Sm up to 4 at. % in the $Zr_{50}Cu_{40}Al_{10}$ alloy decreases ΔT_x, which is considered to be related to the thermal stability of the amorphous phase. ΔT_x and GFA is thought to be proportional in literature; however, there are many BMG systems where the addition of Gd and Nd rare-earths show high GFA for relatively low ΔT_x.

Crystallization kinetics were investigated for $(Zr_{50}Cu_{40}Al_{10})_{100-x}Sm_x$ (x=0, 2, 4 at. %) alloys. It is found that activation energy for crystallization of $Cu_{10}Zr_7$ phase increased with increasing Sm content. It is concluded that, higher activation energy caused by distortion of Cu-Zr atomic pairs with increased Sm atoms in the system. Positive enthalpy of mixing between Zr and Sm atoms thought to be the main cause of this phenomenon. Higher activation energy for crystallization of $Cu_{10}Zr_7$ phase also causes a change in phase selection during devitrification. Primary crystallization shifted from CuZr to Cu_2Sm nanocrystals during rapid solidification and from $Cu_{10}Zr_7$ to Cu_2Sm nanocrystals during devitrification.

Nanocrystallization of $(Zr_{50}Cu_{40}Al_{10})_{96}Sm_4$ alloy have been investigated in combination of DSC, XRD, SEM and APT. Based on XRD analysis, fully amorphous melt-spun ribbons and partially crystalline suction cast rods with 1, 2, and 3 mm diameter were produced. TEM and APT investigations showed that Sm triggers nanocrystallization of spherical Cu_2Sm phase. In case of 1 mm rod samples microstructure contained of 30 nm large Cu_2Sm nanocrystals in as-cast state. Isothermal annealing nucleated 5 nm large Cu_2Sm nanocrystals embedded in partially crystalline matrix. In case of melt-spun ribbon samples, isothermal annealing initiated

nanocrystallization of 10 nm large Cu_2Sm phase. APT and TEM analysis showed that growth of spherical Cu_2Sm nanocrystals hindered by rejected Zr atoms at amorphous/crystalline interface and insufficiency of Sm atoms in amorphous phase. Nanocrystal size is found to be limited by the Sm content within the composition which may be used to control nanocrystal size and distribution with further study.

CHAPTER 4

MECHANICAL PROPERTIES AND SHEAR BAND STABILITY OF Cu-Zr-Al-Sm BULK AMORPHOUS/NANOCRYSTALLINE COMPOSITE

4.1. Introduction

Mechanical enhancement in terms of ductility and toughness of metallic glasses become hot topic in material science due to their promising strength and elastic properties. Metallic glasses have strength values reaching up to the theoretical strength values due to lack of crystalline defects within the structure; however, their plasticity is very limited. Common recent effort in literature is to enhance their ductility by introducing a second phase either by phase separation of two amorphous structure or nanocrystalline/amorphous composite structure. In this chapter, mechanical characterization of $(Zr_{50}Cu_{40}Al_{10})_{100-x}Sm_x$ (x=0 and 4 at. %) alloy compositions were performed on both suction-cast rods and melt-spun ribbons via combined study of Vickers hardness tests, conventional compression tests and micro-pillar compression tests. Effects of nanocrystals on mechanical properties and effects of indentation load on hardness and strain rate and sample sizes on compressive strengths are discussed.

4.2. Literature Review

4.2.1. Mechanical Properties of Metallic Glasses

Much different from crystalline metals and alloys, amorphous bulk metallic glasses have very unique and promising physical, chemical and most importantly mechanical properties [7,20,89,90]. Due to lack of crystalline lattice and consequently lattice defects bulk metallic glasses exhibit extraordinary strength and elasticity [13]. A simple illustration of their strength and elasticity compared to conventional crystalline materials are given in Fig.4.1. It is shown that most of the bulk metallic glasses are exceeding both steels and titanium alloys in strength and few polymers in elasticity. However, engineering applicability of metallic glasses are very limited despite their superior mechanical properties due to the lack of plasticity in their fully amorphous state. Metallic glasses exhibit very limited plasticity under both tension and compression loading.

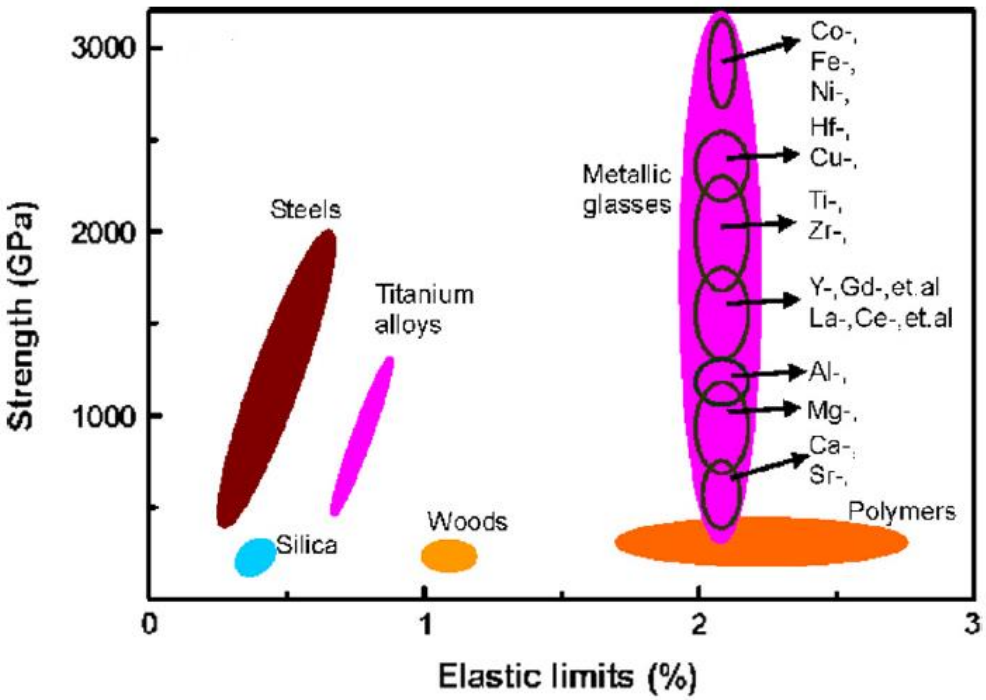

Figure 4. 1 Comparison of metallic glasses and conventional engineering materials in strength – elastic limit plot. Adopted from [13].

4.2.2. Deformation and Fracture of Metallic Glasses

Deformation and fracture mechanisms of metallic glasses have quite unique - characteristics due to their amorphous structure [91–93]. Fracture mechanisms and types of metallic glasses are discussed in Chapter 1. Similarly, deformation behavior of metallic glasses strongly depends on temperature and strain rate. Deformation occurs homogenously at temperatures close to glass transition temperature or at low strain rates. In this case, deformation can be viewed as a viscous flow. In contrast at low temperatures or at high strain rates, plastic deformation localizes on narrow nano-scale regions. These nano-scale regions are labeled as shear bands and give valuable information about mechanical properties of metallic glasses [20]. Determination of nucleation and growth (propagation) of these so-called shear bands are at utmost importance for understanding of the plasticity of a metallic glass. Stability of shear bands during loading is the main concern for a mechanically stable metallic glass.

4.2.3. Shear Band Stability and Micropillar Compression Tests

Investigation of nucleation and propagation speed of shear bands for metallic glasses under loading attract much attention in order to understand the dynamics of shear banding phenomenon. Stability of shear band is attributed with a lower shear band propagation speed or with an arrested strain burst events. For relatively brittle metallic glasses strain burst events are found to be much more discrete compared to ductile metallic glasses [24,39,94–96]. Observations of these strain burst events are as important as it creates a challenge. Due to low temporal and spatial resolution of characterization techniques only few datum points were recorded during strain burst events in early studies [97].

In this respect, researchers focus on compression tests of micro-pillar samples which are prepared in FIB. Literature shows various studies investigating strain burst and stress drop events associated with shear band propagation or studies concerning effects of strain rate or temperature on shear band stability [46, 96]. Meanwhile, some studies

focus on reliability of these micro-pillar compression tests by investigating effects of sample size or tapper angle [47,48,98].

Lai *et. al.* studied the effect of base element on the shear band dynamics using Zr, Au, and Mg-based bulk metallic glasses. In their study, correlation of strain burst speed with raw displacement-time profile revealed that for so-called ductile metallic glasses such as Zr-based BMGs strain burst speed is lower compared to brittle Mg-based BMGs. In addition, an inverse relation between strain burst speed and elastic modulus is shown revealing enhanced ductility for alloys with a low strain burst speeds [96]. Fig.4.2 depicts deformed appearances of 3.8 mm diameter micro-pillar samples revealing much lower displacement of the sheared plane regions for Zr-based BMG compared to Mg and Au-based BMGs.

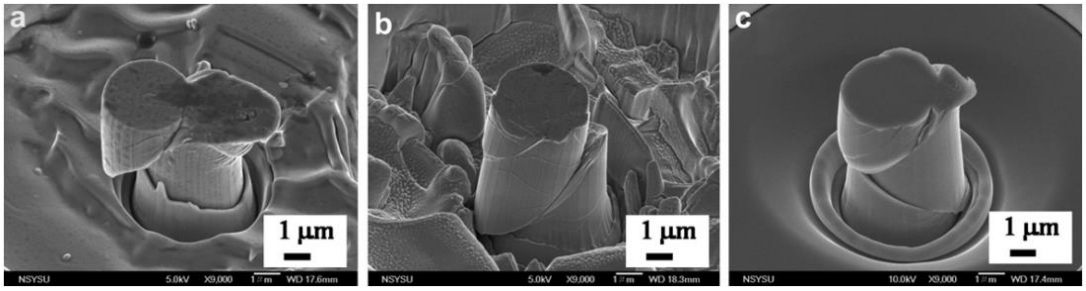

Figure 4. 2 SEM micrographs showing the appearance of 3.8 mm deformed pillars of (a) Mg-, (b) Au- and (c) Zr-based BMG. Adopted from [96].

Effects of sample size and base metal on shear band stability is investigated by Ke *et. al.* in their recent paper. The variation of the average stress-drop or strain burst duration t_L for a typical serration event with the diameter of the different MG micro-pillars are shown in Fig.4.3. It is evident that increasing sample diameter causes an increase in serration event duration for all base metals indicating strain burst events are much more evident for larger samples. In other words, shear band propagation is much more catastrophic for larger BMGs. This phenomenon is in good correlation with the known concept of smaller the better for metallic glasses. [99,100]

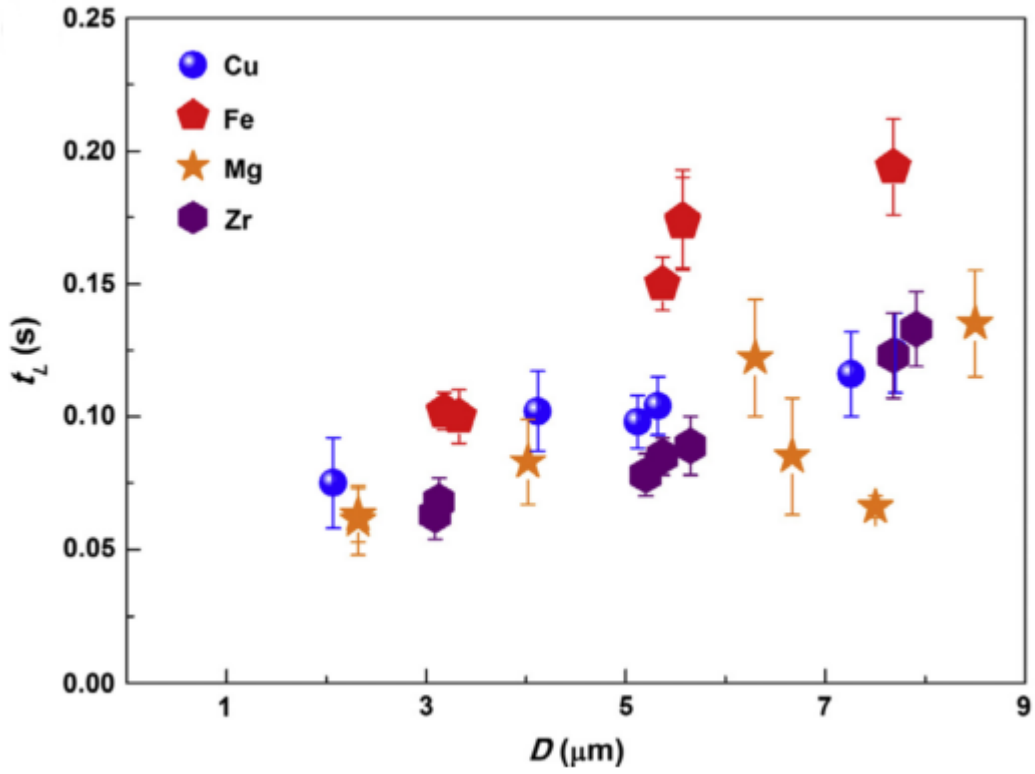

Figure 4. 3 The variation of the average duration t_L for a typical serration event with the diameter of the different MG micro-pillars. Adopted from [98].

In Fig.4.3 strain burst durations appear to be highest for Fe-based BMGs and lowest for Zr-based BMGs. Shorter strain burst events are correlated with alloy compositions where shear band propagation is slower and easily arrested. Since shear bands cannot propagate rapidly and catastrophically sample remains mechanically stable and thus appear more ductile. In macro-scale Zr-based metallic glasses are also known to have relative ductility. In case of Fe-based metallic glasses strain burst duration is much higher compared to Zr-based metallic glasses. Rapid shear band propagation speed causes rapid fracture and brittleness for Fe-based metallic glasses [98].

Ye *et. al.* studied the effects of tapper angle on micro-pillar compression tests results, revealed that 5^o or higher tapper angle causes a 20% overestimation during determination of the yield strength. In their study, they also revealed that shear band

position is also affected by tapper angle [48]. Fig.4.4 illustrates the schematic of tapper angle and its effects. Tapper angle is shown with angle β, the distance between centerline and shear band origin point is shown with d and shear angle is shown with θ. According to the figure, shear band originates from corner point if η is equal to 1. Increase in tapper angle triggers a decrease in η and consequently d, shifting shear band origin point into the centerline. As shear band shifts to center of the specimen, generally shear angle θ increase, shear band branches and error in estimated strength and modulus increases [48].

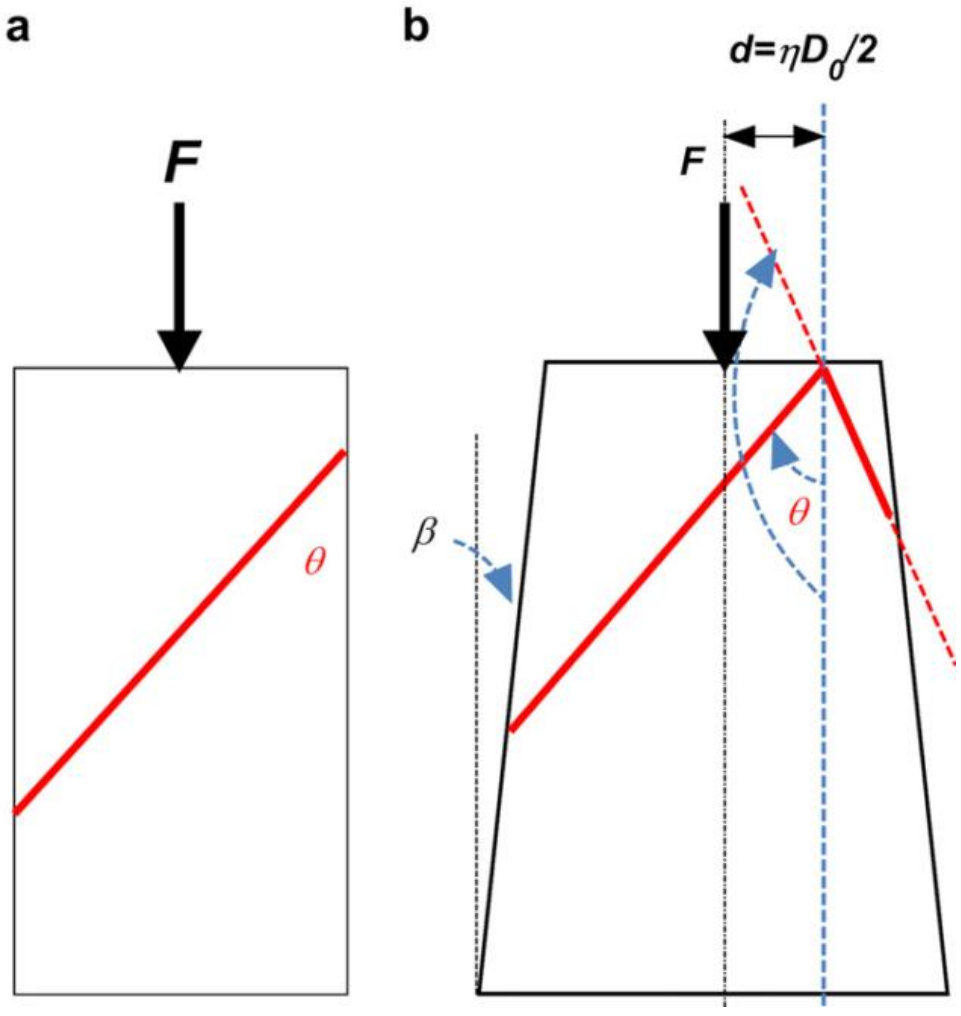

Figure 4. 4 Sketches of the shear band angle and shape in case of (a) non-tapered and (b) tapered micro-pillars. Adopted from [48].

4.3. Experimental Procedure

4.3.1. Production of Alloys

Melt-spun ribbons of 40 μm thickness and suction cast rods samples of 1, 2, and 3 mm diameter rods of $(Zr_{50}Cu_{40}Al_{10})_{100-x}Sm_x$ (x=0, 2, 4 at. %) alloy composition samples are prepared by the same procedure and methods that are explained in Chapter 3. In this particular chapter same samples in both ribbon and cast rod form are characterized via macro and micro mechanical testing.

Focused Ion Beam (FIB) Milling

Cylindrical micropillar samples with diameters of 1, 1.5, and 3 μm are prepared out of ribbon samples by focused ion beam technique (FIB). Micropillar compression tests are performed since melt-spun ribbon samples are not in a suitable shape for macro scale mechanical testing methods such as tensile or compression testing. Micropillar compression tests not only gave a chance to perform mechanical testing but also a way to inspect sample size effect on mechanical properties.

Micropillar compression sample preparation is very similar to TEM sample preparation in FIB. Sample surface is again bombarded with Ga ions in order to mill the surface mechanically. Ga ions are concentrated on a circular region and milled down while center of the region of interest is left untouched. In other words, milling is applied to the surface with a hallow circle shape. As milling proceeds cylindrical pillar forms on the surface of the sample due to decrease in base level.

One important problem of FIB milling is the tapering angle of pillars. In some cases, milling can introduce an inclined pillar surface, where radius increases through bottom of the pillar. In spite of all the care a certain tapper angle is introduced in our samples during sample preparation. This tapper angle is generally between 2-5^o.

4.3.2. Vickers Micro-hardness and Macro Scale Compression Tests

Macro scale compression tests in Chapter 2 are repeated in Chapter 4 with samples with higher amorphous proportions according to the XRD. Main purpose of macro

scale compression tests in Chapter 4 are to help comprehend fracture characteristics. The mechanical properties of the suction cast rod samples of $Zr_{50}Cu_{40}Al_{10}$ and $(Zr_{50}Cu_{40}Al_{10})_{96}Sm_4$ were investigated under compressive load by using Instron 5582 mechanical testing equipment with max. 100 kN shown in Fig.2.10 (a). Specimens were prepared for compressive test according to the ASTM standards, with the gauge dimensions of 3.0 ± 0.3 mm in diameter and 6.0 ± 0.3 mm in length (with an aspect ratio of 2:1). The compressive tests were conducted with the crosshead speed of 0.03 mm/min and corresponding strain rate of 10^{-4} s^{-1} at room temperature. Macro scale specimens are prepared and tested by the same procedure and methods that are explained in Chapter 2.

Vickers micro-hardness tests are performed on both 40 μm thick melt-spun ribbon and 1 mm diameter suction cast rod samples of $(Zr_{50}Cu_{40}Al_{10})_{100-x}Sm_x$ (x=0, 2, 4) compositions. Vickers micro-hardness tests are performed at 0.1 kgf and 2 kgf load with an indentation time of 10 seconds for at least 10 test indents per specimen. Indent size is evaluated on optical microscope to calculate Vickers hardness.

4.3.3. Nano Indentation and Micro Scale Compression Tests

Nano indentation experiments were performed by using an Agilent G200 Nanoindenter. A diamond Berkovich tip was used. The measurements were displacement controlled and in continuous stiffness measurement mode. This allowed the determination of hardness values as a function of depth into the specimen. For some selected measurements, the data acquisition rate was increased to 200 Hz to be able to track the displacement bursts. Micropillar compression experiments were performed by using the same instrument and by utilizing a flat diamond punch in conical form with a flat circular end of 10 um diameter. Compression tests were performed in displacement controlled mode with linear loading and unloading stages. Three different loading rates were applied which corresponded to strain rates around 10^{-2}, 10^{-4} and 10^{-5} s^{-1}. Tests are repeated at least 3 times for most of the samples.

4.4. Results and Discussion

Vickers micro-hardness results of ribbons and 1 mm diameter rod $(Zr_{50}Cu_{40}Al_{10})_{100-x}Sm_x$ (x=0, 2, 4 at. %) samples are shown in Fig. 4.5. Measured Vickers micro-hardness values are also converted to MPa for sake of comparison. Micro-hardness profile with respect to increasing Sm content reveals a decreasing trend for both ribbon and cast rod samples. It is evident that micro-hardness values for rod specimens are slightly higher compared to ribbon specimens. Higher hardness of rod specimens are tougth to be due to their partially crystalline nature and intermetallics within them. Higher correspondence of hardness of the rod and ribbon specimens for $(Zr_{50}Cu_{40}Al_{10})_{96}Sm_4$ composition also supports this statement due to higher amorphous content of this alloy in cast rod condition. Measured micro-hardness and standard deviations of samples are tabulated in Table 4.1.

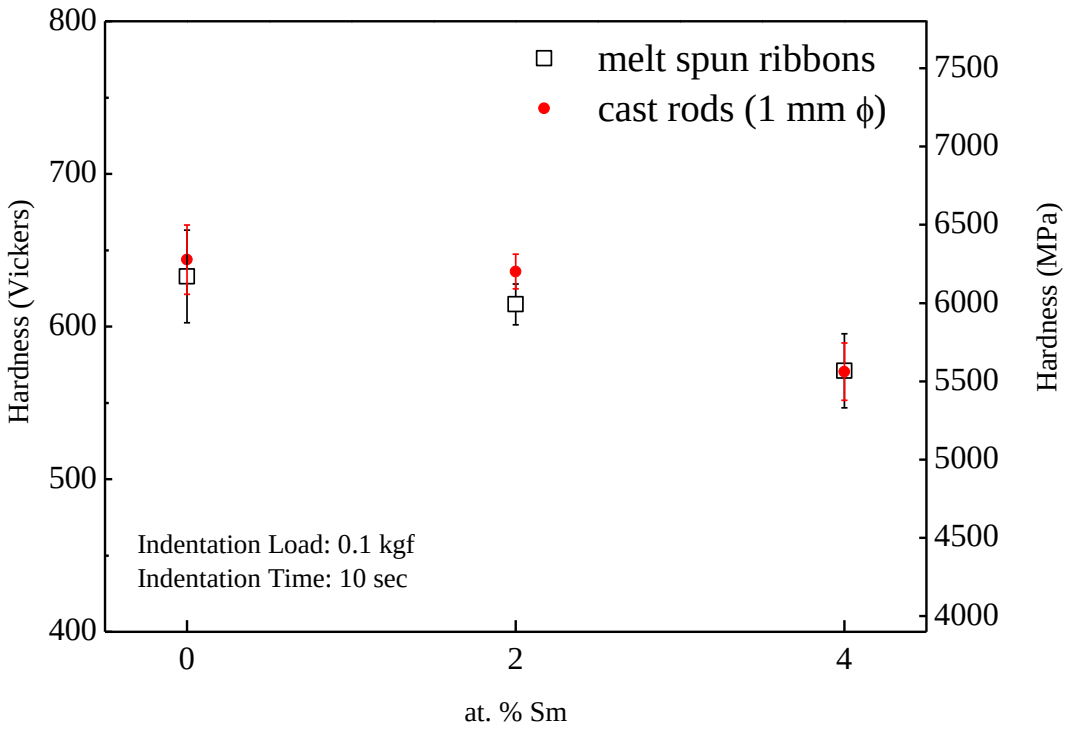

Figure 4. 5 Vickers micro-hardness profile of 1 mm diameter suction cast rods and 40 μm thick melt-spun ribbon $(Zr_{50}Cu_{40}Al_{10})_{100-x}Sm_x$ (x=0, 2, 4 at. %) at 0.1 kgf load.

Table 4. 1 Vickers micro-hardness results of 1 mm diameter suction cast rods and 40 µm thick melt-spun ribbon $(Zr_{50}Cu_{40}Al_{10})_{100-x}Sm_x$ (x=0, 2, 4 at. %) at 0.1 kgf load.

	Vickers Micro-hardness (HV)		
Sample Condition	**0 at. % Sm**	**2 at. % Sm**	**4 at. % Sm**
1 mm Ø cast rod	644 ± 23	636 ± 11	570 ± 19
40 µm thick ribbon	633 ± 30	615 ± 13	571 ± 24

Table 4.1 shows that hardness of $(Zr_{50}Cu_{40}Al_{10})_{100-x}Sm_x$ (x=0, 2, 4 at. %) samples are decreasing from 644-633 HV (6.3 GPa) down to 636-615 HV (6.1 GPa) with 2 at. % Sm and then continued to decrease to 570 HV (5.6 GPa) with 4 at. % Sm addition. Sm micro alloying induced an aparent softening in $Zr_{50}Cu_{40}Al_{10}$ alloy system.

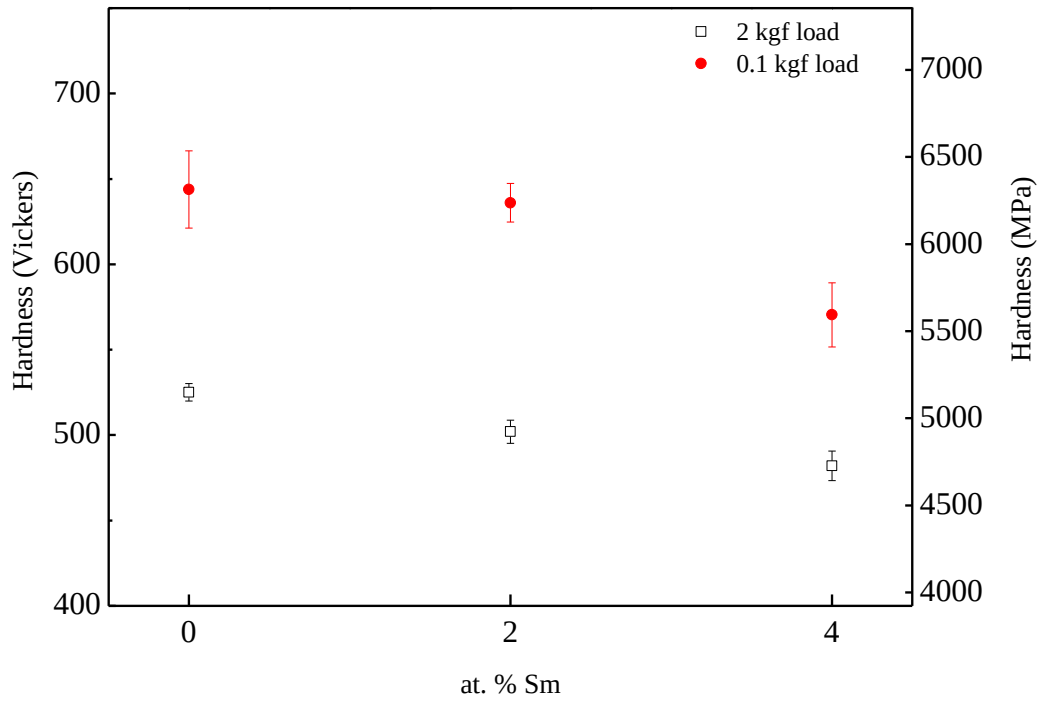

Figure 4. 6 Vickers micro-hardness results of 1 mm diameter suction cast $(Zr_{50}Cu_{40}Al_{10})_{100-x}Sm_x$ (x=0, 2, 4 at. %) rods at various indentation loads.

Effect of indentation load on Vickers micro-hardness is studied using 2 kgf indentation load on 1 mm diameter suction cast $(Zr_{50}Cu_{40}Al_{10})_{100-x}Sm_x$ (x=0, 2, 4 at. %) rods and results are given in Fig. 4.6. As it is shown in figure, decreasing trend of micro-hardness with increasing Sm content is also revealed under 2 kgf indentation load; however, all micro-hardness values are relatively lower compared to 0.1 kgf indentation load. Main reason of lower micro-hardness values is considered to be indentation size effect (ISE) [101]. ISE states that measured hardness values decreases with increasing indentation depth instead of converging a constant value. While the rate of this decrease is more pronounced at lower depths, it is gradually decreases as indentation depth increases. Although ISE is generally observed for crystalline materials in literature [102], there are several studies revealing that ISE is observed on hardness-depth profiles of amorphous metals as well [103]. For amorphous metals ISE is explained by free volume theory. During indentation continuously generated plastic deformation causes an excess free volume in indent vicinity, which attributes as a gradual softening mechanism. As indentation proceeds, softening of metallic glasses occur resulting in a decrease in observed hardness. ISE is observed for both micro-hardness and nano indentation experiments for metallic glasses in literature [104].

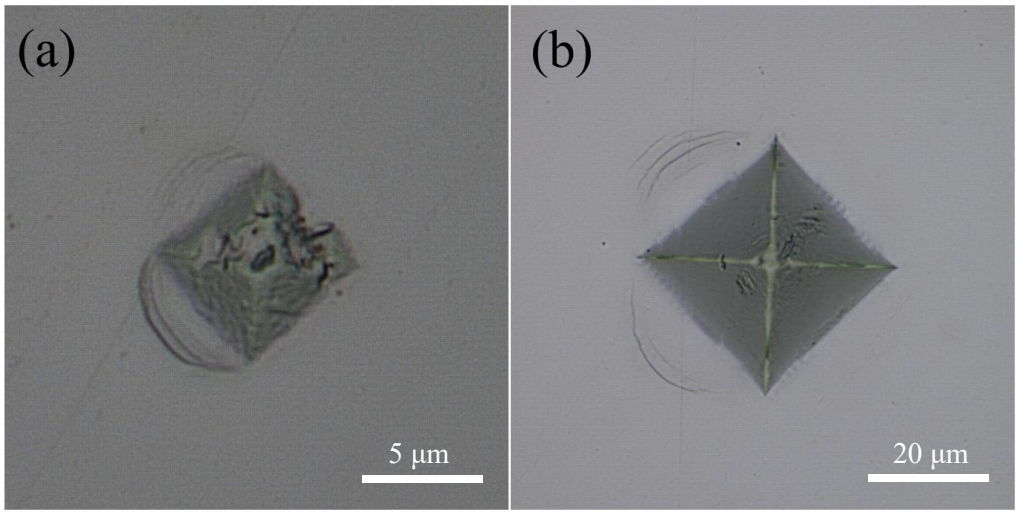

Figure 4. 7 Vickers micro-hardness indent marks at (a) 0.1 kgf and (b) 2 kgf load on 1 mm diameter $Zr_{50}Cu_{40}Al_{10}$ suction cast rods.

Optical microscope images of Vickers micro-hardness indent marks on 1 mm diameter $Zr_{50}Cu_{40}Al_{10}$ suction cast rods for 0.1 kgf and 2 kgf indent load are given in Fig. 4.7 (a) and Fig. 4.7 (b) respectively. Shear bands are observed near the marks revealing the effect of plastic deformation on the samples. It is important to note that shape of the indent mark at 0.1 kgf is distorted compared to the one at 2 kgf. Distorted indent mark effect can be seen in error bars of 0.1 kgf load in Fig. 4.6. Error bars of 0.1 kgf load are relatively larger compared to 2 kgf load, however, hardness value deviation caused by the distorted indent causes not a severe miscalculation to obscure effect of Sm micro alloying on $Zr_{50}Cu_{40}Al_{10}$ alloy system.

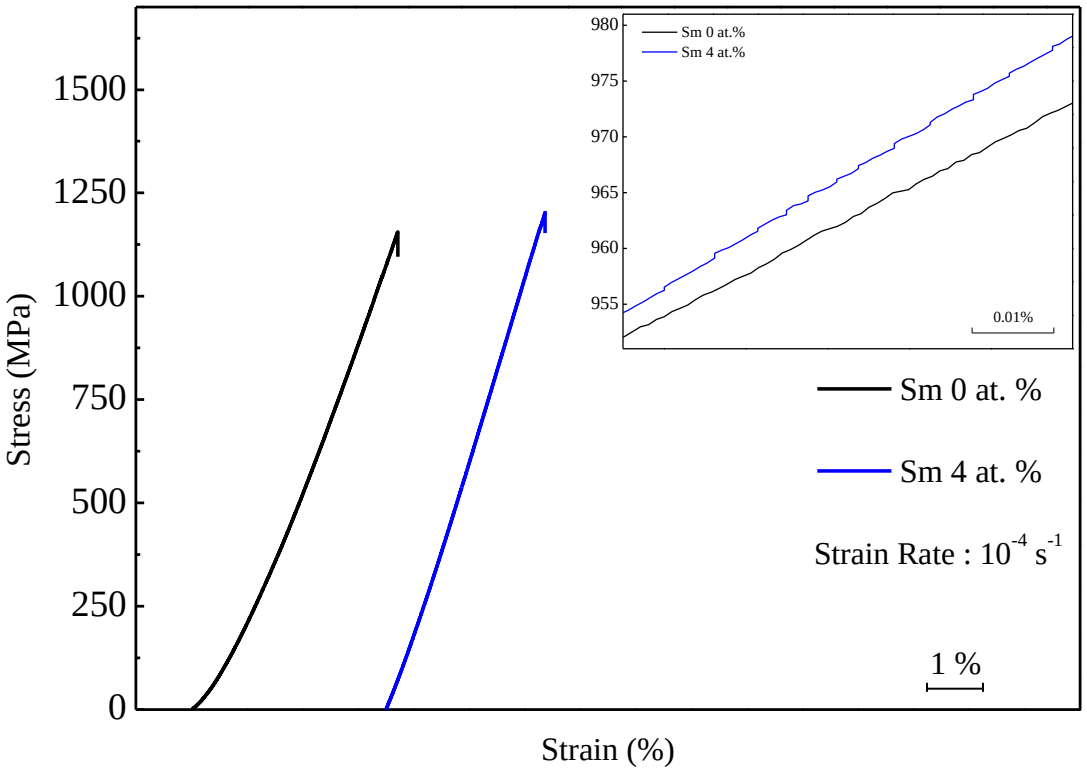

Figure 4. 8 Compressive stress-strain curves for 3 mm diameter suction cast rods of $Zr_{50}Cu_{40}Al_{10}$ and $(Zr_{50}Cu_{40}Al_{10})_{96}Sm_4$ under 10^{-4} s^{-1} strain rate. Inset depicts magnified scale to illustrate serrated behavior of stress-strain curves.

Mechanical tests were carried out via quasi-static uniaxial compression tests at 10^{-4} s^{-1} s on 3 mm diameter suction cast $Zr_{50}Cu_{40}Al_{10}$ and $(Zr_{50}Cu_{40}Al_{10})_{96}Sm_4$ specimens. Stress-strain curves plotted in Fig. 4.8 revealing a straight elastic deformation region which ends with a sudden fracture at approximately 1.2 GPa for both Sm free and Sm micro alloyed $Zr_{50}Cu_{40}Al_{10}$ samples. Detailed investigation in inset of Fig. 4.8 revealed serrated behavior of stress-strain curves indicating plastic deformation occurs via discrete strain burst events of stick and slip mechanism. These strain burst events are much more apparent in $(Zr_{50}Cu_{40}Al_{10})_{96}Sm_4$ composition showing deformation mainly occurs by rapid nucleation and propagation of few shear bands. Vaguer and fewer serrations in stress-strain curve of $Zr_{50}Cu_{40}Al_{10}$ composition shows more homogenous deformation for this sample. It is important to note that none of these samples are fully amorphous, in fact, even their crystalline fractions might greatly differ from each other. So, their fracture strengths, plastic limits or deformation behaviors may not be representing real material properties. These should be considered during any further discussion. However, after conducting these experiments it is thought that results may give some insight on later results with fully amorphous samples.

Fracture surface analysis were carried out using SEM. Fracture micrographs of 1 and 3 mm diameter suction cast $Zr_{50}Cu_{40}Al_{10}$ and $(Zr_{50}Cu_{40}Al_{10})_{96}Sm_4$ samples are shown in Fig. 4.9. Vein patterns and liquid-like ductile features are observed in fracture surfaces of 3 mm cast rod in Fig. 4.9 (a, b) and 1 mm cast rod in Fig. 4.9 (c, d) revealing a more homogenous plastic deformation type where multiple shear bands are branched over the fracture surface and shear band propagation speed is lower. On the other hand, $(Zr_{50}Cu_{40}Al_{10})_{96}Sm_4$ sample undergoes fragmentation during loading similar to an extremely brittle metallic glass as explained in Chapter 2. On the contrary to Sm free sample, smooth surfaces with few shear band marks are observed in fracture surfaces of $(Zr_{50}Cu_{40}Al_{10})_{96}Sm_4$ fragments indicating a rapid propagation of a main shear band. Vein patterns are generally attributing to a higher plasticity during fracture. Strain until fracture, which is the sum of both elastic and any plastic deformation, for $Zr_{50}Cu_{40}Al_{10}$ and $(Zr_{50}Cu_{40}Al_{10})_{96}Sm_4$ alloys in Fig. 4.8 are roughly 3.8 % and 2.8 % respectively. Sm addition on partially crystalline samples up to 4 at. % resulted in embrittlement.

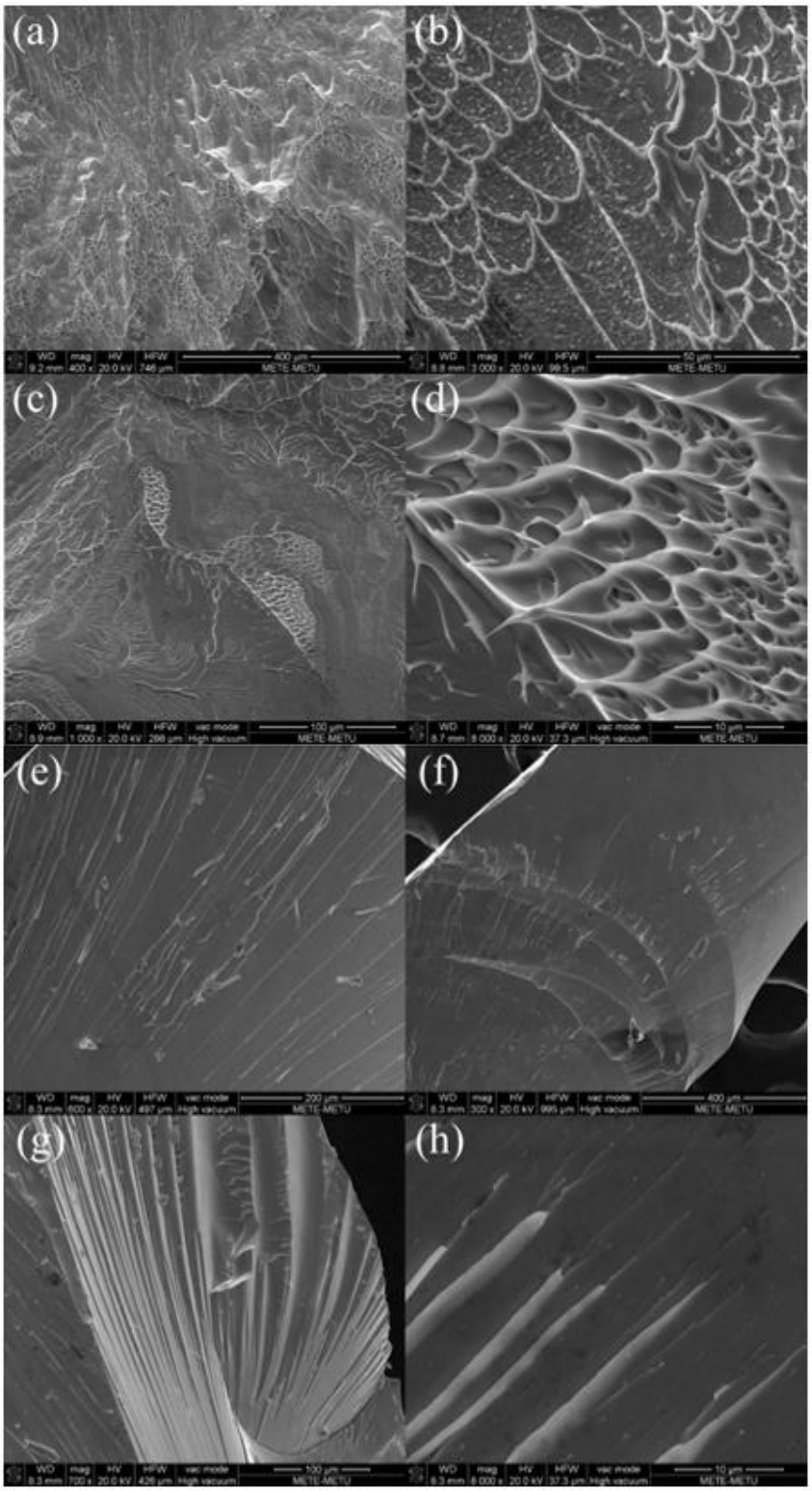

Figure 4. 9 Fracture micrographs for (a, b) 3 mm diameter and (c, d) 1 mm diameter $Zr_{50}Cu_{40}Al_{10}$ rods and for (e, f, g, h) 3 mm diameter $(Zr_{50}Cu_{40}Al_{10})_{96}Sm_4$ rods.

Hardness of fully amorphous ribbon specimens of $(Zr_{50}Cu_{40}Al_{10})_{100-x}Sm_x$ (x=0, 2, 4 at. %) were also investigated at nanoscale via nano indentation experiments. Nanoscale hardness values with respect to at. % Sm addition and annealing condition are shown in Fig. 4.10. Nano indentation hardness results are in good agreement with Vickers micro-hardness results to indicate that there is a decreasing trend in hardness with increasing Sm content up to 4 at. % Sm. Hardness profiles also show that with increasing indentation depth from 500 nm to 2000 nm there is an evident decrease in observed hardness. Indentation size effect (ISE) is also evident in fully amorphous ribbon samples. Softening is more pronounced between 500-1000 nm and gets more obscure with further increase in indentation depth. Measured nano indentation hardness and standard deviations of all samples are tabulated in Table 4.2.

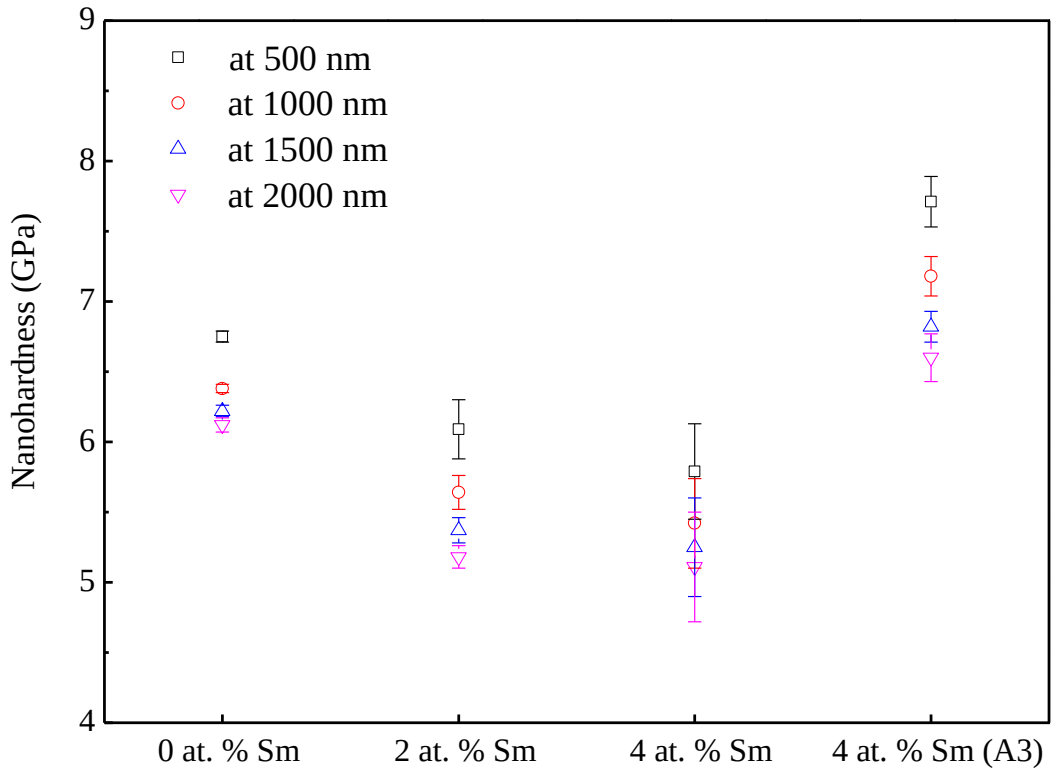

Figure 4. 10 Nano indentation hardness results of as-spun $(Zr_{50}Cu_{40}Al_{10})_{100-x}Sm_x$ (x=0, 2, 4 at. %) along with A3 condition of $(Zr_{50}Cu_{40}Al_{10})_{96}Sm_4$ ribbon samples at various indentation depths.

Table 4. 2 Nano indentation hardness results of melt-spun ribbons of $(Zr_{50}Cu_{40}Al_{10})_{100-x}Sm_x$ (x=0, 2, 4 at. %) along with A3 condition of $(Zr_{50}Cu_{40}Al_{10})_{96}Sm_4$ ribbon samples at various indentation depths.

	Hardness (GPa)			
Depth (nm)	**0 at. % Sm**	**2 at. % Sm**	**4 at. % Sm**	**4 at. % Sm (A3)**
500	6.75 ± 0.04	6.09 ± 0.21	5.79 ± 0.34	7.71 ± 0.18
1000	6.38 ± 0.03	5.64 ± 0.12	5.42 ± 0.32	7.18 ± 0.14
1500	6.22 ± 0.04	5.37 ± 0.09	5.25 ± 0.35	6.82 ± 0.11
2000	6.12 ± 0.05	5.18 ± 0.08	5.11 ± 0.39	6.60 ± 0.17

Table 4.2 shows that hardness of $(Zr_{50}Cu_{40}Al_{10})_{100-x}Sm_x$ (x=0, 2, 4 at. %) melt-spun ribbon samples are decreasing from 6.75-6.12 GPa down to 6.09-5.18 GPa with 2 at. % Sm and then continued to decrease to 5.79-5.11 GPa with 4 at. % Sm addition. Nano indentation hardness results came to the same conclusion with Vickers micro-hardness results as shown in Table 4.2. Decrease in hardness of $Zr_{50}Cu_{40}Al_{10}$ alloy system with Sm micro alloying was proved once more by using fully amorphous melt-spun ribbons.

Another important point in Fig. 4.10 and Table 4.2 is the relatively higher hardness value (7.71-6.60 GPa) of $(Zr_{50}Cu_{40}Al_{10})_{96}Sm_4$ sample at A3 condition which is isothermally annealed at 703 K (430 ^oC) for 26 minutes (annealed until end of the isothermal crystallization peak). As mentioned earlier in Chapter 3, isothermal annealing at 703 K on $(Zr_{50}Cu_{40}Al_{10})_{96}Sm_4$ composition introduces spherical Cu_2Sm nanocrystals with 5-10 nm diameter. Nanocrystals cannot grow further due to the lack of available Sm atoms in matrix and the crystallization of the alloy is forced to cease resulting in a nanocrystalline reinforced amorphous matrix composite structure. Higher hardness value is tougth to be the projection of this composite structure. Nanocrystals embedded within amorphous matrix tend to trigger a strenghtening mechanism similar to precipitation hardening, enhancing hardness value at both nano and micro scale. Considering these results, it is expected that isothermally annealed $(Zr_{50}Cu_{40}Al_{10})_{96}Sm_4$ composition to have promising strength as well.

Compressive strengths of the samples were investigated via load controlled uniaxial micropillar compression tests with quasi-static strain rate of 10^{-4} s^{-1} with a plat punch integrated to the nanoindenter machine. All samples are prepared as micropillars with 3 μm diameter in FIB prior to testing since it was not possible to perform any mechanical tests other than hardness test to ribbon samples. Compressive stress-strain curves of $Zr_{50}Cu_{40}Al_{10}$ and $(Zr_{50}Cu_{40}Al_{10})_{96}Sm_4$ along with annealed (A3) condition of $(Zr_{50}Cu_{40}Al_{10})_{96}Sm_4$ are given in Fig. 4.11. It is clear that there is a pronounced size effect since fracture strength of all samples are relatively higher compared to their macro scale counterparts with 3 mm diameter. This size effect will be discussed later in this Chapter. One important point in Fig. 4.11 is that fracture strength of fully amorphous melt-spun $Zr_{50}Cu_{40}Al_{10}$ and $(Zr_{50}Cu_{40}Al_{10})_{96}Sm_4$ are very close to each other, while a slight decrease in fracture strength with 4 at. % Sm addition is observed. Meanwhile annealed $(Zr_{50}Cu_{40}Al_{10})_{96}Sm_4$ (A3) sample have a much higher fracture strength revealing the effect of annealing induced nanocrystals in amorphous matrix. Another important aspect of stress-strain curves in Fig. 4.11 are their serrated flow; for both as-spun $Zr_{50}Cu_{40}Al_{10}$ and $(Zr_{50}Cu_{40}Al_{10})_{96}Sm_4$ samples there are about 6-7 strain burst events where strength remains constant due to load control. These strain burst events are representing an event of shear band nucleation and propagation or an already present shear band growth. Considering these curves, it is plausible to state that multiple shear bands nucleate and propagate with further loading until fracture. One should note that in these micropillar compression experiments final shear band burst does not represent the ductility directly. In micropillar compression experiments ductility is attributed to the amount of shear bands that are nucleated and arrested [96, 105]. Since each strain burst represents an event of plastic deformation by shearing and each arrest represents a stop to catastrophic failure, alloy with many and short strain burst events can be considered as a more ductile sample. In the light of this information, although annealed $(Zr_{50}Cu_{40}Al_{10})_{96}Sm_4$ (A3) sample have a much higher fracture strength it fails via one dominant shear band which propagates very rapidly. In other words, fracture of this sample is rather catastrophic and in brittle manner. It is evident that same sample in as-spun condition shows more ductile behavior.

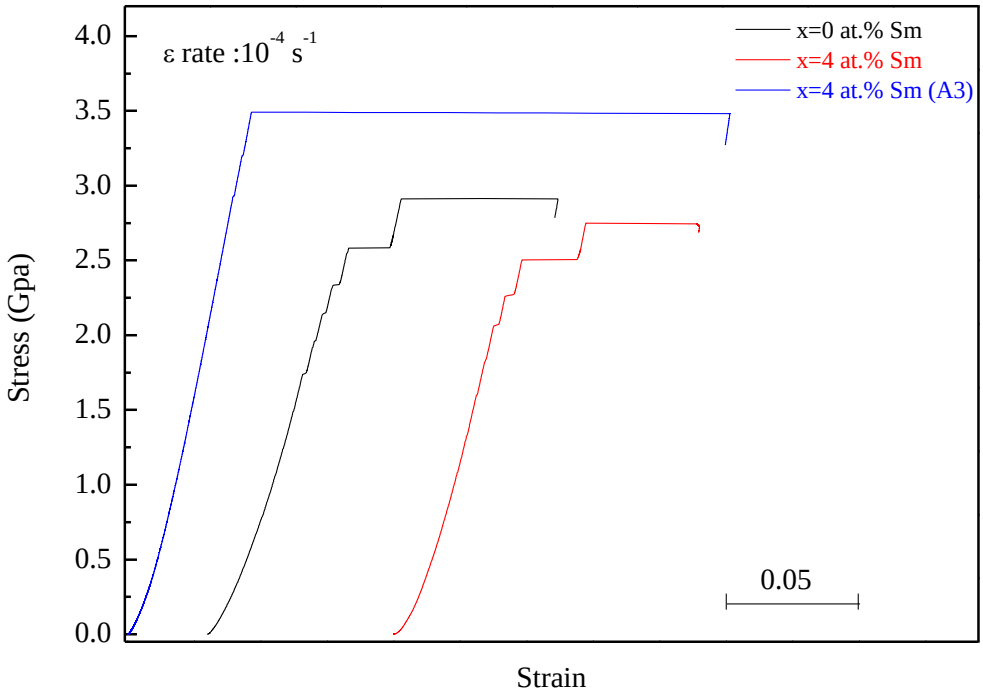

Figure 4. 11 Compressive stress-strain curves for as-spun conditions of $Zr_{50}Cu_{40}Al_{10}$ and $(Zr_{50}Cu_{40}Al_{10})_{96}Sm_4$ along with A3 condition of $(Zr_{50}Cu_{40}Al_{10})_{96}Sm_4$ 3 µm diameter micropillar samples under 10^{-4} s^{-1} strain rate.

Fracture morphologies of micropillars were investigated under SEM by tilting sample surfaces by 52° angle to observe dominant shear bands and shown in Fig. 4.12. SEM images of as-spun $Zr_{50}Cu_{40}Al_{10}$ and $(Zr_{50}Cu_{40}Al_{10})_{96}Sm_4$ compositions before and after loading are seen in Fig. 4.12 (a, b) and Fig 4.12 (c, d). Both micropillars have multiple shear bands which originate from top corner of the specimen and inclined with ~45° angle. Smaller branched shear bands are also observed which are in good correlation with multiple strain burst plateaus in stress-strain curves. Unlike previous pillars, annealed $(Zr_{50}Cu_{40}Al_{10})_{96}Sm_4$ sample deforms in a different manner. Main dominant shear band has a much longer displacement distance where deformed plane nearly moved out of the sample diameter indicating a larger shear band propagation speed. Considering SEM images in literature shown in Fig. 4.2, annealed $(Zr_{50}Cu_{40}Al_{10})_{96}Sm_4$ sample resembles a Mg-based BMG with some brittle fracture characteristics where deformation localizes on one dominant shear band.

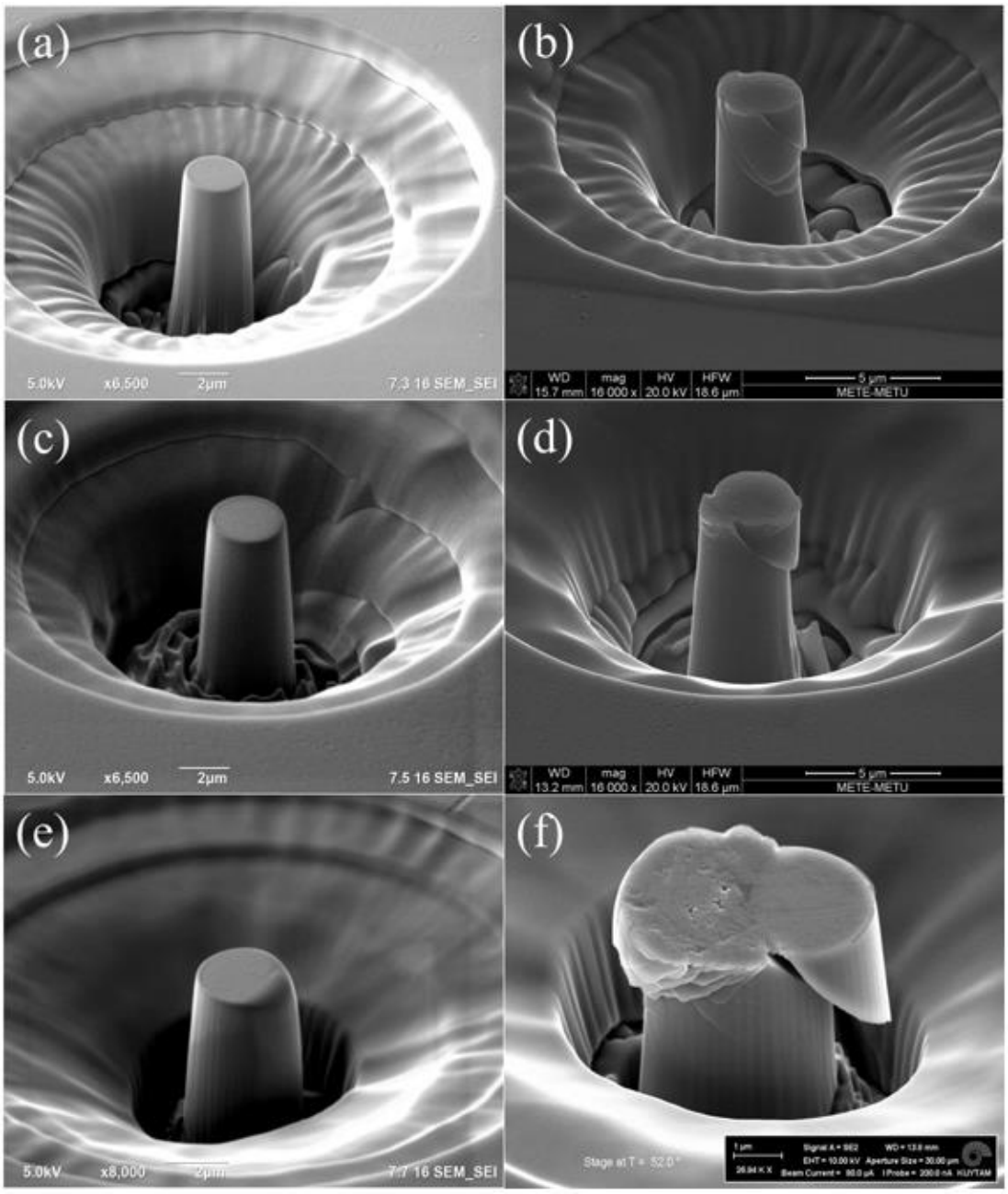

Figure 4. 12 SEM images of micropillars before and after deformation where (a, b) and (c, d) represents as-spun conditions of $Zr_{50}Cu_{40}Al_{10}$ and $(Zr_{50}Cu_{40}Al_{10})_{96}Sm_4$ respectively, while (e, f) represents condition A3 of $(Zr_{50}Cu_{40}Al_{10})_{96}Sm_4$.

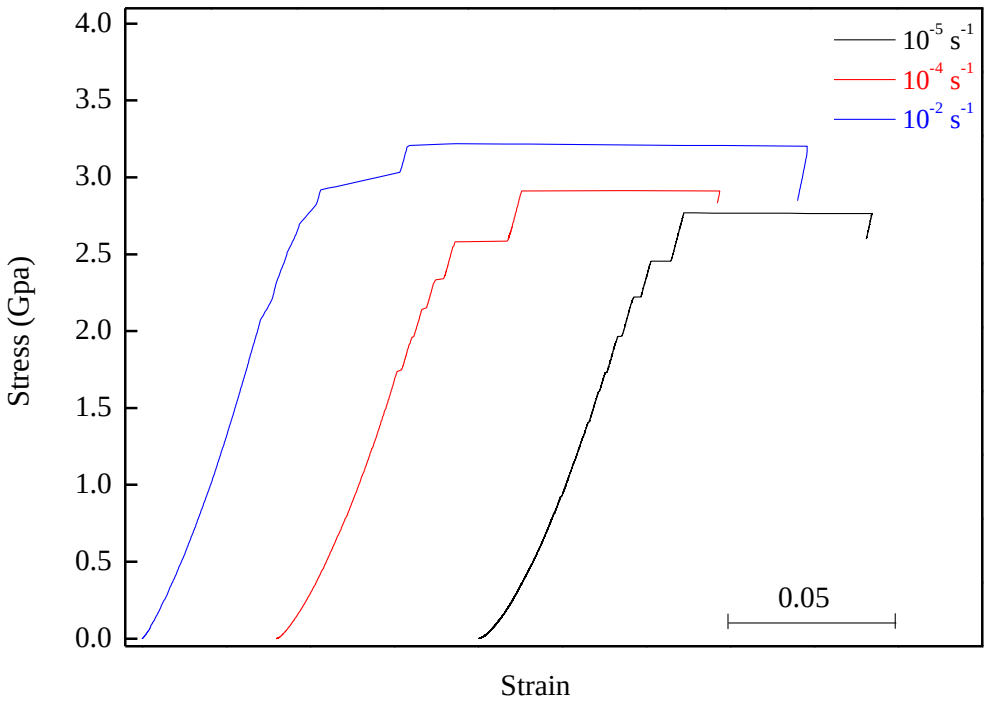

Figure 4. 13 Compressive stress-strain curves for 3 μm diameter $Zr_{50}Cu_{40}Al_{10}$ micropillar samples under various strain rates.

Compressive stress-strain curves of 3 μm diameter $Zr_{50}Cu_{40}Al_{10}$ micropillar samples under 10^{-5}, 10^{-4}, 10^{-2} s^{-1} strain rate are given in Fig. 4.11. Stress-strain curves for $Zr_{50}Cu_{40}Al_{10}$ micropillar under all strain rates show serrations; however, at highest strain rate, 10^{-2} s^{-1}, strain burst events become vaguer. Theoretically, in order to detect the strain burst events, the nano indenter cross-head speed should be relatively lower than shear band propagation speed [106]. It is plausible to expect that as strain rate increases, serrations in stress-strain curve will diminish at some point. Disappearance of strain burst plateaus in 10^{-2} s^{-1} rate is thought to be due to high cross-head speed, which does not allow observations of shear banding events. In addition, effect of strain rate on the fracture strength of metallic glasses were studied in literature. Although fracture strength is found to be independent of strain rate for most metallic glasses, there are some studies in literature reported that strain rate increase triggers an increase in fracture strength of Zr-based BMGs [20].

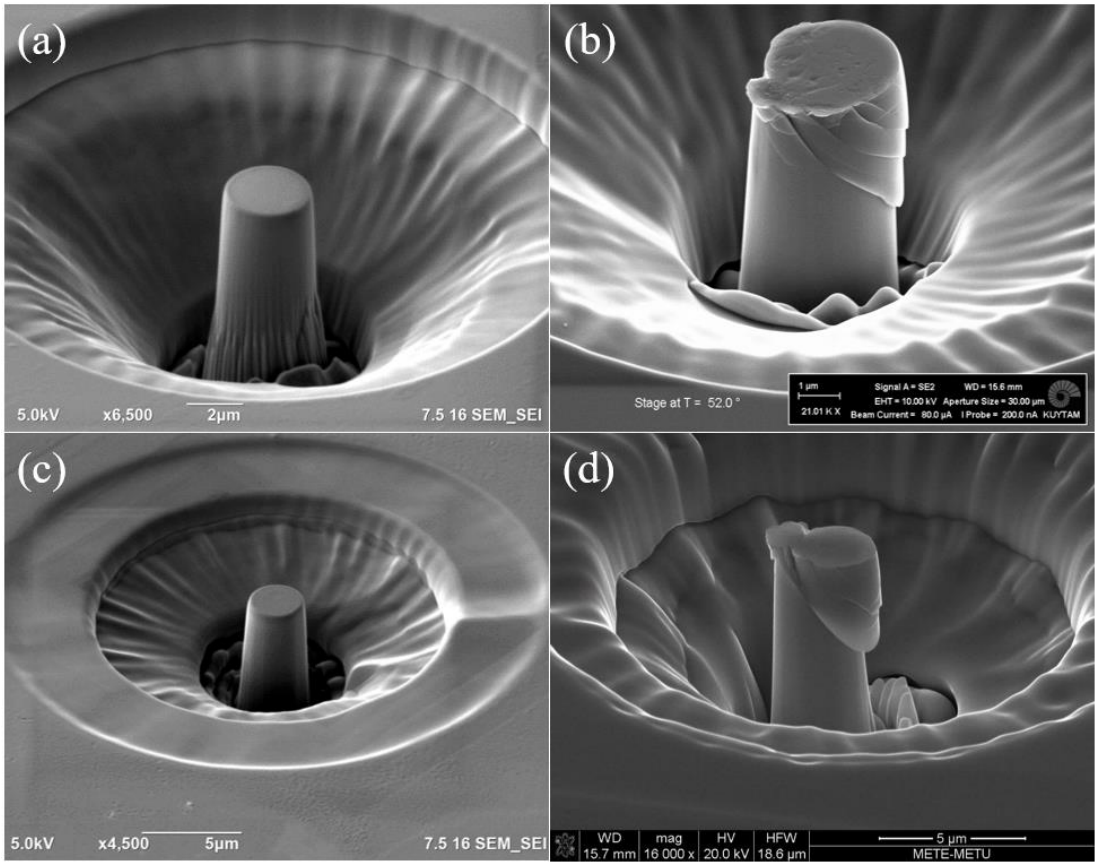

Figure 4. 14 SEM images of micropillars of $Zr_{50}Cu_{40}Al_{10}$ before and after deformation with corresponding strain rates; (a, b) 10^{-5} s^{-1} (c, d) 10^{-2} s^{-1}.

As shown in Fig. 4.13, our results showed a slight increase in fracture strength with increased strain rate. However, this slight increase may be due to geometrical aspects which are greatly affecting the results in micropillar compression tests. Thus our study for effect of strain rate on $Zr_{50}Cu_{40}Al_{10}$ micropillars can be considered as partly inconclusive. Fig. 4.14 shows the SEM images of $Zr_{50}Cu_{40}Al_{10}$ micropillars before and after deformation under 10^{-5} s^{-1} and 10^{-2} s^{-1} strain rates. Displacement range of 10^{-2} s^{-1} strain rate is higher as sheared off plane can be seen as extended out of sample diameter. However, number of observed shear bands are close to each other in both 10^{-5} and 10^{-2} s^{-1} strain rate condition. Although dominant main shear band is more pronounced, there are few other shear bands observed in 10^{-2} s^{-1} rate case.

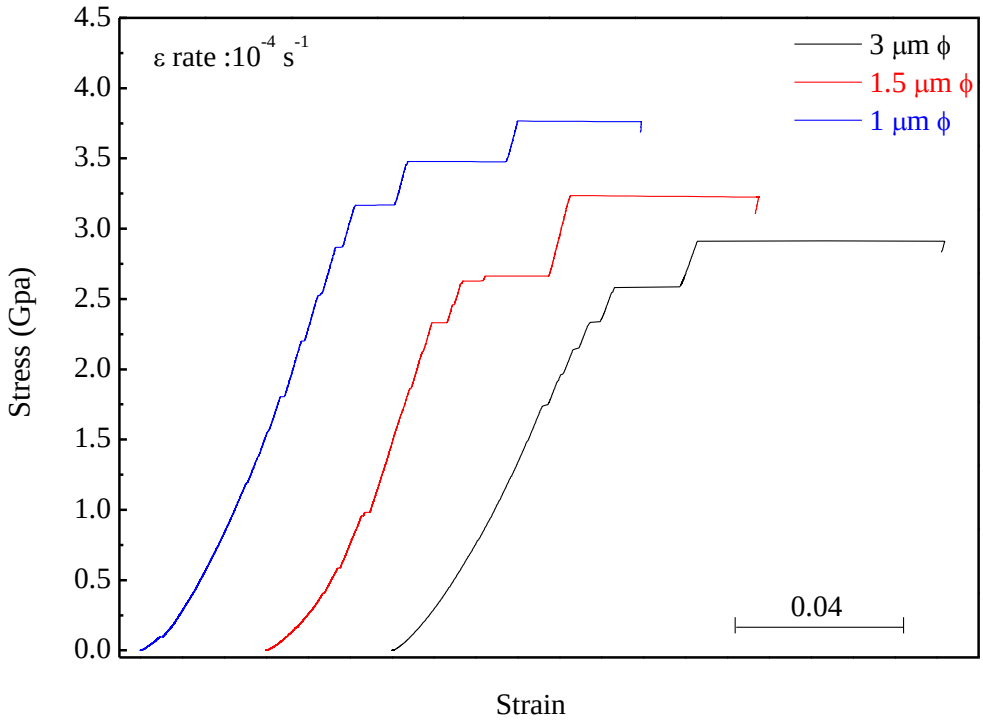

Figure 4. 15 Compressive stress-strain curves at 10^{-4} s^{-1} strain rate for $Zr_{50}Cu_{40}Al_{10}$ micropillar samples at corresponding sample diameters.

Compressive stress-strain curves of $Zr_{50}Cu_{40}Al_{10}$ micropillar samples under 10^{-4} s^{-1} strain rate for 3, 1.5 and 1 μm diameters are given in Fig. 4.15. It is seen that as sample size decreases from 3 μm to 1.5 μm and then 1 μm, fracture strength increases from 2.9 to 3.2 and then 3.7 GPa gradually. For all sample diameters, there are 6-7 strain burst events present. Considering these results, effect of sample size on fracture strength is in good correlation with the metallic glass phenomenon known as 'smaller is stronger' [99-100]. Number of strain burst events for all samples are approximately same indicating a similar deformation behavior. SEM images of 1.5 and 1 μm diameter micropillars before and after deformation are shown in Fig. 4.16. Both images reveal similar deformation mechanisms, where multiple shear bands are present. Both of these samples show relatively more ductile fracture characteristics compared to the 3 μm size pillar in Fig. 4.12 (a, b). Similarly, in Fig. 4.15, strain burst events for smaller size samples appear to be arrested at shorter strain intervals indicating a harder shear band propagation and lower shear band velocity.

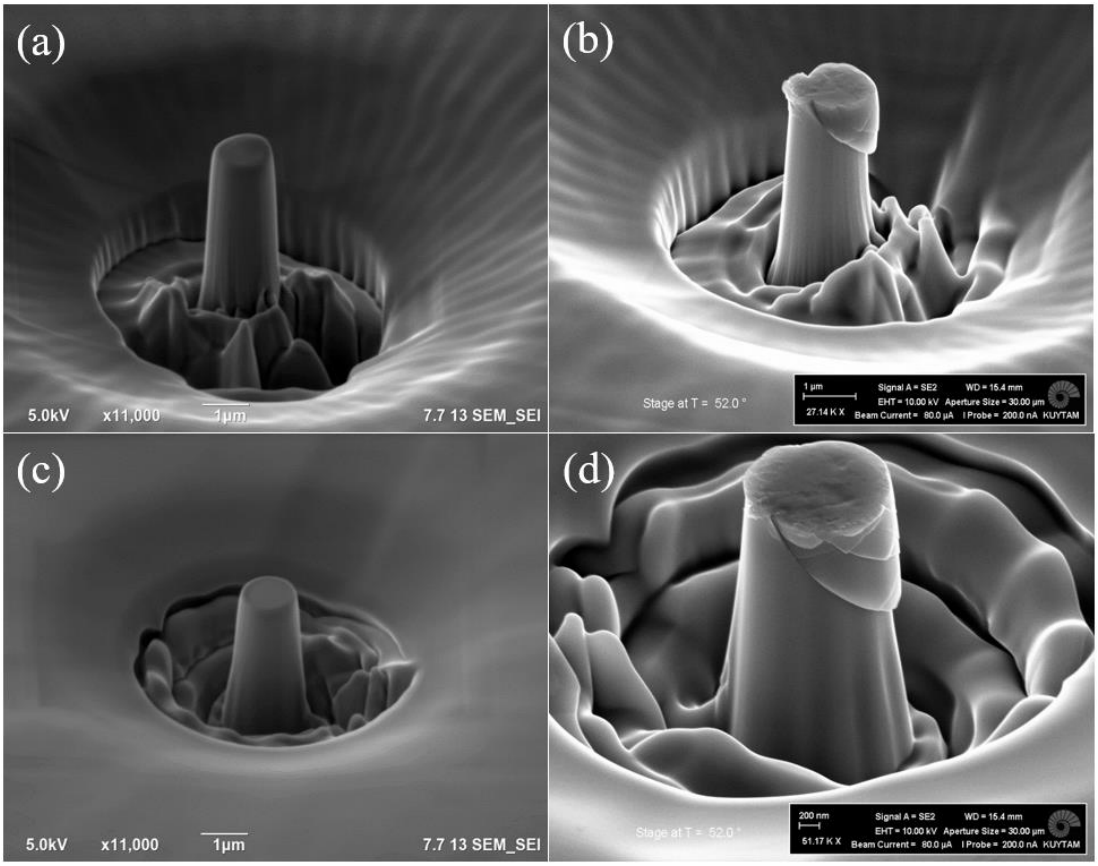

Figure 4. 16 SEM images of micropillars of $Zr_{50}Cu_{40}Al_{10}$ before and after deformation with corresponding sample diameters; (a, b) 1.5 µm (c, d) 1 µm.

Increase in fracture strength with decreased sample size is explained by Weibull statics in literature [105]. Weibull statics are used to determine probability of fracture and expected fracture strengths according to the flaw density in a given volume for brittle materials. In other words, predicting the fracture strength of a material with high flaw density to be lower than the material with low flaw density. Since, as the sample size decreases the expected amount of possible flaw density would decrease. Thus a gradual increase in strength with decreasing sample size can be explained by Weibull statics. Decreased flaw density can also be considered to explain high fracture strength values of micropillar specimens compared to prior macro scale compression experiments.

4.5. Conclusion

Mechanical properties and shear band stability of suction cast and melt spun $(Zr_{50}Cu_{40}Al_{10})_{100-x}Sm_x$ (x=0, 2, 4 at. %) alloys have been investigated using Vickers micro-hardness, uniaxial macro compression testing, nano indentation testing and uniaxial micropillar compression testing. Fracture morphologies were investigated under SEM. All composition samples are produced in both 1 mm diameter suction cast rods and melt-spun ribbon forms after preparing ingots in arc-melter from high purity elements of the systems. Vickers micro-hardness tests were performed on both cast rod and melt spun ribbon samples. Sm micro alloying up to 4 at. % Sm found to cause a decrease in Vickers micro-hardness of $(Zr_{50}Cu_{40}Al_{10})_{100-x}Sm_x$ alloys. Uniaxial macro compression tests were performed on 3 mm diameter partially crystalline suction cast rod samples of $Zr_{50}Cu_{40}Al_{10}$ and $(Zr_{50}Cu_{40}Al_{10})_{96}Sm_4$ compositions. Fracture strength of both Sm-free and 4 at. % Sm micro-alloyed samples were found to be close to each other; however, their fracture morphologies were extremely different. Fracture surface of $Zr_{50}Cu_{40}Al_{10}$ specimen was covered with vein patterns and liquid-like features, while $(Zr_{50}Cu_{40}Al_{10})_{96}Sm_4$ specimen undergoes fragmentation with a blast-like fracture during loading. Fracture surfaces of fragments were featureless and smooth where no liquid-like features were observed, indicating a rapid shear band growth where shear band propagation is unstable. Nano indentation experiments were performed on both as-spun conditions of $(Zr_{50}Cu_{40}Al_{10})_{100-x}Sm_x$ (x=0, 2, 4 at. %) specimens along with isothermally annealed condition (A3) of $(Zr_{50}Cu_{40}Al_{10})_{96}Sm_4$ specimen. Nano indentation hardness results were in correlation with Vickers hardness results. Decrease in hardness was observed with increased Sm content up to 4 at. %. However, hardness of annealed $(Zr_{50}Cu_{40}Al_{10})_{96}Sm_4$ specimen was found to be higher than all samples indicating the presence of nanocrystallization induced hardening in our samples. In addition, both Vickers hardness and nano indentation hardness decreased with increased indentation load or depth, revealing indentation size effect is present for $(Zr_{50}Cu_{40}Al_{10})_{100-x}Sm_x$ alloy system. Finally, uniaxial micropillar compression testing experiments were performed on 3 μm pillar size $Zr_{50}Cu_{40}Al_{10}$ and $(Zr_{50}Cu_{40}Al_{10})_{96}Sm_4$ specimens along with isothermally annealed $(Zr_{50}Cu_{40}Al_{10})_{96}Sm_4$

specimen at 10^{-4} s^{-1} rate. Micropillar compression results of as-spun $Zr_{50}Cu_{40}Al_{10}$ and $(Zr_{50}Cu_{40}Al_{10})_{96}Sm_4$ specimens showed that fracture strength slightly decreased with 4 at. % Sm alloying; however, significantly increased after isothermal annealing at 703 K for 26 minutes. Annealed $(Zr_{50}Cu_{40}Al_{10})_{96}Sm_4$ sample projected a higher fracture strength; however, it failed in a catastrophic manner where only one dominant shear band propagated rapidly during failure. Fracture morphologies of as-spun $Zr_{50}Cu_{40}Al_{10}$ and $(Zr_{50}Cu_{40}Al_{10})_{96}Sm_4$ compositions show that they fail via multiple shear bands and had low shearing displacement. Fracture morphology reveals a relatively ductile manner for these specimens compared to isothermally annealed $(Zr_{50}Cu_{40}Al_{10})_{96}Sm_4$ sample. Effect of sample size and strain rate are also investigated using 3, 1.5 and 1 μm diameter $Zr_{50}Cu_{40}Al_{10}$ micropillars. Gradual increase in fracture strength with decreased sample size was observed which was thought to be originated from Weibull statics. Slight increase fracture strengths and disappearance of serrations in stress-strain curves with increased strain rate was also observed. Vaguer serrations were explained by increased velocity of cross-head speed which is thought to be faster than shear band propagation speed. Although serrations were less at high strain rates, fracture surface contained multiple shear bands on SEM image.

In summary, Cu_2Sm nanocrystal reinforced amorphous matrix composite structure have improved hardness and strength compared to both Sm-free and Sm alloyed fully amorphous samples. However, shear band stability of composite structure appears to be extremely unstable. Fracture mechanism of Cu_2Sm nanocrystal containing samples appear to be similar to extremely brittle metallic glasses such as Mg-based BMGs. Such rapid propagation of shear bands is thought to be due to shear band and nanocrystal interactions, but further study requires in order to explain the mechanism.

CHAPTER 5

CONCLUSION AND FUTURE RECOMMENDATIONS

5.1. Conclusions

Effect of Sm microalloying on the glass forming ability, thermal properties, phase selection and crystallization kinetics along with mechanical properties at nano to macro scale for $(Zr_{50}Cu_{40}Al_{10})_{100-x}Sm_x$ (x= 0-4 at. %) bulk amorphous metallic alloys were investigated within the scope of this thesis.

The effect of Sm microalloying on the glass forming ability and mechanical properties of Cu-Zr-Al bulk metallic glasses have been investigated using DSC, XRD, SEM and mechanical testing on 1, 2, 3 mm diameter cast rods in the first part of the study. Sm addition lead to an increase in GFA for $Zr_{50}Cu_{40}Al_{10}$ alloy according to XRD; however, fully amorphous samples could not have achieved. Furthermore, increase in the Sm concentration of the alloys resulted in a decrease of ΔT_x, which represents the thermal stability of the amorphous phase. The mechanical tests showed no clear trend that can be concluded due to partially crystalline nature of the samples. However, it is clear that $(Zr_{50}Cu_{40}Al_{10})_{96}Sm_4$ alloy show the highest fracture strength which is contributed to higher amorphous portion. In addition, mechanical tests indicated that $(Zr_{50}Cu_{40}Al_{10})_{96}Sm_4$ alloy failed with fragmentation fracture mode instead of shear fracture mode that is observed for most Zr-based metallic glasses.

In the second part of the study, results in Chapter 2 concerning GFA and ΔT_x are proven using fully amorphous melt spun ribbon samples. Furthermore, effect of Sm micro alloying on crystallization kinetics and phase selection was investigated via KAS and FWO methods. Sm addition found to increase crystallization activation energy for $Cu_{10}Zr_7$ which is the first crystallizing phase for Sm free alloys. Increase in activation energy and change in phase selection are correlated and discussed.

$(Zr_{50}Cu_{40}Al_{10})_{96}Sm_4$ alloy was investigated further via combined study of isothermal DSC, XRD, TEM and APT experiments using both 1, 2, 3 mm diameter suction cast rods and melt spun ribbons. In case of 1 mm rod samples microstructure contained 30 nm large Cu_2Sm nanocrystals in as-cast state, while melt spun ribbons were fully amorphous. According to TEM and APT analysis, Sm addition up to 4 at. % lead to nanocrystallization of 5-10 nm spherical Cu_2Sm phase prior to $Cu_{10}Zr_7$ crystallization for both cast rod and ribbon samples. Further growth of Cu_2Sm phase was thought to be hindered due to solute pile-up of Zr atoms at phase boundary and insufficiency of Sm atoms in amorphous phase.

In the last part of the study, mechanical properties and shear band stability of both 1 mm diameter cast rods and melt spun ribbons were investigated with respect to Sm content via SEM and micro and macro scale experiments such as Vickers hardness, uniaxial macro compression tests, nano indentation and micropillar compression experiments. Alloying up to 4 at. % Sm found to cause a decrease in both Vickers micro-hardness and nano indentation hardness of Zr-Cu-Al BMGs. Fracture strength of both 3 mm cast rod specimens of Sm-free and 4 at. % Sm micro alloyed samples were found to be similar; however, their fracture modes varied. Similar to findings in Chapter 2, $(Zr_{50}Cu_{40}Al_{10})_{96}Sm_4$ failed with fragmentation mode. Micropillar compression tests showed fracture strength slightly decreased with 4 at. % Sm alloying and significantly increased after annealing introduced nanocrystals. All samples contained multiple branched shear bands in fracture surface in SEM analysis. Although nanocrystalline $(Zr_{50}Cu_{40}Al_{10})_{96}Sm_4$ alloy showed higher strength it failed via one dominant rapidly propagating shear band revealing brittle characteristics. Effect of sample size and strain rate are also investigated and discussed.

5.2. Future Recommendations

Effect of rare-earth elements, namely Sm, on Cu-Zr-Al bulk metallic glasses were investigated in terms of producibility, thermal, kinetic and mechanical properties and phase selection within the scope of this thesis. Numerous studies in literature showed that alloying rare-earth elements alter both structural integrity and mechanical characteristics for Zr-based bulk metallic glasses. Effect of rare-earth elements on structure is explained as phase separation of Zr-rich and RE-rich amorphous phase; however, critical compositions for each element or mechanisms for phase separation is still not clear. On the other hand, investigation of mechanical properties of Zr-rich metallic glasses with rare-earth alloying shows some vague trends of minor increase in ductility followed by major embrittlement regarding few studies in literature. Understanding origins of these trends and shifts in mechanical properties is an unsettled topic. Generally, positive enthalpy of mixing between rare-earth elements and Zr is considered to be the main reason why any structural and mechanical change occurs. However, effects of this immiscibility tendency on different systems still remain unknown and may show different results such as nanocrystallization instead of phase separation as illustrated in this thesis.

Most crucial future study should be regarding nanocrystallization behavior of Sm micro alloyed $Zr_{50}Cu_{40}Al_{10}$ alloys shown in Chapter 3. Whether system undergoes some nano scale phase separation prior to nanocrystallization or not should be examined by state of the art characterization techniques such as atom probe tomography and in-situ heating transmission electron microscopy experiments. Although APT was used to investigate nanocrystals in Chapter 3, no further study was conducted due to time and financial limitations. Further APT analysis should be conducted on earlier stages of nanocrystallization in order to detect any sign of phase separation. Similarly, in-situ heating TEM experiments are at utmost importance to be able to monitor structural changes during annealing. Nanocrystal number is shown to be approximately 50 nanocrystals in 70x70x70 nm^3 volume which corresponds to 10^{23} m^{-3} nanocrystal density. Origins of such high nanocrystal density should be addressed

by further research for it may prove useful in understanding crystallization phenomenon in purely scientific basis. Phase separation prior to nanocrystallization may be one of the reasons of this absurdly high nucleation rate.

Another future study can be investigation of the effect of cooling rate on the nucleation rate. This study may also prove useful in order to understand the mechanism and origin of these nanocrystals. Although, cooling rate effect is somewhat investigated in Chapter 3 using suction cast rods and melt spun ribbons, scientific concerns were different. Fully amorphous sputtered films of $(Zr_{50}Cu_{40}Al_{10})_{96}Sm_4$ composition can be compared to melt spun ribbons in terms of crystallization behaviors and nanocrystal density to be able to comment on effects of cooling rate.

Investigation of liquid state amorphous phase is also quite important to make correlations of amorphous structures in liquid and solid state and understanding possible phase separation event. Research concerning liquid state was already initiated. In order to examine this, synchrotron radiation was used in combination of aerodynamic levitation melting setup. Levitating samples of a different compositions, $Zr_{50-x}Cu_{40}Al_{10}Sm_x$ (x=10, 20, 30) were melted with laser to obtain containerless liquidation. High energy synchrotron radiation is applied on molten samples to collect XRD data to investigate amorphous structure in liquid state. Results of levitation melting experiments were not presented within this thesis; however, evaluation of liquid state can also shed light on structural effects of Sm and high nanocrystallization density of Cu-Zr-Al-Sm bulk metallic glasses.

Last but not least, one of the most important future study should be investigation of shear bands and nanocrystals of $(Zr_{50}Cu_{40}Al_{10})_{96}Sm_4$ alloy during deformation. Such research can help explain the peculiar fracture mode of nanocrystalline/amorphous composite $(Zr_{50}Cu_{40}Al_{10})_{96}Sm_4$ alloy. In order to reveal origins of fragmentation failure and understand shear band/nanocrystal interactions, in-situ nano mechanical TEM experiments can be conducted on both fully amorphous and annealed samples. Real time examination of shear band propagation and the role of the nanocrystals during deformation can give insight on mechanical properties of metallic glasses.

REFERENCES

[1] J. D. Clark, “The Middle Stone Age of East Africa and the Beginnings of Regional Identity,” *J. World Prehistory*, vol. 2, no. 3, pp. 235–305, 1988.

[2] R. Torrence, P. Swadling, N. Kononenko, W. R. Ambrose, P. Rath, and M. D. Glascock, “Mid-Holocene Social Interaction in Melanesia: New Evidence from Hammer-Dressed Obsidian Stemmed Tools,” *Asian Perspect.*, vol. 48, no. 1, pp. 119–148, 2009.

[3] J. E. Kogel, “A look at the history of mining : Two Peabody mines reach safety mark ; Pair of mines hit one million hours without a lost time incident,” *Min. Eng.*, 2013.

[4] W. Klement, R. H. Willens, and P. O. L. Duwez, “Non-crystalline Structure in Solidified Gold-Silicon Alloys,” *Nature*, vol. 187, no. 4740, pp. 869–870, Sep. 1960.

[5] A. Inoue, “Stabilization of metallic supercooled liquid and bulk amorphous alloys,” *Acta Mater.*, vol. 48, no. 1, pp. 279–306, 2000.

[6] D. Turnbull, “Metastable structures in metallurgy,” *Metall. Trans. B*, vol. 12, no. 2, pp. 217–230, 1981.

[7] J. F. Löffler, “Bulk metallic glasses,” *Intermetallics*, vol. 11, no. 6, pp. 529–540, 2003.

[8] A. Inoue, “Amorphous, Nanoquasicrystalline and Nanocrystalline Alloys in Al-based Systems,” *Prog. Mater. Sci.*, vol. 43, no. 5, pp. 365–520, 1998.

[9] M. Miller and P. Liaw, *Bulk Metallic Glasses An Overview*. 2008.

[10] C. T. Liu *et al.*, “Test environments and mechanical properties of Zr-base bulk amorphous alloys,” *Metall. Mater. Trans. A*, vol. 29, no. 7, pp. 1811–1820, 1998.

[11] C. Zhang, L. Liu, K. C. Chan, Q. Chen, and C. Y. Tang, “Wear behavior of HVOF-sprayed Fe-based amorphous coatings,” *Intermetallics*, vol. 29, pp. 80–

85, 2012.

[12] M. Miglierini and I. Škorvánek, “Magnetic study of neutron irradiated FeCrSiB metallic glass,” *Mater. Sci. Eng. A*, vol. 147, no. 1, pp. 101–106, Oct. 1991.

[13] M. Telford, “The case for bulk metallic glass,” *Mater. Today*, no. March, pp. 36–43, 2004.

[14] Z. P. Lu and C. T. Liu, “A new glass forming-forming ability criterion for bulk metallic glasses,” *Acta Mater.*, vol. 50, pp. 3501–3512, 2002.

[15] Z. Y. Suo, K. Q. Qiu, Q. F. Li, J. H. You, Y. L. Ren, and Z. Q. Hu, “A new parameter to evaluate the glass-forming ability of bulk metallic glasses,” *Mater. Sci. Eng. A*, vol. 528, no. 1, pp. 429–433, 2010.

[16] R. Busch, “The thermophysical properties of bulk metallic glass-forming liquids,” *Jom*, vol. 52, no. 7, pp. 39–42, 2000.

[17] C. Suryanarayana and A. Inoue, *Bulk Metallic Glasses*. CRC Press, 2010.

[18] E. R. Homer and C. A. Schuh, “Mesoscale modeling of amorphous metals by shear transformation zone dynamics,” *Acta Mater.*, vol. 57, no. 9, pp. 2823–2833, 2009.

[19] A. . Argon, “Plastic deformation in metallic glasses,” *Acta Metall.*, vol. 27, no. 1, pp. 47–58, Jan. 1979.

[20] C. A. Schuh, T. C. Hufnagel, and U. Ramamurty, “Mechanical behavior of amorphous alloys,” *Acta Mater.*, vol. 55, no. 12, pp. 4067–4109, 2007.

[21] C. A. Schuh *et al.*, “Rate Dependence of Serrated Flow During Nanoindentation of a Bulk Metallic Glass,” *J. Mater. Res.*, vol. 17, no. 7, pp. 1651–1654, 2002.

[22] H. Neuhäuser, “Rate of shear band formation in metallic glasses,” *Scr. Metall.*, vol. 12, no. 5, pp. 471–474, 1978.

[23] S. X. Song and T. G. Nieh, “Direct measurements of shear band propagation in metallic glasses - An overview,” *Intermetallics*, vol. 19, no. 12, pp. 1968–1977, 2011.

[24] D. Klaumünzer, A. Lazarev, R. Maass, F. H. Dalla Torre, A. Vinogradov, and

J. F. Löffler, “Probing shear-band initiation in metallic glasses,” *Phys. Rev. Lett.*, vol. 107, no. 18, pp. 1–5, 2011.

[25] T. C. Hufnagel, T. Jiao, Y. Li, L.-Q. Xing, and K. T. Ramesh, “Deformation and Failure of Zr57Ti5Cu20Ni8Al10 Bulk Metallic Glass Under Quasi-static and Dynamic Compression,” *J. Mater. Res.*, vol. 17, pp. 1441–1445, 2002.

[26] B. Yang, C. T. Liu, T. G. Nieh, M. L. Morrison, P. K. Liaw, and R. a. Buchanan, “Localized heating and fracture criterion for bulk metallic glasses,” *J. Mater. Res.*, vol. 21, pp. 915–922, 2006.

[27] J. J. Lewandowski and A. L. Greer, “Temperature rise at shear bands in metallic glasses,” *Nat. Mater.*, vol. 5, no. 1, pp. 15–18, 2006.

[28] B. A. Sun, J. Tan, S. Pauly, U. Kühn, and J. Eckert, “Stable fracture of a malleable Zr-based bulk metallic glass,” *J. Appl. Phys.*, vol. 112, no. 10, pp. 5–11, 2012.

[29] Z. F. Zhang and J. Eckert, “Unified tensile fracture criterion,” *Phys. Rev. Lett.*, vol. 94, no. 9, pp. 1–4, 2005.

[30] Y. Chen, M. Q. Jiang, Y. J. Wei, and L. H. Dai, “Failure criterion for metallic glasses,” *Philos. Mag.*, vol. 91, no. 36, pp. 4536–4554, 2011.

[31] T. Mukai, T. G. Nieh, Y. Kawamura, A. Inoue, and K. Higashi, “Effect of strain rate on compressive behavior of a Pd40Ni40P20 bulk metallic glass,” *Intermetallics*, vol. 10, no. 11–12, pp. 1071–1077, 2002.

[32] Z. F. Zhang *et al.*, “Wavy cleavage fracture of bulk metallic glass,” *Appl. Phys. Lett.*, vol. 89, no. 25, pp. 105–108, 2006.

[33] G. Wang, K. C. Chan, X. H. Xu, and W. H. Wang, “Instability of crack propagation in brittle bulk metallic glass,” *Acta Mater.*, vol. 56, no. 19, pp. 5845–5860, 2008.

[34] K. Zhao, X. X. Xia, H. Y. Bai, D. Q. Zhao, and W. H. Wang, “Room temperature homogeneous flow in a bulk metallic glass with low glass transition temperature,” *Appl. Phys. Lett.*, vol. 98, no. 14, pp. 8–11, 2011.

[35] M. Stoica, J. Eckert, S. Roth, Z. F. Zhang, L. Schultz, and W. H. Wang, “Mechanical behavior of Fe65.5Cr4Mo4Ga4P12C5B5.5 bulk metallic glass,”

Intermetallics, vol. 13, no. 7, pp. 764–769, 2005.

[36] Z. F. Zhang, H. Zhangy, B. L. Shenz, A. Inouez, and J. Eckertx, "Shear fracture and fragmentation mechanisms of bulk metallic glasses," *Philos. Mag. Lett.*, vol. 86, no. 10, pp. 643–650, 2006.

[37] A. Laboratory, "Melt Spinner," 2009. [Online]. Available: https://www.flickr.com/photos/ames_laboratory/3292950517. [Accessed: 01-Jan-2017].

[38] F. X. Liu *et al.*, "Micro-scratch study of a magnetron-sputtered Zr-based metallic-glass film," *Surf. Coatings Technol.*, vol. 203, no. 22, pp. 3480–3484, 2009.

[39] J. P. Chu *et al.*, "Thin film metallic glasses: Unique properties and potential applications," *Thin Solid Films*, vol. 520, no. 16, pp. 5097–5122, 2012.

[40] P. . J. Kelly and R. . D. Arnell, "Magnetron sputtering: a review of recent developments and applications," *Vacuum*, vol. 56, no. 3, pp. 159–172, 2000.

[41] H. Shao *et al.*, "High density of shear bands and enhanced free volume induced in Zr70Cu20Ni10 metallic glass by high-energy ball milling," *J. Alloys Compd.*, vol. 548, pp. 77–81, 2013.

[42] K. Tomolya *et al.*, "Microstructure evolution in CuZrAl alloys during ball-milling," *J. Non. Cryst. Solids*, vol. 382, pp. 105–111, 2013.

[43] H. K. D. H. Bhadeshia, "Differential scanning calorimetry," *Life Sci.*, vol. 61, no. 9, pp. 909–923, 1997.

[44] I. Kalay, M. J. Kramer, and R. E. Napolitano, "Crystallization Kinetics and Phase Transformation Mechanisms in Cu56Zr44 Glassy Alloy," *Metall. Mater. Trans. A*, vol. 46, no. 8, pp. 3356–3364, 2015.

[45] CAMECA, "Atom Probe Tomography," *AMETEK Inc.* [Online]. Available: http://www.cameca.com/instruments-for-research/atom-probe.aspx.

[46] J. M. Wheeler, R. Raghavan, and J. Michler, "Temperature invariant flow stress during microcompression of a zirconium-based bulk metallic glass," *Scr. mater.*, vol. 67, pp. 125–128, 2012.

[47] Y. Yang, J. C. Ye, J. Lu, F. X. Liu, and P. K. Liaw, "Effects of specimen

geometry and base material on the mechanical behavior of focused-ion-beam-fabricated metallic-glass micropillars," *Acta Mater.*, vol. 57, no. 5, pp. 1613–1623, 2009.

[48] J. C. Ye, J. Lu, Y. Yang, and P. K. Liaw, "Extraction of bulk metallic-glass yield strengths using tapered micropillars in micro-compression experiments," *Intermetallics*, vol. 18, no. 3, pp. 385–393, 2010.

[49] I. Kalay, M. J. Kramer, and R. E. Napolitano, "High-accuracy X-ray diffraction analysis of phase evolution sequence during devitrification of Cu50Zr50 metallic glass," *Metall. Mater. Trans. A Phys. Metall. Mater. Sci.*, vol. 42, no. 5, pp. 1144–1153, 2011.

[50] T. Cullinan, I. Kalay, Y. E. Kalay, M. Kramer, and R. Napolitano, "Kinetics and Mechanisms of Isothermal Devitrification in Amorphous Cu50Zr50," *Metall. Mater. Trans. A Phys. Metall. Mater. Sci.*, vol. 46, no. 2, pp. 600–613, 2015.

[51] H. Tian *et al.*, "A first-principle study of the structural and electronic properties of amorphous Cu-Zr alloys," *Sci. China-Physics Mech. Astron.*, vol. 54, no. 2, pp. 249–255, 2011.

[52] D. Wang, H. Tan, and Y. Li, "Multiple maxima of GFA in three adjacent eutectics in Zr-Cu-Al alloy system - A metallographic way to pinpoint the best glass forming alloys," *Acta Mater.*, vol. 53, no. 10, pp. 2969–2979, 2005.

[53] D. Yu *et al.*, "Glass formation in Zr-Al-Fe-Cu system," *Mater. Lett.*, vol. 157, pp. 299–302, 2015.

[54] Y. Yokoyama, T. Ishikawa, J. T. Okada, Y. Watanabe, S. Nanao, and A. Inoue, "Volume and viscosity of Zr-Cu-Al glass-forming liquid alloys," *J. Non. Cryst. Solids*, vol. 355, no. 4–5, pp. 317–322, 2009.

[55] W. Zhang, Q. Zhang, C. Qin, and A. Inoue, "Synthesis and properties of Cu–Zr–Ag–Al glassy alloys with high glass-forming ability," *Mater. Sci. Eng. B*, vol. 148, no. 1–3, pp. 92–96, 2008.

[56] Z. Xie, Y. Zhang, Y. Yang, X. Chen, and P. Tao, "Effects of rare-earth elements on the glass-forming ability and mechanical properties of Cu46Zr47-

x Al7M x (M = Ce, Pr, Tb, and Gd) bulk metallic glasses," *Rare Met.*, vol. 29, no. 5, pp. 444–450, 2010.

[57] L. Deng, B. Zhou, H. Yang, X. Jiang, B. Jiang, and X. Zhang, "Roles of minor rare-earth elements addition in formation and properties of Cu-Zr-Al bulk metallic glasses," *J. Alloys Compd.*, vol. 632, pp. 429–434, 2015.

[58] E. S. Park, J. S. Kyeong, and D. H. Kim, "Phase separation and improved plasticity by modulated heterogeneity in Cu-(Zr, Hf)-(Gd, Y)-Al metallic glasses," *Scr. Mater.*, vol. 57, no. 1, pp. 49–52, 2007.

[59] E. S. Park and D. H. Kim, "Phase separation and enhancement of plasticity in Cu-Zr-Al-Y bulk metallic glasses," *Acta Mater.*, vol. 54, no. 10, pp. 2597–2604, 2006.

[60] Y. Wang *et al.*, "Composition optimization of the Al-Co-Zr bulk metallic glasses," *Scr. Mater.*, vol. 50, no. 6, pp. 829–833, 2004.

[61] Y. M. Wang, C. H. Shek, J. B. Qiang, C. H. Wong, W. R. Chen, and C. Dong, "The e/a factor governing the formation and stability of (Zr76Ni24)1-xAlx bulk metallic glasses," *Scr. Mater.*, vol. 48, no. 11, pp. 1525–1529, 2003.

[62] T. A. Waniuk, J. Schroers, and W. L. Johnson, "Critical cooling rate and thermal stability of Zr-Ti-Cu-Ni-Be alloys," *Appl. Phys. Lett.*, vol. 78, no. 9, pp. 1213–1215, 2001.

[63] Y. Zhang, D. . Zhao, M. . Pan, and W. . Wang, "Glass forming properties of Zr-based bulk metallic alloys," *J. Non. Cryst. Solids*, vol. 315, no. 1, pp. 206–210, 2003.

[64] Z. Han and Y. Li, "Cooperative shear and catastrophic fracture of bulk metallic glasses from a shear-band instability perspective," *J. Mater. Res.*, vol. 24, no. 12, pp. 3620–3627, 2009.

[65] V. Z. Bengus *et al.*, "New features of the low temperature ductile shear failure observed in bulk amorphous alloys," *J. Mater. Sci.*, vol. 35, no. 17, pp. 4449–4457, 2000.

[66] B. A. Sun *et al.*, "Serrated flow and stick-slip deformation dynamics in the presence of shear-band interactions for a Zr-based metallic glass," *Acta*

Mater., vol. 60, no. 10, pp. 4160–4171, 2012.

[67] B. A. Sun and W. H. Wang, "The fracture of bulk metallic glasses," *Prog. Mater. Sci.*, vol. 74, pp. 211–307, 2015.

[68] F. Zeng, Y. Chen, M. Q. Jiang, C. Lu, and L. H. Dai, "Dynamic fragmentation induced by network-like shear bands in a Zr-based bulk metallic glass," *Intermetallics*, vol. 56, pp. 96–100, 2015.

[69] Z. Altounian, T. Guo-hua, and J. O. Strom-Olsen, "Crystallization characteristics of Cu-Zr metallic glasses from Cu70Zr30 to Cu25Zr75," *J. Appl. Phys.*, vol. 53, no. 7, pp. 4755–4760, 1982.

[70] E. Kneller, Y. Khan, and U. Gorres, "E. Kneller, Y. Khan, U. Gorres, Zeitschrift Fur Metallkunde 77 (1986) 152-163," *Fur Met.*, vol. 77, pp. 152–163, 1986.

[71] R. Wei, X. L. Wang, S. Yang, F. Jiang, and L. He, "Formation of CuZr-based bulk metallic glass composites containing nanometer-scale B2-CuZr phase through sub-Tg annealing," *J. Alloys Compd.*, vol. 617, pp. 699–706, 2014.

[72] H. Kozachkov, J. Kolodziejska, W. L. Johnson, and D. C. Hofmann, "Effect of cooling rate on the volume fraction of B2 phases in a CuZrAlCo metallic glass matrix composite," *Intermetallics*, vol. 39, pp. 89–93, 2013.

[73] D. Y. Wu *et al.*, "Glass-forming ability, thermal stability of B2 CuZr phase, and crystallization kinetics for rapidly solidified Cu-Zr-Zn alloys," *J. Alloys Compd.*, vol. 664, pp. 99–108, 2016.

[74] S. Pauly, G. Liu, G. Wang, U. Kühn, N. Mattern, and J. Eckert, "Microstructural heterogeneities governing the deformation of Cu47.5Zr47.5Al5 bulk metallic glass composites," *Acta Mater.*, vol. 57, no. 18, pp. 5445–5453, 2009.

[75] P. Gargarella, S. Pauly, M. Samadi Khoshkhoo, U. Kühn, and J. Eckert, "Phase formation and mechanical properties of Ti-Cu-Ni-Zr bulk metallic glass composites," *Acta Mater.*, vol. 65, pp. 259–269, 2014.

[76] Y. Wu *et al.*, "Formation of Cu-Zr-Al bulk metallic glass composites with improved tensile properties," *Acta Mater.*, vol. 59, no. 8, pp. 2928–2936,

2011.

[77] D. V. Louzguine-Luzgin *et al.*, “Nano-crystallization behavior of Zr-Cu-Al bulk glass-forming alloy,” *J. Non. Cryst. Solids*, vol. 358, no. 2, pp. 145–149, 2012.

[78] M. P. Macht *et al.*, “Decomposition of the Supercooled Liquid of the Bulk Amorphous Alloy Zr41Ti14Cu12.5Ni10Be22.5,” *Mater. Sci. Forum*, vol. 225–227, pp. 65–70, 1996.

[79] R. Busch, Y. J. Kim, S. Schneider, and W. L. Johnson, “Atom probe field ion microscope and levitation studies of the decomposition and crystallization of undercooled Zr-Ti-Cu-Ni-Be melts,” *Metastable, Mech. Alloy. Nanocrystalline Mater. Pts 1 2*, vol. 225, pp. 77–82, 1996.

[80] C. C. Hays, C. P. Kim, and W. L. Johnson, “Large supercooled liquid region and phase separation in the Zr-Ti-Ni-Cu-Be bulk metallic glasses,” *Appl. Phys. Lett.*, vol. 75, no. 8, pp. 1089–1091, 1999.

[81] W. Wang, W. Q., and F. S., “Microstructure, decomposition, and crystallization in Zr41Ti14Cu12.5Ni10Be22.5 bulk metallic glass,” *Phys. Rev. B*, vol. 57, no. 14, pp. 8211–8217, 1998.

[82] D. H. Kim, W. T. Kim, E. S. Park, N. Mattern, and J. Eckert, “Phase separation in metallic glasses,” *Prog. Mater. Sci.*, vol. 58, no. 8, pp. 1103–1172, 2013.

[83] J. H. Han *et al.*, “Phase separation in Zr56-xGdxCo28Al16 metallic glasses (0⩽x⩽20),” *Acta Mater.*, vol. 66, pp. 262–272, 2014.

[84] G. Wu, Q. H. Tang, N. N. Yu, and X. S. Miao, “Phase separation and nanocrystallization behavior above crystallization temperature in Mg-Cu-Y metallic glass thin film,” *Thin Solid Films*, vol. 545, pp. 38–43, 2013.

[85] N. Mattern *et al.*, “Microstructure and thermal behavior of two-phase amorphous Ni-Nb-Y alloy,” *Scr. Mater.*, vol. 53, no. 3, pp. 271–274, 2005.

[86] C. Yıldırım, “Structural and Dynamical Evolution of Nanocrystals,” no. July, p. 93, 2013.

[87] K. J. Laws *et al.*, “Analysis of dynamic segregation and crystallisation in Mg

65Cu 25Y 10 bulk metallic glass using atom probe tomography," *Mater. Sci. Eng. A*, vol. 556, pp. 558–566, 2012.

[88] I. Kalay, "Devitrification kinetics and phase selection mechanisms in Cu-Zr metallic glasses," p. 187, 2010.

[89] A. L. Greer, M. E., and G. Editors, "Bulk Metallic Glasses : At the Cutting Edge of Metals Research," *MRS Bull.*, vol. 32, no. August, pp. 611–619, 2007.

[90] W. H. Wang, C. Dong, and C. H. Shek, "Bulk metallic glasses," *Mater. Sci. Eng. R Reports*, vol. 44, no. 2–3, pp. 45–90, 2004.

[91] M. M. Trexler and N. N. Thadhani, "Mechanical properties of bulk metallic glasses," *Prog. Mater. Sci.*, vol. 55, no. 8, pp. 759–839, 2010.

[92] W. H. Wang, "The elastic properties, elastic models and elastic perspectives of metallic glasses," *Prog. Mater. Sci.*, vol. 57, no. 3, pp. 487–656, 2012.

[93] M. Chen, "Mechanical Behavior of Metallic Glasses: Microscopic Understanding of Strength and Ductility," *Annu. Rev. Mater. Res.*, vol. 38, no. 1, pp. 445–469, Jul. 2008.

[94] P. Thurnheer, R. Maaß, K. J. Laws, S. Pogatscher, and J. F. Löffler, "Dynamic properties of major shear bands in Zr-Cu-Al bulk metallic glasses," *Acta Mater.*, vol. 96, pp. 428–436, 2015.

[95] R. Maaß, D. Klaumünzer, and J. F. Löffler, "Propagation dynamics of individual shear bands during inhomogeneous flow in a Zr-based bulk metallic glass," *Acta Mater.*, vol. 59, no. 8, pp. 3205–3213, 2011.

[96] Y. H. Lai, H. M. Chen, C. J. Lee, J. C. Huang, and J. S. C. Jang, "Strain burst speeds in metallic glass micropillars," *Intermetallics*, vol. 18, no. 10, pp. 1893–1897, 2010.

[97] W. J. Wright, M. W. Samale, T. C. Hufnagel, M. M. LeBlanc, and J. N. Florando, "Studies of shear band velocity using spatially and temporally resolved measurements of strain during quasistatic compression of a bulk metallic glass," *Acta Mater.*, vol. 57, no. 16, pp. 4639–4648, 2009.

[98] H. B. Ke, B. A. Sun, C. T. Liu, and Y. Yang, "Effect of size and base-element on the jerky flow dynamics in metallic glass," *Acta Mater.*, vol. 63, no.

January, pp. 180–190, 2014.

[99] R. Maaß *et al.*, “Smaller is stronger: The effect of strain hardening,” *Acta Mater.*, vol. 57, no. 20, pp. 5996–6005, 2009.

[100] G. Kumar, A. Desai, and J. Schroers, “Bulk metallic glass: The smaller the better,” *Adv. Mater.*, vol. 23, no. 4, pp. 461–476, 2011.

[101] R. Limbach, K. Kosiba, S. Pauly, U. K??hn, and L. Wondraczek, “Serrated flow of CuZr-based bulk metallic glasses probed by nanoindentation: Role of the activation barrier, size and distribution of shear transformation zones,” *J. Non. Cryst. Solids*, vol. 459, pp. 130–141, 2017.

[102] W. D. Nix and H. Gao, “Indentation size effects in crystalline materials: A law for strain gradient plasticity,” *J. Mech. Phys. Solids*, vol. 46, no. 3, pp. 411–425, 1998.

[103] N. Van Steenberge *et al.*, “Dynamic softening and indentation size effect in a Zr-based bulk glass-forming alloy,” *Scr. Mater.*, vol. 56, no. 7, pp. 605–608, 2007.

[104] F. Xu, Y. H. Ding, X. H. Deng, P. Zhang, and Z. L. Long, “Indentation size effects in the nano- and micro-hardness of a Fe-based bulk metallic glass,” *Phys. B Condens. Matter*, vol. 450, pp. 84–89, 2014.

[105] Y. H. Lai *et al.*, “Bulk and microscale compressive behavior of a Zr-based metallic glass,” 2008.

[106] H. M. Chen, J. C. Huang, S. X. Song, T. G. Nieh, and J. S. C. Jang, “Flow serration and shear-band propagation in bulk metallic glasses,” vol. 141914, 2009.